# Appendix B – Part II

## Results from Prior Support (one-pagers)

As examples of the breadth and vitality of the scientific achievements of the COMPRES community, Appendix B of this proposal provides 143 research "one-pagers" that have been submitted by research groups in preparation of this proposal that summarize selected published results enabled by COMPPRES investment in community facilities and infrastructure from 2012-2016.

## Table of Contents – One-Pagers

# High Pressure-Temperature Phase Diagrams of Energetic Materials: FOX-7 & TATB

Matthew Bishop, Nenad Velisavljevic, Raja Chellappa, Zhexian Liu, Dana Dattelbaum, and Yogesh Vohra

(COMPRES-related facilities: NSLS – U2A, Infrared Spectroscopy Beamline)

The pressure-temperature (P-T) phase diagrams of 2,4,6-triamino-1,3,5-trinitrobenzene (TATB) and 1,1-diamino-2,2-dinitroethylene (FOX-7) were determined by *in situ* synchrotron infrared radiation spectroscopy at NSLS, U2A beamline, with resistively heated diamond anvil cell techniques. The decomposition boundaries for both TATB and FOX-7 were established up to 10 GPa. For TATB, the decomposition boundary exhibits a very low ~ 4°C / GPa slope. In contrast, the decomposition boundary of FOX-7 has an anomalous change of slope at a ($\alpha$ + Phase I + decomposition) triple point with a negative slope of ~ 180°C / GPa. The anomalous behavior of the decomposition boundary may indicate a structural modification to a slightly higher symmetry than the $\alpha$-phase $P2_1/n$ or evidence of a potential 'island' phase. The high-pressure $\varepsilon$-phase of FOX-7 has a moderate positive slope of ~ 29°C / GPa up to 10 GPa. The similarities between the decomposition boundaries of the $\varepsilon$-phase of FOX-7 and TATB are remarkable: both phases have triclinic symmetry and planar molecular/layering structures with moderate positive slopes extending over a broad range of pressure. These results provide the first recorded evidence of high P-T stability of two similar high explosives and provide strong evidence for the potential mechanisms behind sensitivity and performance. However, additional experiments are needed to further elucidate the role thermal kinetics and strain rate have on the mechanisms behind sensitivity and performance characteristics.
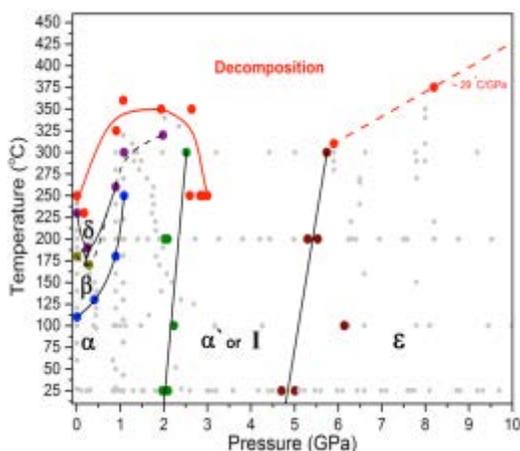


**Figure 1.** The high pressure-temperature phase diagram of FOX-7 with colored symbols indicating the presence of the respective phase along a particular PT pathway represented by grey symbols, and the decomposition boundary is indicated in red symbols (lines).

**Figure 2.** The high pressure-temperature phase diagram of TATB with grey symbols (lines) indicating PT pathways, and the decomposition boundary is indicated in red symbols (lines).
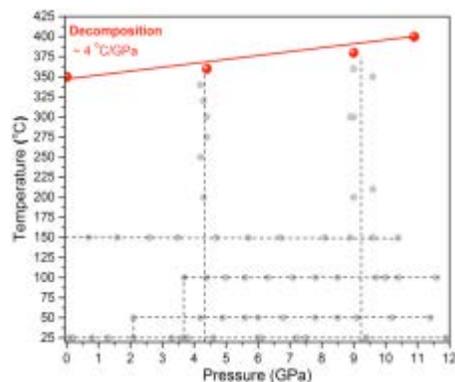
**References:**

[1] Matthew M. Bishop, Nenad Velisavljevic, Raja S. Chellappa, Dana Dattelbaum, and Yogesh K. Vohra, "Communication: High pressure temperature phase diagrams of TATB and FOX-7," J. Chem. Phys. Comm., under review (2016).

[2] Matthew M. Bishop, Nenad Velisavljevic, Raja S. Chellappa, and Yogesh K. Vohra, " The High Pressure Temperature Phase Diagram of 1,1 diamino-2,2-dinitroethylene (FOX-7)," J. Phys. Chem. A., 119 9739 (2015).

[3] Matthew M. Bishop, Raja S. Chellapa, Zhexian Liu, Daniel N. Preston, Mary Sandstrom, Dana M. Dattelbaum, Yogesh K. Vohra, and Nenad Velisavljevic, "High pressure-temperature polymorphism of 1,1-diamino-2,2-dinitroethylene," J. Phys. Conf. Ser. 500 052005 (2014).

[4] Matthew M. Bishop, Raja S. Chellappa, Michael Pravica, Josh Coe, Zhenxian Liu, Dana Dattelbaum, Yogesh K. Vohra, and Nenad Velisavljevic "1,1-Diamino-2,2-Dinitroethylene Under High Pressure Temperature," J. Chem. Phys. 137 174304 (2012).

# Nanocrystals in Compression: Unexpected Structural Phase Transition and Amorphization due to Surface Impurities

Gang Liu, Lingping Kong, Jinyuan Yan, Zhenxian Liu, et.al

(COMPRES-related facilities: NSLS U2A beamline)

We study an unprecedented surface doping-driven anomaly in the compression behaviors of nanocrystals that demonstrates the change of surface chemistry can lead to interior bulk structure change in nanoparticles. In the synchrotron-based x-ray diffraction experiments, titania nanocrystals with low concentration yttrium dopants at the surface are found to be less compressible than undoped titania nanocrystals. More surprisingly, an unexpected $TiO_2(II)$ phase ($\alpha$-$PbO_2$ type) is induced and obvious anisotropy is observed in compression of the yttrium-doped $TiO_2$, in sharp contrast to the compression behavior of undoped $TiO_2$. In addition, the undoped brookite nanocrystals stay with the same structure up to 30 GPa, whereas the yttrium-doped brookite amorphizes above 20 GPa. The abnormally structural evolution observed in yttrium-doped $TiO_2$ do not agree with the reported phase stability of nano titania polymorphs, thus suggest that the physical properties of the interior of nanocrystals can be controlled by the surface.
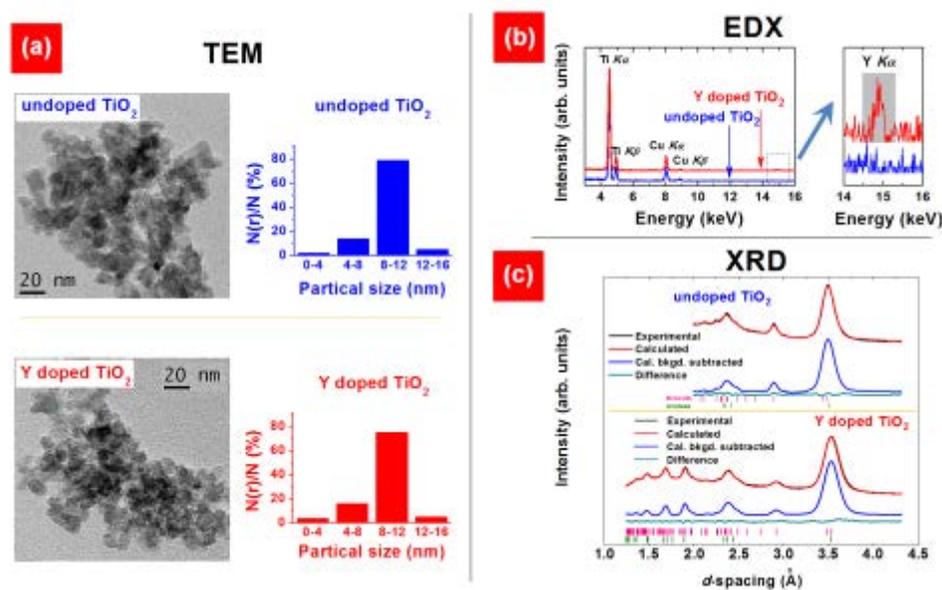


**Figure 1.** Characterizations of undoped and yttrium doped $TiO_2$ nanoparticles before compression. (a) TEM examinations and derived particle size distributions of both undoped and Y doped samples. The particle sizes fall in the narrow range of 8-12 nm, with particle number percentage of 79% and 75% for undoped $TiO_2$ and yttrium doped $TiO_2$, respectively. (b) An Y:Ti atomic ratio of ~1:100 in yttrium doped sample based on the EDX estimation. The detected Cu signal comes from the Cu TEM support (see materials and methods). (c) The results of synchrotron XRD experiments indicate the mixed phases of brookite and anatase in both samples. The initial mol. percentage of brookite in undoped and doped samples before compression is ~66% and ~70%, respectively. Anatase reflections are indicated by dark green '|'; pink ones represent brookite diffraction positions

References: Gang Liu, Lingping Kong, Jinyuan Yan, Zhenxian Liu, Hengzhong Zhang, et.al, (2016), Nanocrystals in compression: unexpected structural phase transition and amorphization due to surface impurities, *Nanoscale,* DOI: 10.1039/C5NR09027J.

# Pressure induced conductivity and yellow-to-black piezochromism in a layered Cu-Cl hybrid perovskite

Adam Jaffe, Yu Lin, Wendy L. Mao, and Hemamala Karunadasa, Stanford University

(COMPRES-related facilities: ALS 12.2.2, NSLS U2A)

Pressure-induced changes in the electronic structure of two-dimensional Cu-based materials have been a subject of intense study. In particular, the possibility of suppressing the Jahn-Teller distortion of $d^9$ Cu centers with applied pressure has been debated over a number of decades. We studied the structural and electronic changes resulting from the application of pressures up to ca. 60 GPa on a two-dimensional copper (II)-chloride perovskite using diamond anvil cells (DACs), through a combination of in situ powder x-ray diffraction, electronic absorption and vibrational spectroscopy, dc conductivity measurements, and optical observations. Our measurements show that compression of this charge-transfer insulator initially yields a first-order structural phase transition at ca. 4 GPa similar to previous reports on other $Cu^{II}$–Cl perovskites, during which the originally translucent yellow solid turns red. Further compression induces a previously unreported phase transition at ca. 8 GPa and dramatic piezochromism from translucent red-orange to opaque black. Two-probe dc resistivity measurements conducted within the DAC show the first instance of appreciable conductivity in $Cu^{II}$–Cl perovskites. The conductivity increases by 5 orders of magnitude between 7 and 50 GPa, with a maximum measured conductivity of $2.9 \times 10^{-4}$ S·cm$^{-1}$ at 51.4 GPa. Electronic absorption spectroscopy and variable-temperature conductivity measurements indicate that the perovskite behaves as a 1.0-eV bandgap semiconductor at 39.7 GPa, and has an activation energy for electronic conduction of 0.218(5) eV at 51.4 GPa. Remarkably, all these changes are reversible: the material reverts to a translucent yellow solid upon decompression and ambient pressure powder x-ray diffraction data taken before and after compression up to 60 GPa show that the original structure is maintained with minimal hysteresis.
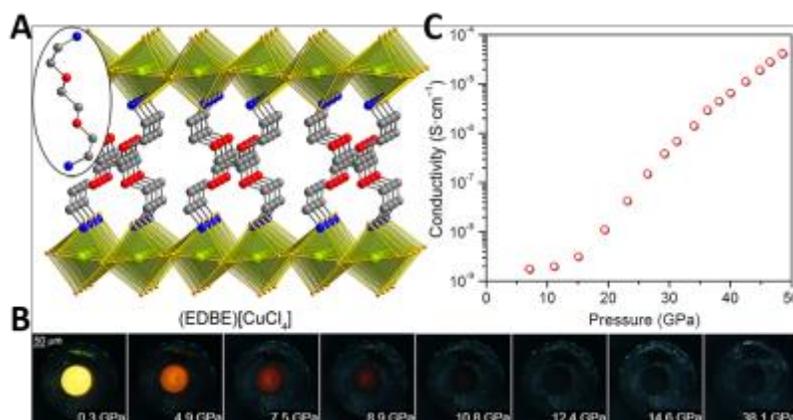


**Figure 1.** A) X-ray structure of (EDBE)[CuCl$_4$]. Inset: an EDBE dication. Cu: green, Cl: orange, O: red, N: blue, and C: gray. H atoms omitted for clarity. B) The material undergoes dramatic piezochromism from translucent yellow to opaque black. C) Two-probe dc conductivity measurements show the conductivity increases by 5 orders of magnitude between 7 and 50 GPa. EDBE = 2,2'-(ethylenedioxy)bis(ethylammonium))

References: Adam Jaffe, Yu Lin, Wendy L. Mao, and Hemamala Karunadasa, (2015), Pressure-Induced Conductivity and Yellow-to-Black Piezochromism in a Layered Cu-Cl Hybrid Perovskite, *J. Am. Chem. Soc.,* **137**, 1673-1678.

# Pressure-driven high-to-low spin transition in the bimetallic quantum magnet [Ru2(O2CMe)4]3[Cr(CN)6]

K. R. O'Neal[1], Z. Liu[2], Joel S. Miller[3], R. S. Fishman[4], and J. L. Musfeldt[1]

[1]University of Tennessee, [2]Carnegie Institute of Washington, [3]University of Utah,
[4]Oak Ridge National Laboratory

(COMPRES-related facilities: NSLS Beamline U2A)

Synchrotron-based infrared and Raman spectroscopies were brought together with diamond anvil cell techniques and an analysis of the magnetic properties to investigate the pressure-induced high $\rightarrow$ low spin transition in [Ru2(O2CMe)4]3[Cr(CN)6]. We find that the extended nature of the diruthenium wave function combined with coupling to chromium-related local lattice distortions changes the relative energies of the $\pi^*$ and $\delta^*$ orbitals and drives the high $\rightarrow$ low spin transition on the mixed-valence diruthenium complex. This is a rare example of an externally controlled metamagnetic transition in which both spin-orbit and spin-lattice interactions contribute to the mechanism.
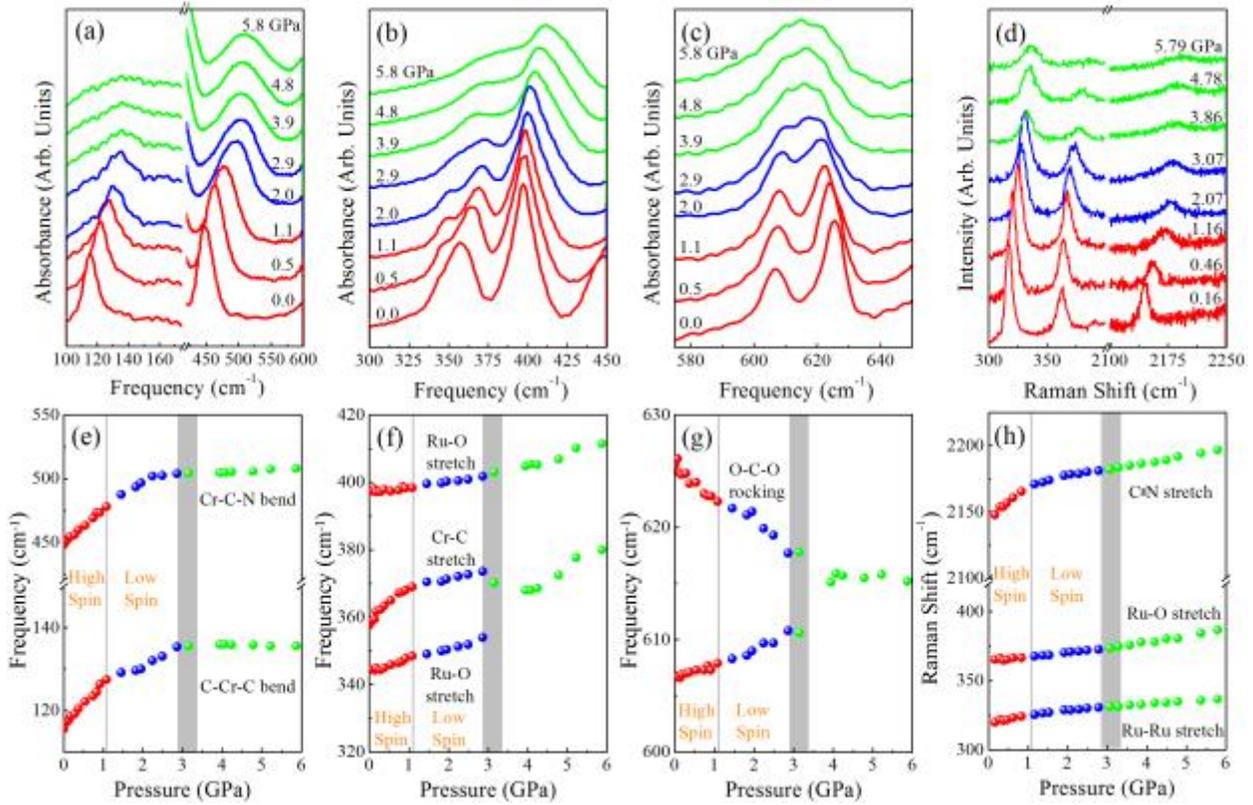
**Figure 1.** Close-up views of the infrared (a-c) and Raman (d) response of [Ru2(O2CMe)4]3[Cr(CN)6] as a function of pressure at 300 K. (e-h) Frequency versus pressure trends showing how the various modes change through the pressure-driven transitions (denoted by the gray vertical lines at 1 and 3.2 GPa.

Reference: K. R. O'Neal, Z. Liu, Joel S. Miller, R. S. Fishman, and J. L. Musfeldt, Pressure-driven high-to-low spin transition in the bimetallic quantum magnet [Ru2(O2CMe)4]3[Cr(CN)6], *Phys. Rev. B,* **90**, 104301 (2014).

# Pressure-induced magnetic crossover driven by hydrogen bonding in $CuF_2(H_2O)_2$(3-chloropyridine)

K. R. O'Neal[1], T. V. Brinzari[1,2], J. B. Wright[1], C. Ma[3,4], S. Giri[5], J. A. Schlueter[6,7], Q. Wang[5,8], P. Jena[5], Z. Liu[3] and J. L. Musfeldt[1]

[1]University of Tennessee, [2]University of Florida, [3]Carnegie Institute of Washington, [4]Jilin University, [5]Virginia Commonwealth University, [6]Argonne National Laboratory, [7]National Science Foundation, [8]Center for Applied Physics and Technology of Peking University

(COMPRES-related facilities: NSLS Beamline U2A)

We combined diamond anvil cell techniques, synchrotron-based infrared spectroscopy, and complimentary density functional theory based calculations to investigate the mechanism of the pressure-induced 0.8 GPa magnetoelastic phase transition in $CuF_2(H_2O)_2$(3-chloropyridine). Our spectra reveal changes that suggest a pressure-induced increase in crystal symmetry brought about by the tilting of the 3-chloropyridine rings in the direction of the chlorine. This tilting brings the chlorine center closer to the $H_2O$ ligands. The increased electrostatic interaction may establish additional hydrogen bonding linkages in the *c* direction that can act as superexchange pathways between copper centers. Development of this new exchange pathway combined with the buckled *ab* plane hydrogen bonding exchange pathway yields a three dimensional superexchange network between copper centers that may facilitate the antiferromagnetic to ferromagnetic crossover. Analysis of the local lattice distortions also allows us to identify two additional structural phase transitions at 4 and 6 GPa that mostly involve lowering the symmetry of the penta-coordinate copper environment, not the 3-chloropyridine ring.
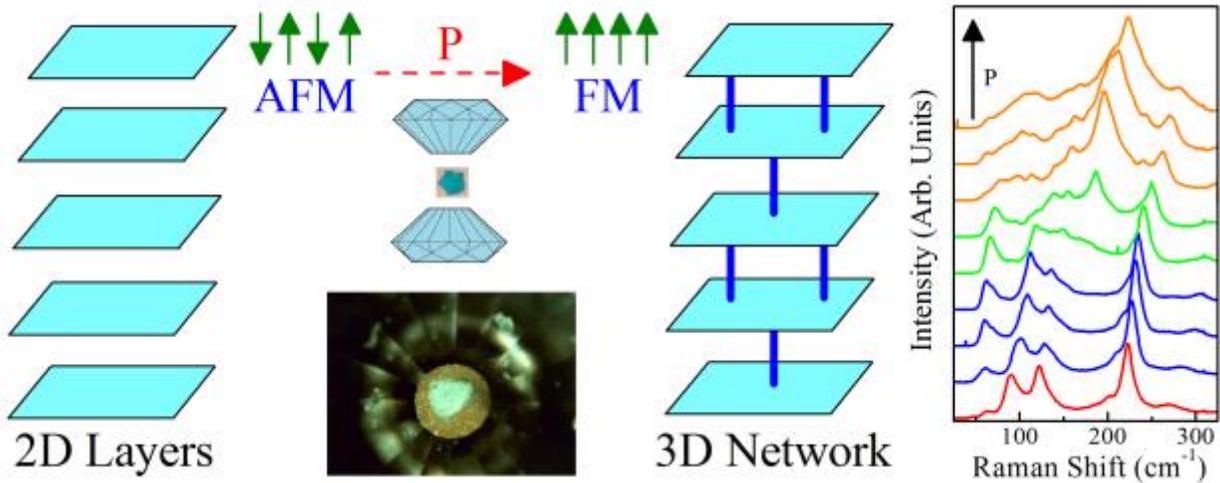


**Figure 1.** Left: Schematic representation of the pressure-induced two-to-three dimensional superexchange network crossover that accompanies the antiferromagnetic-to-ferromagnetic crossover in $CuF_2(H_2O)_2$(3-chloropyridine). The center contains images of the sample in the diamond anvil cell. Right: Representative low frequency Raman spectra at increasing pressures, color coded for each observed phase. This region is rich with spectral changes that were used to identify the phase transitions at 4 and 6 GPa.

Reference: K. R. O'Neal, T. V. Brinzari, J. B. Wright, C. Ma, S. Giri, J. A. Schlueter, Q. Wang, P. Jena, Z. Liu and J. L. Musfeldt, Pressure-Induced Magnetic Crossover Driven by Hydrogen Bonding in $CuF_2(H_2O)_2$(3-chloropyridine), *Sci. Rep.,* **4**, 6054 (2014).

# Pressure-induced structural transition in copper pyrazine dinitrate and implications for quantum magnetism

K. R. O'Neal[1], J. Zhou[2], J. G. Cherian[1], M. M. Turnbull[3], C. P. Landee[3], P. Jena[2], Z. Liu[4], and J. L. Musfeldt[1]

[1]*University of Tennessee*, [2]*Virginia Commonwealth University*, [3]*Clark University*, [4]*Carnegie Institute of Washington*

(COMPRES-related facilities: NSLS Beamline U2A)

We combined synchrotron-based infrared and Raman spectroscopies, diamond anvil cell techniques, and first principles calculations to unveil pressure-induced distortions in quasi-one-dimensional $Cu(pyrazine)(NO_3)_2$. The crossover found at 0.7 GPa is local in nature and involves only interchain spacing effects on the nitrate groups. The transition at 5 GPa lowers the overall crystal symmetry from *Pmna* to *P222_1* and is predicted to slightly increase magnetic dimensionality. Comparison with prior magneto-infrared results reveals the striking role of out-of-plane bending of the pyrazine ligand, a finding that we discuss in terms of the possibility of using pressure to bias the magnetic quantum critical transition in this classic $S = 1/2$ antiferromagnet.
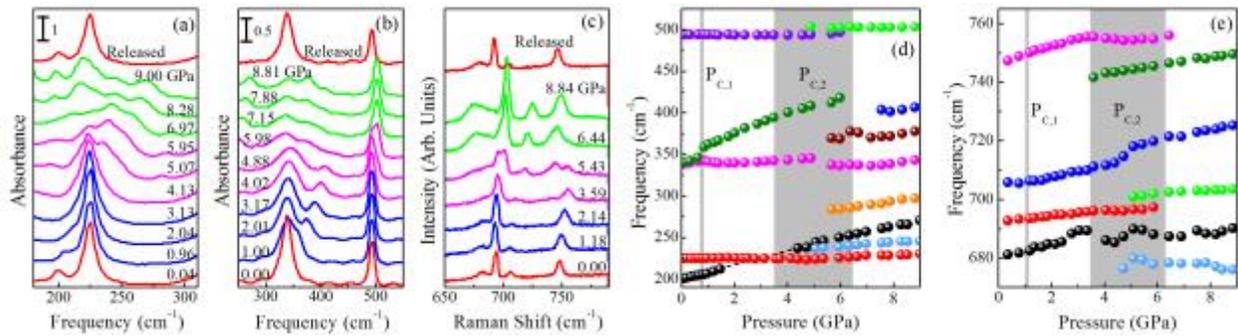


**Figure 1.** (a,b) Infrared and (c) Raman spectra under compression and upon release of pressure. Scale bars are included for clarity, and line colors represent different or coexistence of phases. (d,e) Frequency versus pressure for the vibrational modes seen in (a-c). The gray vertical bands indicate transition regions.
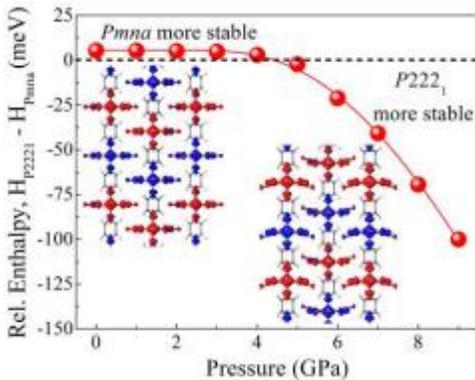


**Figure 2.** (a) Relative enthalpy ($H = E + PV$) and (b) unit cell volume of the ambient *Pmna* and high pressure *P222_1* phases as a function of pressure. Through the 5 GPa transition the *P222_1* structure becomes more stable. Insets in (a) are calculated magnetic isosurfaces where red and blue surfaces represent spin up and spin down states, respectively. The high pressure state is still a collinear antiferromagnet where neighboring chains have shifted in opposite directions, leading to out-of-plane bending of the nitrate groups.

Reference:

K. R. O'Neal, J. Zhou, J. G. Cherian, M. M. Turnbull, C. P. Landee, P. Jena, Z. Liu, and J. L. Musfeldt, Pressure-induced structural transition in copper pyrazine dinitrate and implications for quantum magnetism, *Phys Rev. B,* **93**, 104409 (2016).

# High pressure vibrational properties of WS$_2$ nanotubes

K. R. O'Neal[1], J. G. Cherian[1], A. Zak[2], R. Tenne[3], Z. Liu[4], and J. L. Musfeldt[1]

[1]*University of Tennessee,* [2]*Holon Institute of Technology,* [3]*Wietzmann Institute,*
[4]*Carnegie Institute of Washington*

(COMPRES-related facilities: NSLS Beamline U2A)

We report the high pressure infrared and Raman response of multi-walled WS$_2$ nanotubes up to 20 GPa in order to study the pressure-induced breakdown pathway. Combining, for the first time, infrared and Raman reveals that while most of the vibrational modes display similar pressure-induced frequency changes, the Raman-active A$_{1g}$ interlayer vibrational mode is almost twice as responsive. This extra sensitivity suggests that the nanotube breakdown pathway proceeds through this interlayer breathing mode. Moreover, an increasing infrared background is fit to a percolation model, indicating a hopping barrier of 350 cm$^{-1}$ and that the nanotubes display some conductivity, although no metallic response is observed up to 20 GPa.
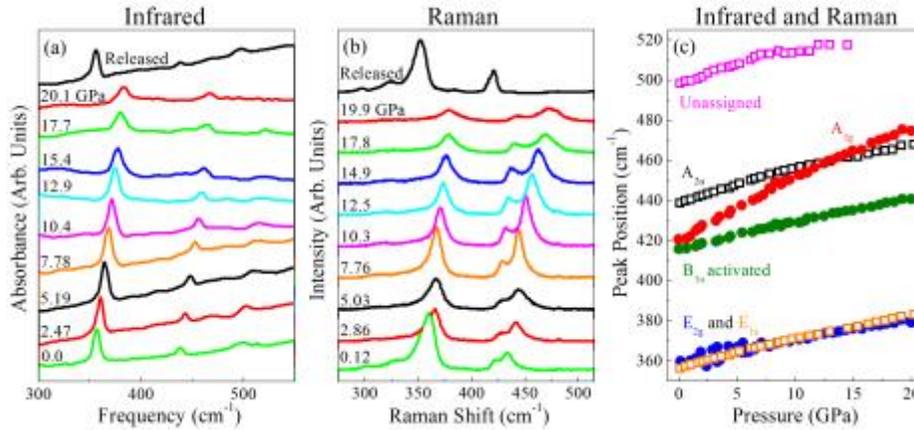


**Figure 1.** (a) Infrared and (b) Raman spectra of WS$_2$ nanotubes at the indicated pressures. (c) Frequency versus pressure for the infrared- (open squares) and Raman-active (closed circles) modes, displaying the stronger pressure sensitivity of the A$_{1g}$ mode.
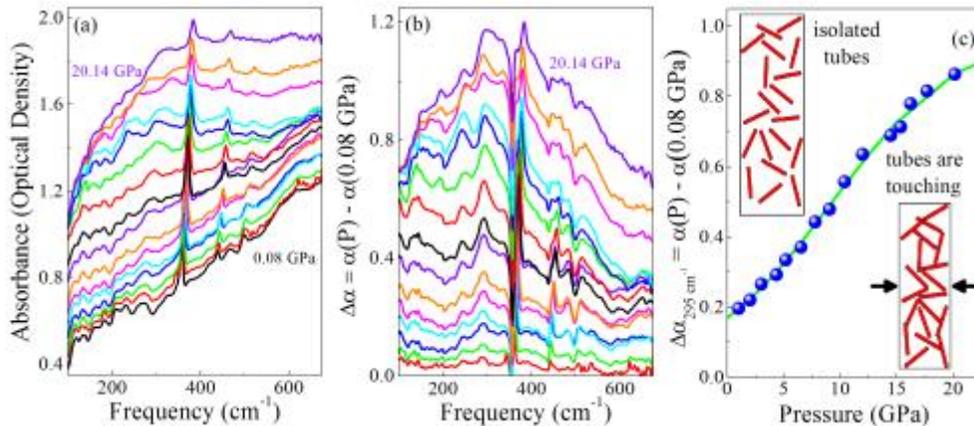


**Figure 2.** (a) Infrared spectra and (b) absorption difference up to 20 GPa, showing the increasing background due to improved conductivity. (c) Absorption difference at 295 cm$^{-1}$ versus pressure. Insets: schematic diamond anvils cell at low and high pressure showing the conductive pathway that forms.

Reference: K. R. O'Neal, J. G. Cherian, A. Zak, R. Tenne, Z. Liu, and J. L. Musfeldt, High Pressure Vibrational Properties of WS$_2$ Nanotubes, *Nano. Lett.,* **16**, 993-999 (2016).

# Infrared study of the pressure-induced insulator-to-metal transition in $PrRu_4P_{12}$

Hidekazu Okamura, Tokushima University

(COMPRES-related facility: National Synchrotron Light Source U2A Beamline)

Optical conductivity [$\sigma(\omega)$] of $PrRu_4P_{12}$ has been studied under high pressure to 14 GPa, at low temperatures to 8 K, and at photon energies 12 meV–1.1 eV. $\sigma(\omega)$ of a sample at high pressure was obtained from the analysis of a reflectance spectrum, $R(\omega)$, measured with a diamond anvil cell (DAC). $R(\omega)$ in the spectral range between 12 and 20 meV was measured using the beamline U2A at NSLS, while that between 20 meV and 1.1 eV was measured using the beamline BL43IR at SPring-8. The energy gap in $\sigma(\omega)$ at ambient pressure, shown in Fig. 1(a), is caused by a metal-insulator transition due to an unconventional charge-density-wave formation at 63 K. With increasing pressure to 10 GPa, as shown in Fig. 1(b), the energy gap is gradually filled in. At 14 GPa and below 30 K, $\sigma(\omega)$ exhibits a pronounced Drude-type component due to free carriers. This indicates that the initial insulating ground state at zero pressure has been turned into a metallic one at 14 GPa. This is consistent with a previous resistivity study under pressure, where the resistivity rapidly decreased with cooling below 30 K at 14 GPa. As discussed in detail in Okamura et al. (2012), the evolution of electronic structure with pressure is qualitatively consistent with a theoretical model, that assumes an unconventional CDW formation based on the crystal field degree of freedom in the $Pr^{3+}$ ions.
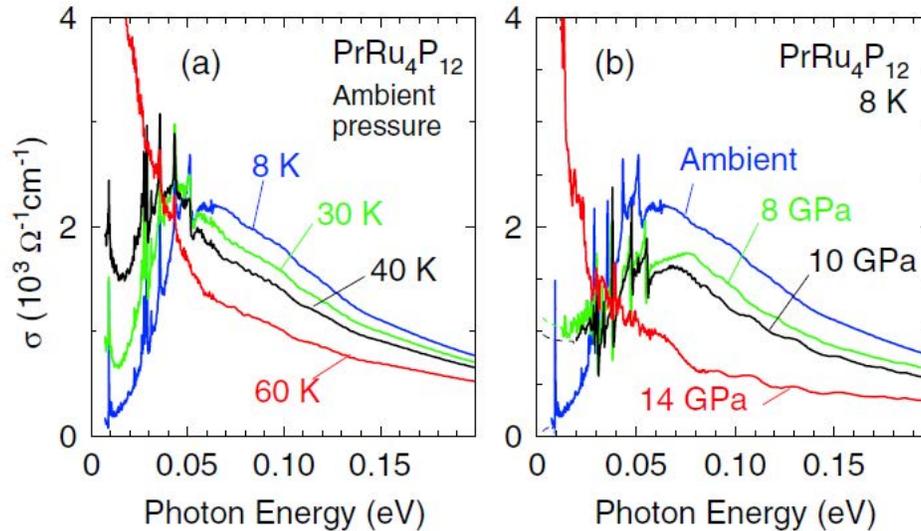


**Figure 1.** Optical conductivity $\sigma(\omega)$ spectra of $PrRu_4P_{12}$. In (a), the spectra were measured under ambient pressure, and in (b) they were measured under high pressure using DAC, where the low-energy range at 12-20 meV was measured at U2A beamline at NSLS.

Reference: H. Okamura et al. (2012), Pressure suppression of unconventional charge-density-wave state in $PrRu_4P_{12}$ studied by optical conductivity, *Physical Review B,* **85**, 205116 .

# High-Pressure Single-Crystal Structures of 3D Lead-Halide Hybrid Perovskites and Pressure Effects on their Electronic and Optical Properties

Adam Jaffe†, Yu Lin†‡§, Christine M. Beavers‖, Johannes Voss⊥, Wendy L. Mao*‡§, and Hemamala I. Karunadasa*†

†Departments of Chemistry and ‡Geological Sciences, Stanford University,§ Photon Science and Stanford Institute for Materials and Energy Sciences, SLAC, ‖ Advanced Light Source/ UC Santa Cruz,⊥ SUNCAT Center for Interface Science and Catalysis, SLAC

## COMPRES-related facility: Beamline 12.2.2 at the Advanced Light Source

We report the first high-pressure single-crystal structures of hybrid perovskites. The crystalline semiconductors (MA)PbX$_3$ (MA = CH$_3$NH$_3^+$, X = Br$^-$ or I$^-$) afford us the rare opportunity of understanding how compression modulates their structures and thereby their optoelectronic properties. Using atomic coordinates obtained from high-pressure single-crystal X-ray diffraction data, collected on Beamline 12.2.2 at the Advanced Light Source, we track the perovskites' precise structural evolution upon compression. These structural changes correlate well with pressure-dependent single-crystal photoluminescence (PL) spectra and high-pressure bandgaps derived from density functional theory. We further observe dramatic piezochromism where the solids become lighter in color and then transition to opaque black with compression. Indeed, electronic conductivity measurements of (MA)PbI$_3$ obtained within a diamond-anvil cell show that the material's resistivity decreases by 3 orders of magnitude between 0 and 51 GPa. The activation energy for conduction at 51 GPa is only 13.2(3) meV, suggesting that the perovskite is approaching a metallic state. Furthermore, the pressure response of mixed-halide perovskites shows new luminescent states that emerge at elevated pressures. We recently reported that the perovskites (MA)Pb(Br$_x$I$_{1-x}$)$_3$ (0.2 < $x$ < 1) reversibly form light-induced trap states, which pin their PL to a low energy. This may explain the low voltages obtained from solar cells employing these absorbers. Our high-pressure PL data indicate that compression can mitigate this PL redshift and may afford higher steady-state voltages from these absorbers. These studies show that pressure can significantly alter the transport and thermodynamic properties of these technologically important semiconductors.
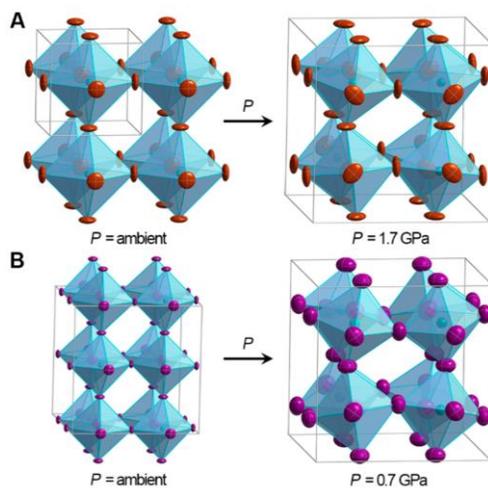


Figure 1-Single-crystal X-ray structures of (A) (MA)PbBr3 at ambient pressure and 1.7 GPa, (B) (MA)PbI3 at ambient pressure and 0.7 GPa.
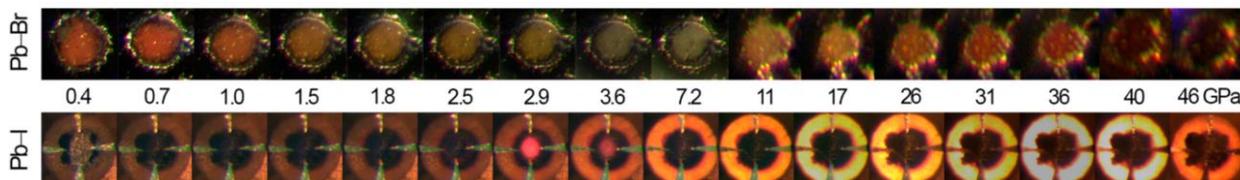


Figure 2-Optical micrographs showing piezochromic transitions of (MA)PbBr3 (top) and (MA)PbI3 (bottom)

Reference: Jaffe, A.; Lin, Y.; Beavers, C. M.; Voss, J.; Mao, W. L.; Karunadasa, H. I. High-Pressure Single-Crystal Structures of 3D Lead-Halide Hybrid Perovskites and Pressure Effects on their Electronic and Optical Properties. *ACS Central Science* **2016**, *2*, 201.

# Material and elastic properties of Al-tobermorite in ancient Roman seawater concrete

The pyroclastic aggregate concrete of Trajan's Markets (110 CE), now Museo Fori Imperiali in Rome, has absorbed energy from seismic ground shaking and long-term foundation settlement for nearly two millenia while remaining largely intact at the structural scale. The scientific basis of this exceptional service record is explored through computed tomography of fracture surfaces and synchroton X-ray microdiffraction analyses of a reproduction of the standardized hydrated lime–volcanic ash mortar that binds decimeter-sized tuff and brick aggregate in the conglomeratic concrete. The mortar reproduction gains fracture toughness over 180 d through progressive coalescence of calcium–aluminum-silicate–hydrate (C-A-S-H) cementing binder with $Ca/(Si+Al) \approx 0.8–0.9$ and crystallization of strätlingite and siliceous hydrogarnet (katoite) at $\geq 90$ d, after pozzolanic consumption of hydrated lime was complete. Platey strätlingite crystals toughen interfacial zones along scoria perimeters and impede macroscale propagation of crack segments. In the 1,900-y-old mortar, C-A-S-H has low $Ca/(Si+Al) \approx 0.45–0.75$. Dense clusters of 2- to 30-μm strätlingite plates further reinforce interfacial zones, the weakest link of modern cement-based concrete, and the cementitious matrix. These crystals formed during long-term autogeneous reaction of dissolved calcite from lime and the alkali-rich scoriae groundmass, clay mineral (halloysite), and zeolite (phillipsite and chabazite) surface textures from the Pozzolane Rosse pyroclastic flow, erupted from the nearby Alban Hills volcano. The clast-supported conglomeratic fabric of the concrete presents further resistance to fracture propagation at the structural scale.
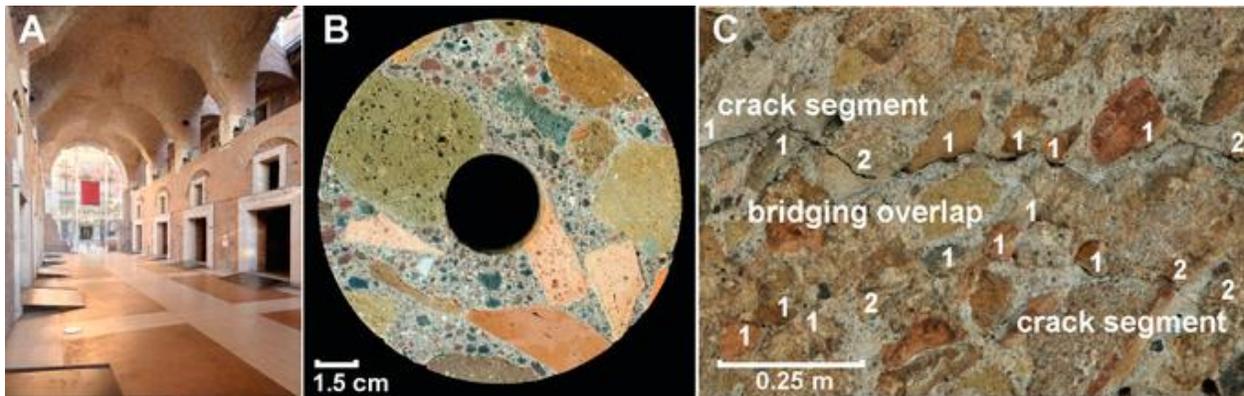


Markets of Trajan concretes. (A) Great Hall, vaulted ceiling and brick-faced concrete walls; reprinted with permission from Archives, Museo Fori Imperiali. (B) Drill core with Pozzolane Rosse volcanic ash (harena fossicia) mortar and conglomeratic aggregate (caementa). (C) Fractures in vaulted ceiling, Grande Emiciclo: 1, crack follows caementa perimeter; 2, crack traverses caementa. Wall concrete contains ~88 vol % pyroclastic rock: 45–55% tuff (and brick) as caementa, ~38% volcanic ash pozzolan, and ~12% lime paste, with 3:1 ash:lime volumetric ratio (de Architectura 2.5.1) in the mortar.

Jackson, M.D., Moon, J., Gotti, E., Taylor, R., Chae, S.R., Kunz, M., Emwas, A.H., Meral, C., Guttmann, P., Levitz, P., Wenk, H.-R., Monteiro, P.J.M. (2013). Material and elastic properties of Al-tobermorite in ancient Roman seawater concrete. *J. Am. Ceram. Soc.* 96, 2598-2606; DOI:10.1111/jace.12407

***High-Pressure behavior of Osmium: An Analog for Iron in Earth's Core***

B.K. Godwal[1], J. Yan[2], and R. Jeanloz[1]

[1]University of California, Berkeley; [2]Advanced Light Source, LBL, Berkeley

(COMPRES-related facilities: ALS 12.2.2)

High-resolution X-ray diffraction with diamond-anvil cells, using argon as a quasi-hydrostatic pressure medium (axial geometry), and non hydrostatic measurements (radial geometry) documents the crystal structure and equation of state of osmium to over 60 GPa at room temperature. We minimized nonhydrostatic conditions by thermally annealing the sample at each pressure: the entire cell was heated with pressurized air to temperatures of ~40-60° C for 2-5 minutes. The observed significant decrease in pressure variations across the sample indicated diminishment of shear stresses across the sample. We find the zero-pressure bulk modulus obtained from hydrostatic data (387 (±12) GPa) as well as deduced hydrostatic data (389 (±9) GPa) from non hydrostatic radial diffraction measurements in fair agreement with other experiments as well as with relativistic electronic band-structure calculations: osmium is the densest but not the most incompressible element at ambient conditions. Cynn et al. (PRL, 2002) Obtained a value of 462 ±12 GPa for bulk modulus using argon as pressure medium. The high value for bulk modulus is possibly due to the presence of shear stresses. We find no evidence for anomalies in the ratio of unit-cell parameters, $c/a$, or in the compressibility of osmium as a function of pressure. This is in agreement with other experiments (K. Takemura, Phys. Rev. B 70, 012101, (2004)) and quantum mechanical calculations (Y. Liang and Z. Fang, J. Phys.:Condens. Matter 18, 8749 (2006)), but disagrees with recent claims that the electronic structure and equation of state of osmium exhibit anomalies at pressures of ~ 15-25 GPa (F. Occelli et al., PRL, 93, 095502, (2004)); the discrepancies are may be due to effects of texturing.
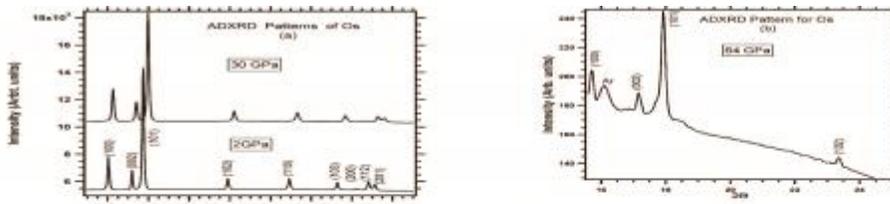


Fig. 1(a-b) Evolution of diffraction patterns of osmium as a function of pressure.
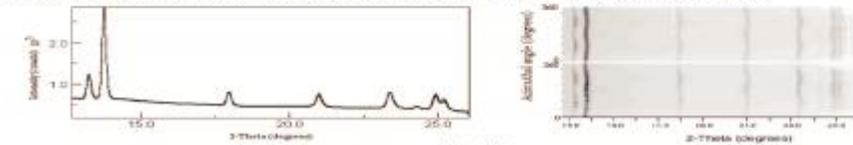


Fig. 2(a)
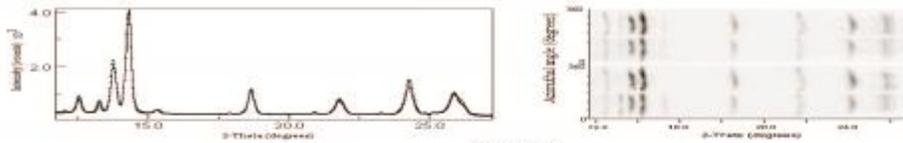


Fig. 2(b)

Fig. 2 X-ray diffraction patterns of non-hydrostatically compressed Os calculated from MAUD refinements (left), with the 2D experimental patterns (right) showing the development of texture at 5 GPa. Osmium remains in the hcp structure under these conditions
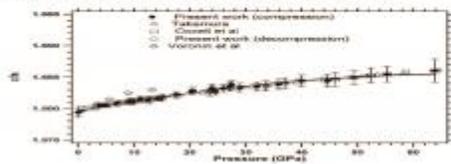


Fig. 3 Variation in c/a ratio with pressure
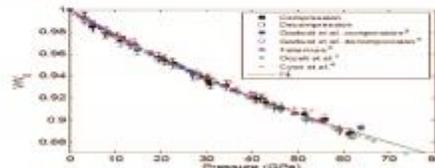
Fig. 4 Unit cell volume, V, normalized by the ambient pressure value, V0, as a function of pressure from the present study, and from previous studies

References: B.K. Godwal, J. Yan, S.M. Clark and R. Jeanloz JAP, 111, 112608 (2012), High-Pressure behavior of Osmium: An Analog for Iron in Earth's Core (Refer this for Godwal et al[3]) ; G. A. Voronin, C. Pantea, T. W. Zerda, L. Wang and Y. Zhao, Jouranl of Physics and Chemistry of Solids 66, 706 (2005); C. Pantea, et al. J. Phys. Chem. Solids 69, 211 (2008); H. Cynn, J. E. Klepeis, C. Yoo, D. A. Young, Phys. Rev. Lett. 88, 135701, (2002); R. Jeanloz and B.K. Godwal J. Phys. Conf. Series 377, 012032 (2012)

# Pressure-Induced Phase Transition in PbSe: Crystal Structure and Thermoelastic Properties

Lead selenide, PbSe, an important lead chalcogenide semiconductor, has been investigated using in-situ high-pressure/high temperature synchrotron X-ray diffraction measurements at COMPRES-supported MAC facility (X17B2-NSLS/6BMB-APS). For the first time, high-quality X-ray diffraction data were collected for the intermediate orthorhombic PbSe. Combined with ab initio calculations, we find a Cmcm, InI-type symmetry for the intermediate phase, which is structurally more favorable than the anti-GeS-type Pnma. At room temperature, the onset of the cubic−orthorhombic transition was observed at ∼3.5 GPa with a ∼3.4% volume reduction. At an elevated temperature of 1000 K, the reversed orthorhombic-to-cubic transition was observed at 6.12 GPa, indicating a positive Clapeyron slope for the phase boundary. Interestingly, phase-transition induced elastic softening in PbSe was also observed, which can be mainly attributed to the loosely bonded trigonal prisms along the b-axis in the Cmcm structure. In a comparison with the cubic phase, orthorhombic PbSe exhibits a large negative pressure dependence of electrical resistivity. In addition, thermoelastic properties of orthorhombic PbSe have been derived from isothermal compression data, such as the temperature derivative of bulk modulus and thermally induced pressure.
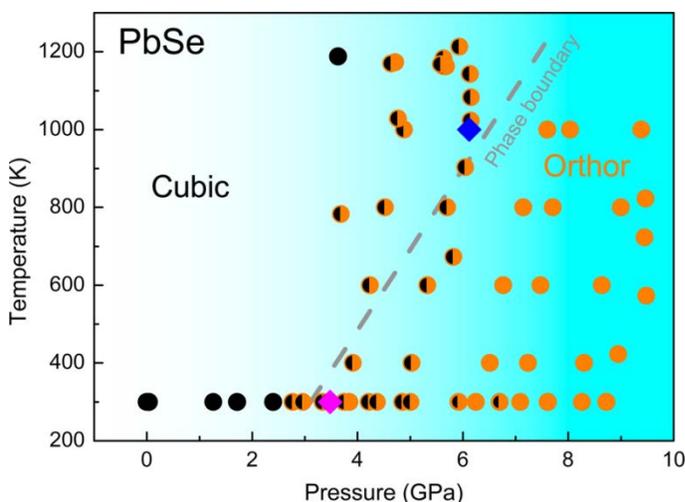


**Figure 1** Phase diagram of PbSe determined using in-situ high-P−T synchrotron XRD measurements. Black and orange solid dots represent the measured conditions for single-phase cubic- and orthorhombic-PbSe, respectively. The conditions for the co-existing phases are denoted by black−orange solid dots. During room temperature compression, the onset of the cubic → ortho transition occurs at ∼3.48 GPa (magenta diamond). During decompression, the ortho-to-cubic transformation was first observed at ∼6.12 GPa and 1000 K (blue diamond). A tentative phase boundary between the cubic and orthorhombic PbSe is delineated as a gray dashed line.
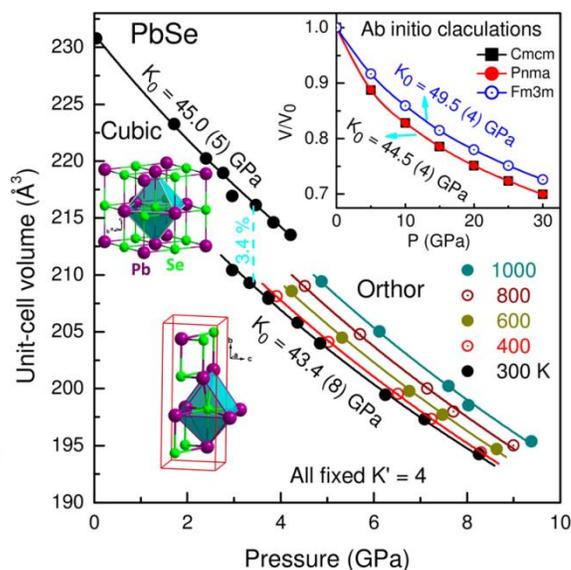


**Figure 2** Isothermal volume−pressure data of orthorhombic phase collected at 300, 400, 600, 800, and 1000 K, respectively. The volume-pressure data of cubic phase was also collected at 300 K. All data are fitted to the second-order Birch−Murnaghan equation of state. Insets are the corresponding crystal structures depicted in polyhedral views. Also shown in the upper right corner are the calculated P-V data of Cmcm and Pnma PbSe.

Wang, SM; Zang, CP; Wang,YK; Wang, LP;  Zhang, JZ; Childs, C; Ge, H; Xu, HW; Chen, HY; He, DW; Zhao, YS (2015) Revisit of pressure-induced phase transition in PbSe: crystal Structure, and thermoelastic and electrical properties. *Inorganic Chemistry*, 54, 4981-4989.

# A high-pressure far- and mid-infrared study of 1,1-diamino-2,2-dinitroethylene

Michael Pravica, Yu Liu, John Robinson, Nenad Velisavljevic, Zhenxian Liu, Martin Galley
UNLV/HiPSEC
(COMPRES-related facilities: National Synchrotron Light Source Beamline U2A)

High pressure infrared (IR) measurements of the insensitive explosive, 1,1-diamino-2,2-dinitroethylene (DADNE or FOX-7), have been performed in the far- and mid-IR spectral regions up to □28 GPa using a synchrotron source. Petroleum jelly and KBr were employed as the pressurizing media for the far- and mid-IR experiments, respectively. In both experiments, IR spectra were collected at various pressures both in compression and decompression to determine reversibility under pressure cycling. There is evidence for at least two and possibly three phase transitions in the samples at pressures near 2, 5, and 10 GPa, respectively. In the high frequency region (□3000–3300 cm□1), the $NH_2$ symmetric and antisymmetric vibrational modes soften with increasing pressure, suggesting strengthening intermolecular hydrogen bonding, and then stiffen with further pressure increase. At higher pressures (above 5 GPa), we suspect progressive flattening of the zig zag structure characteristic of the a phase occurs, which was observed in the low temperature, quenched c phase. FOX-7 was also observed to survive pressure cycling up to 28 GPa contrary to earlier reports of pressure-induced molecular decomposition. Based on this study, we proposed that FOX-7 flattens with pressure which has recently been confirmed. Here, we report the first high pressure far-IR and mid-IR studies of this relatively novel and potentially useful energetic material to the best of our knowledge.
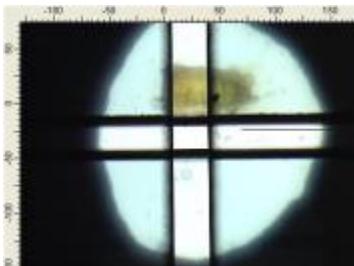


**Figure 1.** The yellow FOX-7 sample in KBr pressurizing medium at 28 GPa (as viewed through one diamond using the IR microscope). Transparent KBr fills the sample hole. Spatial optical filtering is employed via the overlayed cross-hatching pattern near the microscope objective as seen in the figure. In this snapshot, background is collected from the open rectangle displayed in the center. A small ruby sphere is seen just below this rectangle. The x- and y-grid units displayed are in microns.
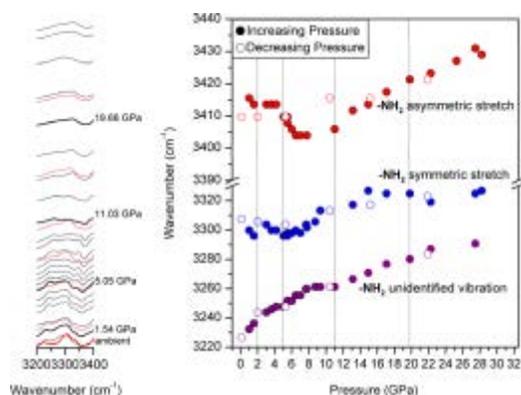


**Figure 2.** $NH_2$ symmetric stretch **(bottom)** and $NH_2$ antisymmetric stretch **(top)** frequencies as a function of pressure demonstrating phase transitions and the peculiar behavior of FOX-7 at high pressure which we ascribe to the effects of hydrogen bonding and flattening of the "zig zag" unit cell pattern with pressure .

**References:** M. Pravica, Y. Liu, J. Robinson, N. Velisavljevic, Z. Liu, M. Galley, ", (2012), A high-pressure far- and mid-infrared study of 1,1-diamino-2,2-dinitroethylene, *J. Appl. Phys*. **111**, pp. 103534 (1-8).

# Strength and texture of Pt compressed to 63 GPa

*S. M. Dorfman, Earth and Planetary Science Laboratory, Ecole Polytechnique Fédérale de Lausanne, Lausanne, Switzerland*

*S. R. Shieh, Department of Earth Sciences, University of Western Ontario, London, Ontario N6A 5B7, Canada*

*T. S. Duffy, Department of Geosciences, Princeton University, Princeton, NJ 08544, USA*

Platinum metal is commonly used in high-pressure experiments as a strain marker. Its face-centered cubic structure, inert chemistry and lack of phase transitions over a wide pressure range support its use as an internal pressure standard. Its high elastic anisotropy and strength make it useful for calibrating deviatoric stresses. Previous studies by X-ray diffraction produced conflicting results for the strength of Pt at high pressure, with some suggesting that its strength is anomalously high among metals despite its low shear modulus. We performed room-temperature compression experiments on Pt powder with three different grain sizes: 70 nm, 300 nm, and 2 microns. At pressures up to 63 GPa, angle- and energy-dispersive X-ray diffraction measurements were performed perpendicular to the compression axis at NSLS beamline X17C. The strength of bulk-grain-size Pt was measured to be lower than all previous observations, in accord with low shear modulus. Higher strengths were observed for smaller, nanoscale grain sizes. Strength and textural differences support grain-size-dependence of deformation mechanism of the polycrystalline sample.
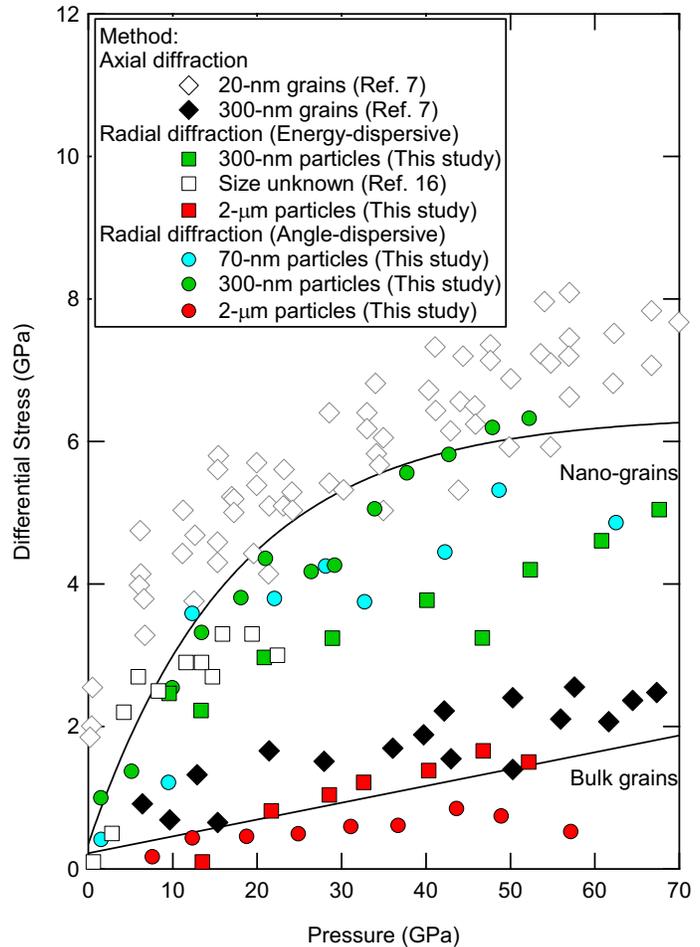


**Figure 1: Differential stress supported by platinum of 20-2000 nm grain sizes as measured by axial and radial diffraction techniques.**

Reference: Dorfman, S.M., Shieh, S.R., and Duffy, T.S. (2015). Journal of Applied Physics, 117, 065901.

# High-pressure study of rubidium azide by Raman and Infrared Spectroscopies

Dongmei Li, Fangfei Li, Yan Li, Xiaoxin Wu, Guangyan Fu, Zhenxian Liu (GL-CIW), Xiaoli Wang, Qiliang Cui, and Hongyang Zhu, Jilin University

(COMPRES-related facilities: NSLS, U2A Beamline at Brookhaven National Laboratory)

We report the high-pressure studies of $RbN_3$ by Raman and IR spectral measurements at room temperature with the pressure up to 28.5 GPa and 30.2 GPa, respectively. All the fundamental vibrational modes were resolved by combination of experiment and calculation. Detailed spectroscopic analyses reveal two phase transitions at ~ 6.5 and ~16.0 GPa, respectively. Upon compression, the shearing distortion of the unit cell induced the displacive structural transition of phase $\alpha \rightarrow \gamma$. Further analyses of the mid-IR spectra indicate the evolution of $N_3^-$ with the arrangement sequence of orthogonal $\rightarrow$ parallel $\rightarrow$ orthogonal during the phase transition of phase $\alpha \rightarrow \gamma \rightarrow \delta$. Additionally, the pressure-induced non-linear/asymmetric existence of N=N=N and the two crystallographically nonequivalent sites of $N_3^-$ were observed in phase $\delta$.
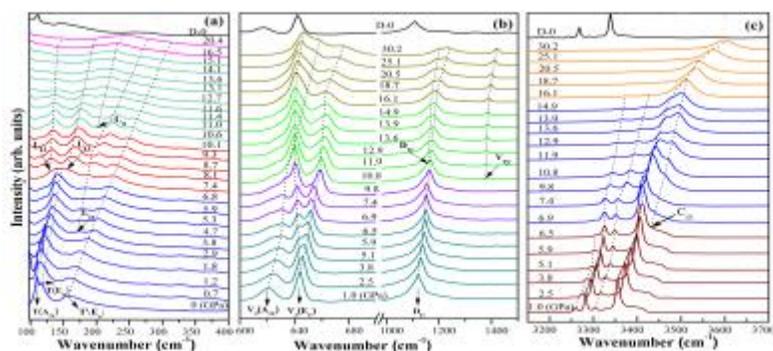


**Figure 1.** Selected high-pressure IR spectra of $RbN_3$ in the region of Far-IR (a) 100-390 $cm^{-1}$ and mid-IR (b) 600-1500 $cm^{-1}$ and (c) 3150-3700 $cm^{-1}$. The dashed lines serve as visual guides. D-0 stands for the pressure rel eased to 0 GPa.
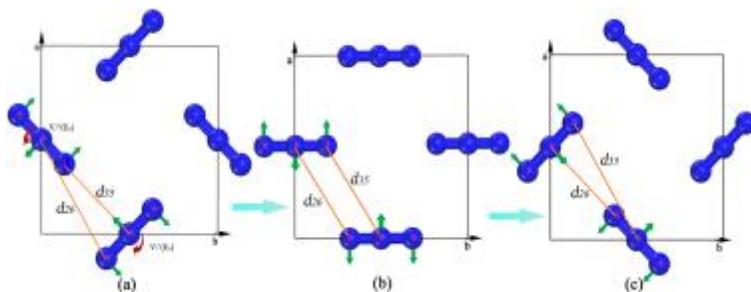


**Figure 2.** The simulated diagram of the evolution of the $N_3^-$ with increasing pressure. The green arrows indicates the vibrational direction of the atom. (a), (b), and (c) correspond to the projections of arrangement of $N_3^-$ in $a$-$b$ plane in phase $\alpha$, $\gamma$, and $\delta$, respectively.

**References:** Dongmei Li, Fangfei Li, Yan Li,‡Xiaoxin Wu, Guangyan Fu, Zhenxian Liu, Xiaoli Wang, Qiliang Cui, and Hongyang Zhu*, (2015), High-pressure study of rubidium azide by Raman and Infrared Spectroscopies, *The Journal of Physical Chemistry C.,* **119**, pp. 16870-16878.

# Bulk Signatures of Pressure---Induced Band Inversion and Topological Phase Transitions in $Pb_{1-x}Sn_xSe$

The characteristics of topological insulators are manifested in both their surface and bulk properties, but the latter remain to be explored. In this paper, the authors report bulk signatures of pressure-induced band inversion and topological phase transitions in $Pb_{1-x}Sn_xSe$ ($x = 0.00$, $0.15$, and $0.23$). The results of infrared measurements as a function of pressure indicate the closing and the reopening of the band gap as well as a maximum in the free carrier spectral weight. The enhanced density of states near the band gap in the topological phase gives rise to a steep inter-band absorption edge. The change of density of states also yields a maximum in the pressure dependence of the Fermi level. Thus, the conclusive results provide a consistent picture of pressure-induced topological phase transitions and highlight the bulk origin of the novel properties in topological insulators.
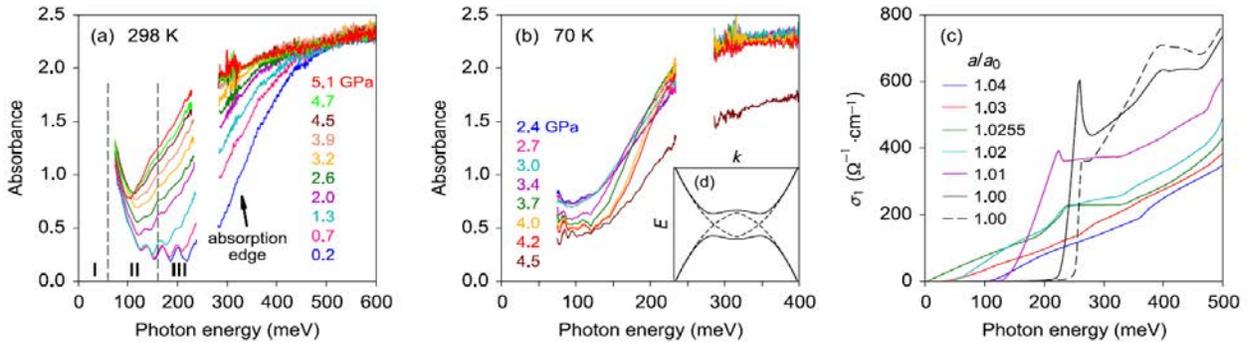


Figure. 6. Pressure-dependent mid-infrared absorbance of PbSe measured at (a) 298 K and (b) 70 K. Data in the blank region between 200–300 meV are not shown because of unreliability caused by diamond absorption. (c) Real part of the interband optical conductivity σ1 of intrinsic PbSe at various $a=a_0$ from first-principles calculations. The dashed line shows the result including holes with a density of $1018$ $cm^{-3}$. (d) [inset to (b)] A diagram illustrating hybridization opens up a band gap (in the bands shown as solid lines) when the conduction band and valence band cross (dashed lines).

**Reference:** Xi X, He X-G, Guan F, Liu Z, Zhong R D, Schneeloch J A, Liu T S, Gu G D, Xu D, Chen Z, Hong X G, Ku W and Carr G L 2014 Bulk Signatures of Pressure-Induced Band Inversion and Topological Phase Transitions in $Pb_{1-x}Sn_xSe$ *Phys. Rev. Lett.* **113** 096401

# Swift heavy ion-induced phase transformation in Gd₂O₃

The authors report that the crystalline-to-crystalline phase transformation of cubic $Gd_2O_3$ induced by swift Au ions with a kinetic energy of 2.25 GeV, has been characterized by synchrotron X-ray diffraction experiments (XRD) as a function of increasing fluence, up to $5 \times 10^{13}$ ions/cm². The diffraction maxima of the initial cubic structure gradually decrease in intensity as function of ion fluence, concurrent with the in-growth of several new diffraction peaks, which, based on Rietveld refinement, correspond to the monoclinic high-temperature phase. The same cubic-to-monoclinic phase transformation induced by swift heavy ions has been observed in $Y_2O_3$. The transformation pathway under irradiation is consistent with the high-temperature behavior of $Gd_2O_3$, and is probably associated with a multiple ion-impact mechanism. There was no evidence of amorphous material in the diffraction patterns, even after irradiation to the maximum fluence, at which the initial cubic phase has been completely transformed to the monoclinic structure.
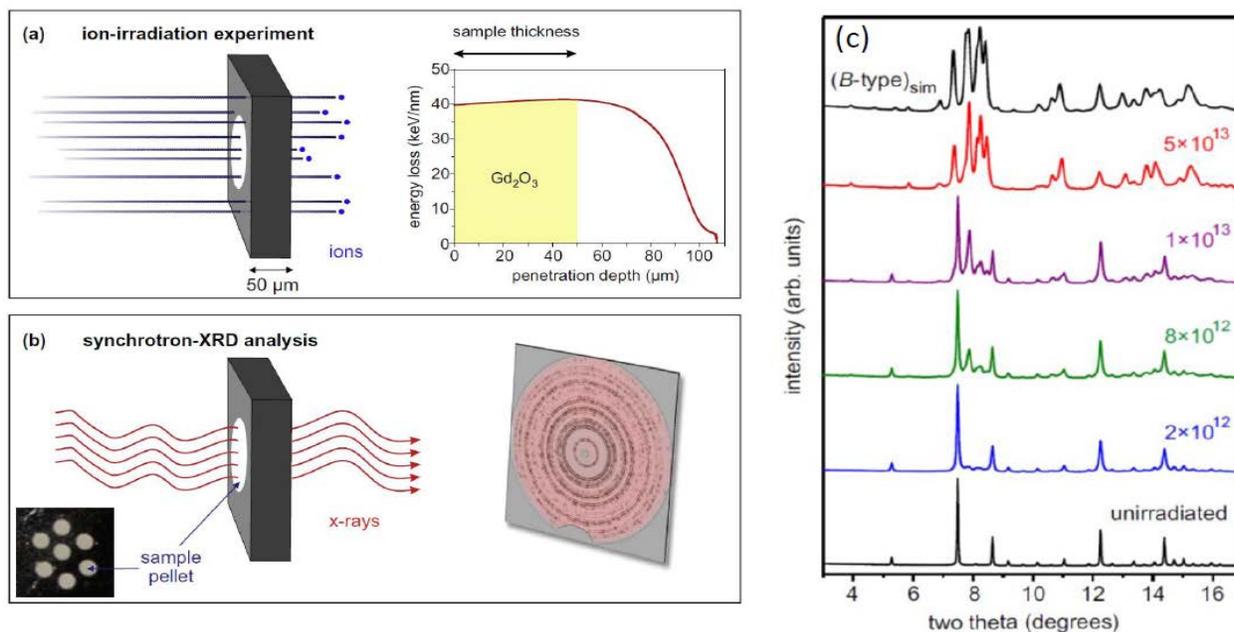


Figure 7. (a) Swift Au ions of 2.25 GeV kinetic energy completely penetrate the (white) powder sample pressed into a thin steel foil; (b) Powder X-ray diffraction experiments with 30.5 keV X-rays to study ion-induced structural modifications throughout the sample thickness; (c) Synchrotron X-ray diffraction patterns of Gd2O3 before and after irradiation with 2.25 GeV Au ions.

**Reference:** Lang M, Zhang F, Zhang J, Tracy C L, Cusick A B, VonEhr J, Chen Z, Trautmann C and Ewing R C 2014 Swift heavy ion-induced phase transformation in Gd₂O₃ *Nuclear Instruments and Methods in Physics Research Section B: Beam Interactions with Materials and Atoms* **326** 121–5

# Structural phase transition of BaZrO3 under high pressure

The authors report the phase transition behavior of cubic BaZrO$_3$ perovskite by *in situ* high-pressure synchrotron X-ray diffraction experiments up to 46.4 GPa at room temperature. The phase transition from the cubic phase to the tetragonal phase was observed in BaZrO$_3$ for the first time, which takes place at 17.2 GPa. A bulk modulus 189(26) GPa for cubic BaZrO$_3$ is derived from the pressure–volume data. Upon decompression, the high-pressure phase transforms into the initial cubic phase. It is suggested that unstable phonon modes caused by the rotation of oxygen octahedra plays a crucial role in the high-pressure phase transition behavior of BaZrO$_3$.
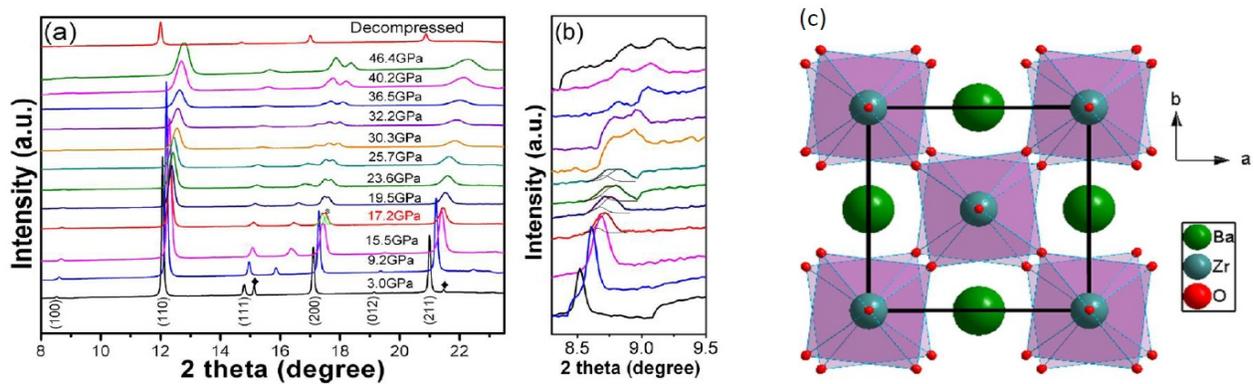


Figure 8. (a) Selected XRD patterns of BaZrO$_3$ as a function of pressure upon compression up to 46.4 GPa; (b) The enlarged pattern in the region of 8–9.5 of BaZrO$_3$. The asterisk denotes the new peak. The peaks marked by the diamond denote the unknown peaks; (c) Schematic representation of BaZrO$_3$ in I4/mcm space group structure with oxygen octahedra rotation. View along the c direction, where the out-of-phase tilting of oxygen octahedra occurs.

**Reference:** Yang X, Li Q, Liu R, Liu B, Zhang H, Jiang S, Liu J, Zou B, Cui T and Liu B 2014 Structural Phase Transition of BaZrO$_3$ under High Pressure *Journal of Applied Physics* **115 (** 12): 124907:1-5

# Pressure-induced phase transitions in rubidium azide: Studied by in-situ x-ray diffraction

The authors present the in-situ X-ray diffraction studies of $RbN_3$ up to 42 GPa at room temperature to supplement the high-pressure exploration of alkali azides. Two pressure-induced phase transitions of α-$RbN_3$ → γ-$RbN_3$ → δ-$RbN_3$ were revealed at 6.5 and 16.0 GPa, respectively. During the phase transition of α-$RbN_3$ → γ-$RbN_3$, lattice symmetry decreases from a fourfold to a twofold axis accompanied by a rearrangement of azide anions. The γ-$RbN_3$ was identified to be a monoclinic structure with *C2/m* space group. Upon further compression, an orthogonal arrangement of azide anions becomes energetically favorable for δ-$RbN_3$. The compressibility of α-$RbN_3$ is anisotropic due to the orientation of azide anions. The bulk modulus of α-$RbN_3$ is 18.4 GPa, quite close to those of $KN_3$ and $CsN_3$. By comparing the phase transition pressures of alkali azides, their ionic character is found to play a key role in pressure-induced phase transitions.
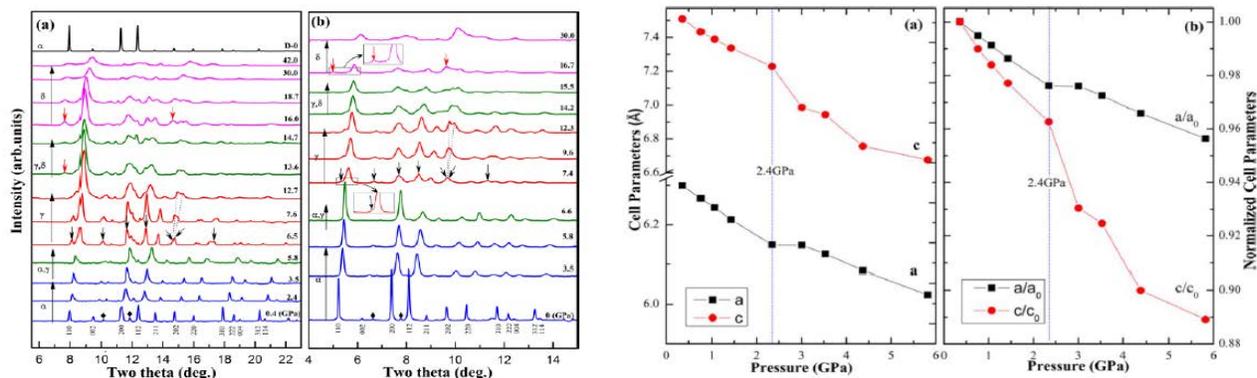


Figure 9. Left panel: Representative the XRD patterns of $RbN_3$ at various pressures. Wavelengths of X-ray used in (a) 0.6199 Å and (b) 0.4066 Å. The arrows (↓) denote the new peaks of high pressure phases. The diamonds (◆) denote the peaks of the unidentified impurity, and dashed lines serve as visual guides for these two neighboring peaks. Insets in (b): blowup of the Bragg peaks in orthogons. Right panel: Pressure dependence of the cell parameters. (b) Compression ratio ( $a/a_0$, $c/c_0$ ) of α-$RbN_3$.

**Reference:** Li D, Wu X, Jiang J, Wang X, Zhang J, Cui Q and Zhu H 2014 Pressure-induced phase transitions in rubidium azide studied by in-situ x-ray diffraction Applied Physics Letters 105 071903

# Synergetic effect of VOx and TeOx species in mesoporous SiO2 on selective oxidation of propane to acrolein

Lei Shi, Xue-Quan Zhu, Yuan Su, Wei-Zheng Weng, Huan Feng, Xiao-Dong Yi, Zhen-Xian Liu Hui-Lin Wan (Xiamen University, China)

(COMPRES-related facilities: National Synchrotron Light Source Beamline U2A)

A mesoporous silica with incorporated vanadium (V) and tellurium (Te) (3%VTezOx-MS; z = 0–0.33), synthesized by an evaporation-induced self-assembly route, was used as a model catalyst to investigate the synergetic effect of VOx and TeOx species on propane oxidation to acrolein. It was found that V in the catalyst was predominantly present as a highly dispersed $VO_4$ species, while Te existed as a highly dispersed TeOx species when the Te/V atomic ratio was below 0.2. Acrolein formation rate was positively correlated with TeOx content when both VOx and TeOx in the catalysts were in a highly dispersed state. Study of the propane oxidation pathways further indicated that highly dispersed $VO_4$ in close contact with highly dispersed TeOx constituted the active sites for direct oxidation of propane to acrolein. These binary sites satisfied all the required functions for the reactions, including consecutive sequence of activation of propane and propylene intermediate followed by inserting oxygen into the as-formed allylic species.
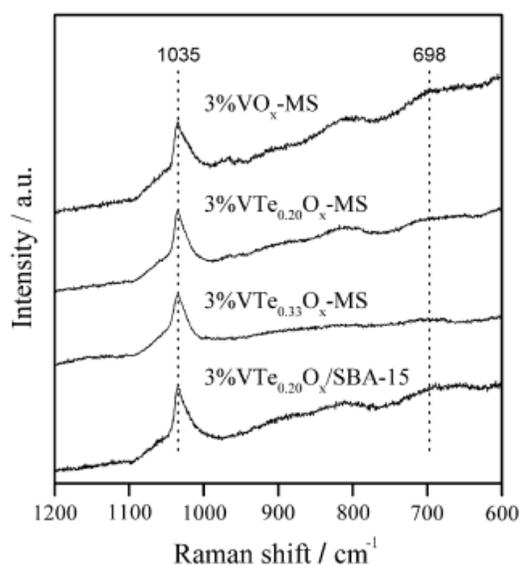


Fig. 1. Raman spectra of the 3%VTezOx-MS (z = 0–0.33) and 3%VTe0.20Ox/SBA-15 catalysts under dehydrated conditions.
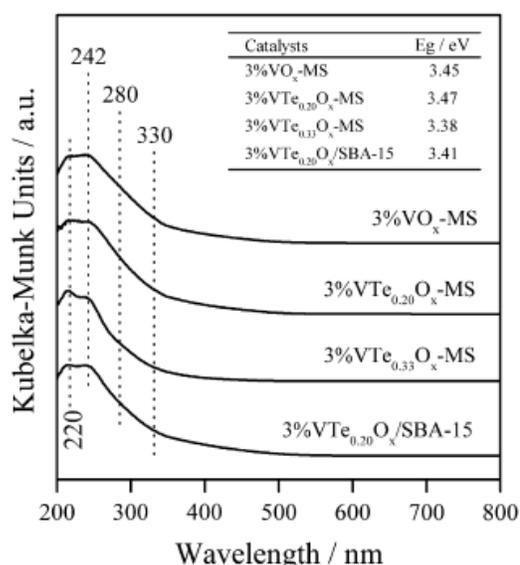
Fig. 4. UV–vis DRS spectra of the %VTezOx-MS (z = 0–0.33) and 3%VTe0.20Ox/SBA-15 catalysts under dehydrated condition, and the absorption energy edge (Eg) calculated from the UV–vis DRS spectra of the corresponding catalysts.

**Reference:** Shi L. Zhu X., Su Y., Weng W.-Z., Feng H., Yi X., Liu Z., Wan H. (2013) Synergetic effect of VOx and TeOx species in mesoporous $SiO_2$ for selective oxidation of propane to acrolein. Journal of Catalysis **307**, 316–326.

**Size dependent compressibility of nano-ceria: Minimum near 33 nm**

Nano-particulate versions of some materials have properties that are different from the same materials in bulk, comprised of micron-sized or larger grains. $CeO_2$ is one such material. We measured the unit cell parameter and compression of this material through an unusually complete range of grain sizes from micro to nano particulate.
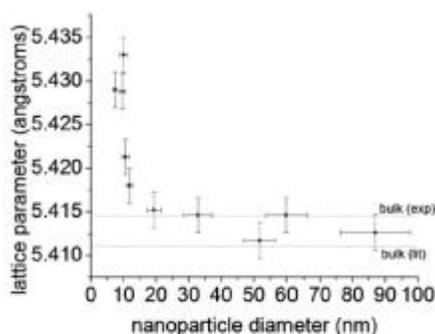


FIG. 1. Plot of crystallite diameter vs lattice parameter of nanoceria under ambient conditions. The dotted lines represent the lattice parameter of bulk ceria, both the experimental (expt.) value measured independently and the literature value (lit.).
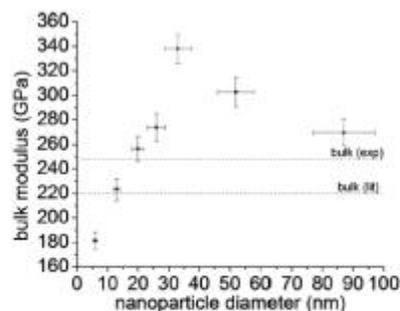


FIG. 4. Bulk modulus of nanoceria as a function of crystallite diameter, from the BM EoS calculation. The experimental bulk modulus that we have measured ourselves is represented as a dotted line labelled bulk (expt.), whereas the literature value of the bulk modulus for bulk ceria is represented as a dotted line labelled bulk (lit.). Literature bulk modulus of 220 GPa was obtained from Gerward.[24]

The bulk modulus during compression has a maximum (minimum compressibility) near 33 nm particle size. As our nano-ceria particles are confirmed to be defect free by TEM, the explanation put forward by Chen et al. (2009), based on defects in nano-anatase ($TiO_2$) with similar extremum behavior in the bulk modulus, cannot be applied to our nano-ceria. Explanations based on the anomalous lattice expansion at the smallest particle sizes observed also fail because the extremum does not fall in the same range as the anomalous expansion supposedly causing the effect on compressibility. Furthermore physical mechanisms based on anomalous expansion are quantitatively inadequate to support the large compressibility effect, even if were to occur in the correct particle size range. Instead we find that the core-shell model developed by Bian et al. (2014) for nano-galena (PbS) can provide an adequate

# Structure-Conductivity Relationships at High Pressure

Elinor C. Spencer, Victoria Soghomonian and Nancy Ross (Virginia Tech)

(COMPRES-related facilities: Advanced Light Source Beamline 12.2.2)

Electrically conducting materials are of fundamental technological importance, and understanding the often complex structure-function relationships that govern the performance of these multifunctional materials is vital for the development of new materials that exhibit desirable and exploitable properties. High-pressure single-crystal diffraction and high-pressure single-crystal conductivity measurements are needed to achieve a comprehensive appraisal of the structural features that dictate the electrical properties of such materials. We have collected data on Sr-Krettchinite (Sr-K) and MoAsC whose structures and conductivities of make them excellent candidates for testing the relationship between structure and conductivity.

The structure of Sr-K, $SrMn_2(VO_4)_2(\mu^3\text{-}OH)(\mu^4\text{-}OH_2)$, is comprised of chains of edge-sharing $MnO_6$ octahedra running parallel to [010] that are cross-linked by $VO_4$ tetrahedra to give 2D layers that lie parallel to (001). Sr cations reside between the layers. The cross-linked chain structure leads to pronounced anisotropic electrical conductivity (Fig. 1) with the most conductive along [010], parallel to the direction of the chains of edge-sharing $MnO_6$ octahedra, and less conductive in directions perpendicular to the chains. The correlation between the structural features of Sr-K and its directional-dependent electrical properties make this material an excellent candidate for investigating the structure / conductivity relationship at high pressure and whether distortions within the chains lead to a pronounced effect on the conductivity of Sr-K.
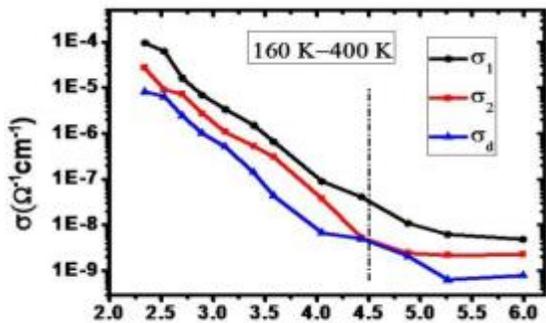


**Fig. 1.** Electrical conductivity of Sr-K: $\sigma_1$ = conductivity along [010]; $\sigma_2$ = conductivity along [100]; $\sigma_d$ = conductivity ca. along [110].

The second material is MoAsC, comprised of $[Mo_{18}As_{2.42}O_{62}]^{4-}$ clusters (Fig. 2). Protonated piperazine cations, $[C_4N_2H_{12}]^{2+}$ reside between the clusters. Intriguingly, the shortest distance between neighboring clusters is only 2.9 Å. The shortness of this distance is postulated to be critical for explaining the observed conductivity of this material. Under moderate pressures (< 5 GPa), the clusters are unlikely to deform significantly due to the rigidity of the component polyhedra and their connectivity, but rather the packing arrangement of the clusters and counterions is likely to alter. Indeed, as the clusters are close together under ambient conditions, one must expect phase transitions to occur as electronic repulsion between the charged molecules becomes significant as they are forced together with increasing pressure. Such substantial adjustments to the crystal structure will have a strong influence on the electrical conductivity of the material. Analyses of high-pressure data are underway to confirm this hypothesis.
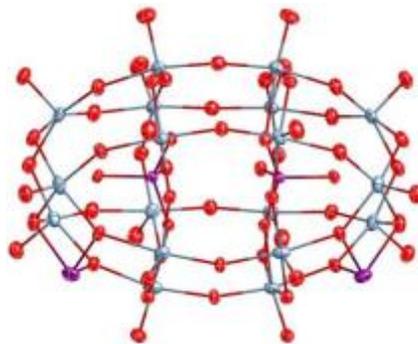


**Fig. 2.** Structure of Mo/As cluster in MoAsC. Blue: Mo; Purple: As; Red: O.

# Yield Strength of Ni-Al-Cr super alloy under pressure

S.V. Raju[1], B.K. Godwal[2], J. Yan[3], R. Jeanloz[2], S. K .Saxena[1]

[1]Florida International University, Miami; [2]University of California, Berkeley; [3]Advanced Light Source, LBL, Berkeley

(COMPRES-related facilities: ALS 12.2.2)

Ni based superalloy Ni-Al-Cr with γ and γ' phase was studied under high pressure up to 30 GPa using diamond anvil cell technique. In-situ x-ray diffraction data was collected on these alloys at beamline 12.2.2 of Advanced Light Source at LBL under hydrostatic and non-hydrostatic conditions in axial geometry. Cubic phase remains stable up to the highest pressure of about 30 GPa studied (Figs. 1 and 2). Bulk modulus and its pressure derivative obtained from the volume compression of pressure data (Fig.3) are K= 166.6± 5.8 GPa with K' set to 4 under hydrostatic conditions and K= 211.3 ±4.7 GPa with K' set to 4 for non-hydrostatic conditions. Using lattice strain theory, maximum shear stress 't' was determined from the difference between the axial and radial stress components in the sample. The magnitude of shear stress suggests that the lower limit of compressive strength increases with pressure and shows maximum yield strength of 1.8±0.3 GPa at 20 GPa (Fig.5). Further, we have also determined yield strength using pressure gradient method (Fig.4). In both the methods, yield strength increases linearly with applied pressure. The results are found to be in good agreement with each other and with literature values at ambient conditions.
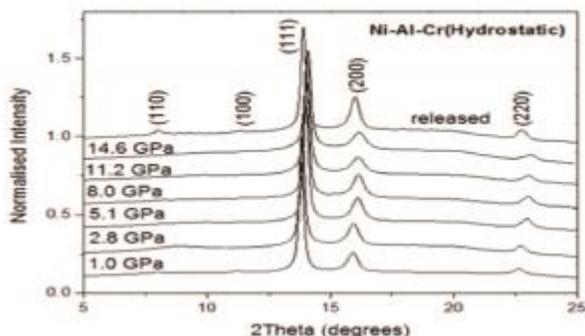


Fig. 1 X-ray diffraction data of Ni-Al-Cr collected at WL 0.4959A at various pressures under hydrostatic conditions.
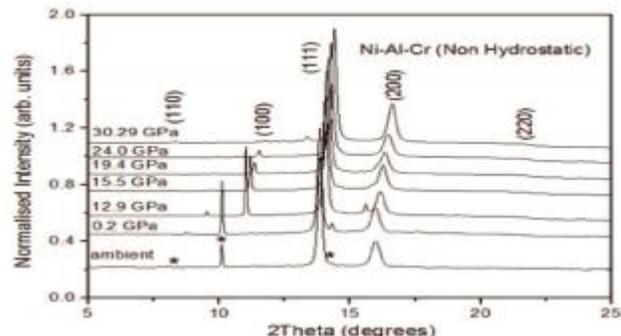


Fig. 2 X-ray diffraction pattern of Ni-Al-Cr (7.5 at %) at various pressures under non-hydrostatic conditions with at wavelength of WL 0.4959A. Asterisk sign represents line positions of NaCl which is used to determine pressure at each step from using its equation of state [28]. Ni-Al-Cr peak (220) is weak due to preferred orientation.
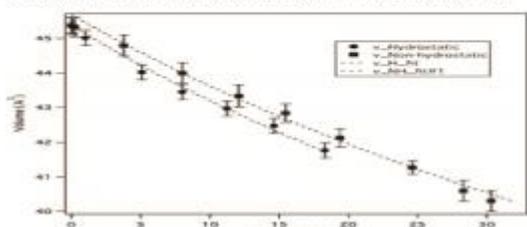


Fig.3 Pressure vs. volume data obtained for Ni-Al-Cr under hydrostatic and non-hydrostatic conditions is represented by solid circles and squares rspectively. Broken lines represent their corresponding fits obtained using Birch-Murnaghan EOS.
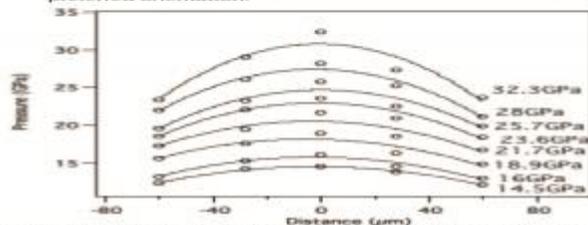


Fig. 4. Mean stress distribution across the Ni-Al-Cr alloy under non-hydrostatic conditions. Pressure at each radial position across the sample relative to the center of the sample chamber is indicated by each individual point as determined by using ruby fluorescence method on the diamond sample interface. Each curve was obtained at the average sample pressure indicated.
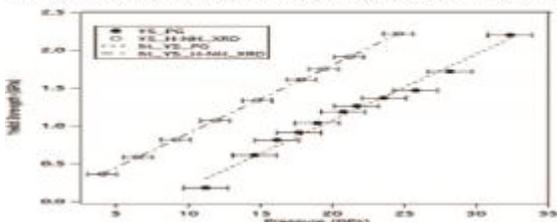


fig.5 Comparison of yield strength versus applied load. Solid circles represent data obtained from hydrostatic and non-hydrostatic equations of state (P-V relations) and open circles are obtained using by pressure gradient method

References: S.V. Raju, B.K. Godwal, J. Yan, R. Jeanloz, S. K .Saxena, Journal of Alloys and Compounds 657, 889 (2016), Yield Strength of Ni-Al-Cr super alloy under pressure

# Thermal equation of state and thermodynamic Grüneisen parameter of beryllium metal

Beryllium (Be) has been a challenging system for theoretical modeling, especially its properties under high pressure. Equation of state (EOS) and associated thermodynamic data such as Grüneisen parameter are fundamental properties of condensed matter. In the case of beryllium, because of its simplicity in electronic structure, these properties can provide crucial test for the lattice-dynamical models and schemes currently utilized in electronic structure calculations. Thus far, however, only room-temperature EOSs have been reported in literature. In the absence of temperature as an important thermodynamic parameter, significant source of uncertainties could be introduced in the density calculations and associated predictive modeling. In this study, we conducted synchrotron x-ray diffraction on alpha-Be at pressures up to 7.9 GPa and temperatures up to 1373 K at COMPRES-supported MAC facility (X17B2-NSLS/6BMB-APS). A complete pressure ($P$)–volume ($V$)–temperature ($T$) equation of state (EOS) is determined based on the experiment, which includes temperature derivatives of elastic bulk modulus (at both constant pressure and constant volume) and pressure dependence of thermal expansivity. From this EOS, we calculate thermal pressure, heat capacity at constant volume, and thermodynamic Grüneisen parameter as a function of temperature. Above 600 K, our results show notable deviation from theoretical predictions using the quasi-harmonic and local-density approximations, indicating that the free energy calculations need to be further improved within the current scheme of approximations.
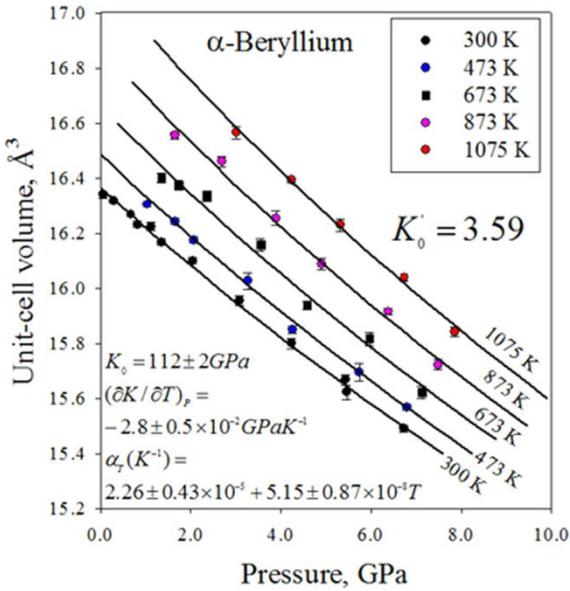


**Figure 1** Pressure-volume-temperature data measured for the alpha-phase of beryllium. The curves represent results of the least-squares fit using a modified high-temperature Birch-Murnaghan equation of state at the indicated isotherms.

Zhang, JZ; Zhu, JL; Velisavljevic, N; Wang, LP; Zhao, YS (2013) Thermal equation of state and thermodynamic Grüneisen parameter of beryllium metal. *Journal of Applied Physics*, 113, 203520.
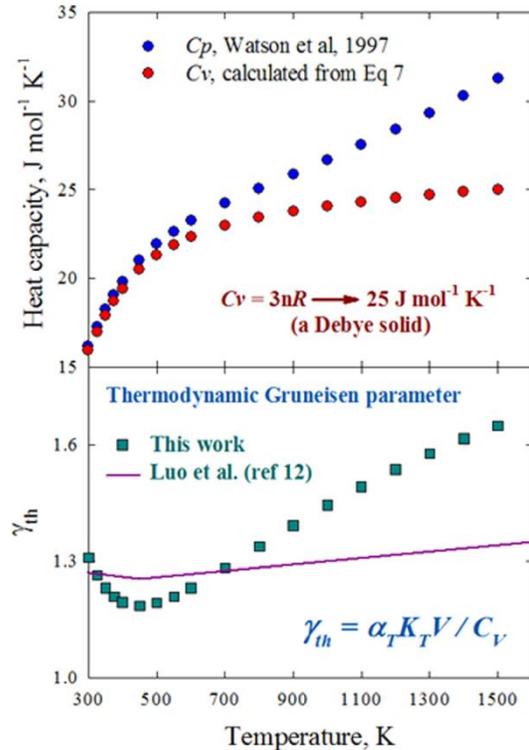
**Figure 2** Heat capacity and Grüneisen parameter plotted as a function of temperature for alpha-Be at ambient pressure. The experimental $C_P$ is from the work of Watson *et al.*. The Grüneisen parameters obtained from DFT calculations are shown by a solid curve.

# Immobilization of Large, Aliovalent Cations in the Small Pore Zeolite K-Natrolite Using Pressure

Yongjae Lee,* Yongmoon Lee, Donghoon Seoung, Jun-Hyuk Im, Hee-Jung Hwang, Tae-Hyun Kim, Dan Liu (YONSEI UNIVERSITY, KOREA), Zhenxian Liu (GL-CIW, USA), Seung Yeop Lee (Korea Atomic Energy Research Institute, Korea), Chi-Chang Kao (SLAC, USA), Thomas Vogt (USC, USA)

(COMPRES-related facilities: National Synchrotron Light Source Beamline U2A)

Selective ion-exchange is one of the fundamental properties of zeolites enabling various environmental and industrial applications. The ion exchange selectivity of a zeolite is controlled in part by the geometry of the pores and channels where exchanging cations diffuse through and bind via the framework oxygen atoms. Most studies on the ion-exchange properties of zeolites have been carried out near ambient conditions to establish the selectivity series between mono- and divalent cations and to a lesser extent, for trivalent cations such as lanthanides and actinides. We utilize the auxetic properties of the small-pore zeolite natrolite framework to exchange under pressure and trap at ambient conditions formally thought non-exchangeable trivalent cations such as lanthanides in potassium-natrolite. Here, we show, using in-situ diffraction, spectroscopy and ex-situ high-pressure synthesis, that trivalent europium cations can be trapped in the natrolite framework, i.e., over 90% Eu(III) exchange level was achieved in the P-T range of 3 GPa and 250°C.
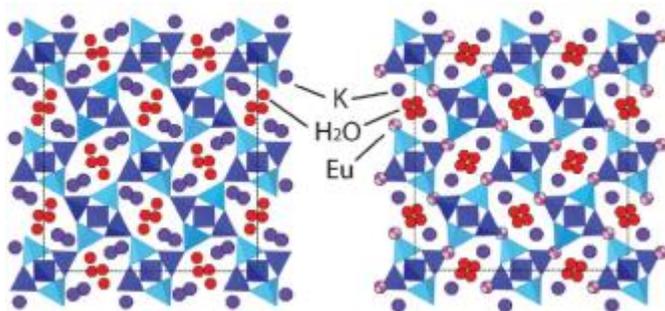


**Figure 1.** TOP: Polyhedral representations of K-natrolite at ambient pressure (left) and under 1.0M Eu(III) solution medium at 1.5 GPa (right), viewed along [001], the chain/channel axis. Note that europium cations partially occupy a site distinctive from the potassium cations and water molecular sites. Dark (light) tetrahedra illustrate an ordered distribution of Si (Al) atoms in the framework. Bottome: Pressure-dependent changes of the refined cation content of K-NAT in 1.oM Eu(III) solution.
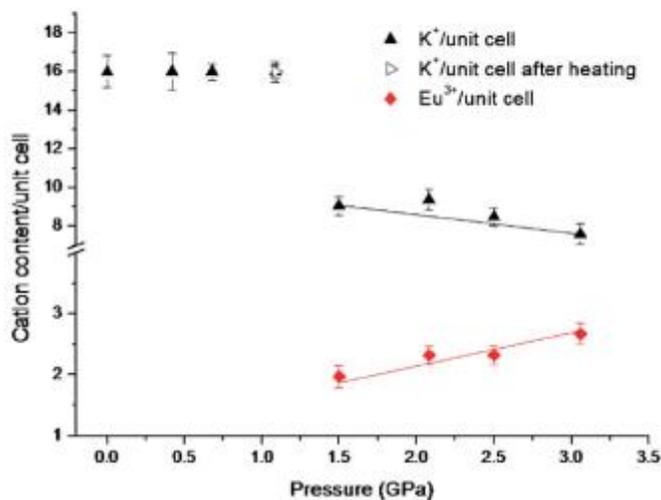
**References:** Y. Lee,* Y. Lee, D. Seoung, J.-H. Im, H.J. Hwang, T.H. Kim, D. Liu, Z. Liu, S.Y. Lee, C.-C. Kao, T. Vogt, (2012), Immobilization of Large, Aliovalent Cations in the Small-Pore Zeolite K-Natrolite by Means of Pressure, Angewandte Chemie International Edition, **51**, pp.4848-4851

# Spectroscopic and Computational Characterizations of Alkaline-Earth- and Heavy-Metal-Exchanged Natrolites

D. Liu, Y. Lee* (YONSEI UNIVERSITY, KOREA), X. Chen, Y. Ma (Jilin University, China), Z. Liu (GL-CIW, USA), T. Vogt (USC, USA)

Understanding the structure and property relationship of a zeolite is crucial in many industrial and environmental applications such as ion-exchange, molecular separation, and catalysis. Although the zeolite natrolite has been regarded as one of the model zeolites possessing a relatively simple framework structure, its ion-exchange property and resulting structural changes have evaded complete understanding since its first discovery in 1803. Researchers at Yonsei University have established an important synthetic route to broaden the ion-exchange capabilities in natrolite and reported its comparative structural chemistry in a series of papers (Am. Mineral., 2010, 2011; J. Phys. Chem. C 2013). In this work, the collaboration between the four research groups has linked the established systematic structural variations of ion-exchanged natrolites to their spectroscopic signatures so as to enable structural predictions and probe natrolites with mixed EFCs. We have found that the vibrational frequencies of both 4- and helical 8-ring units in natrolite scale with the size of the EFC and that the frequency of the H-O-H bending and O-H stretching modes of water contained within the pores are dependent on the orientations of the water molecules along the natrolite channel. Deviations from these correlations in mixed EFC natrolites could hint at new structures due to size-driven phase separations.
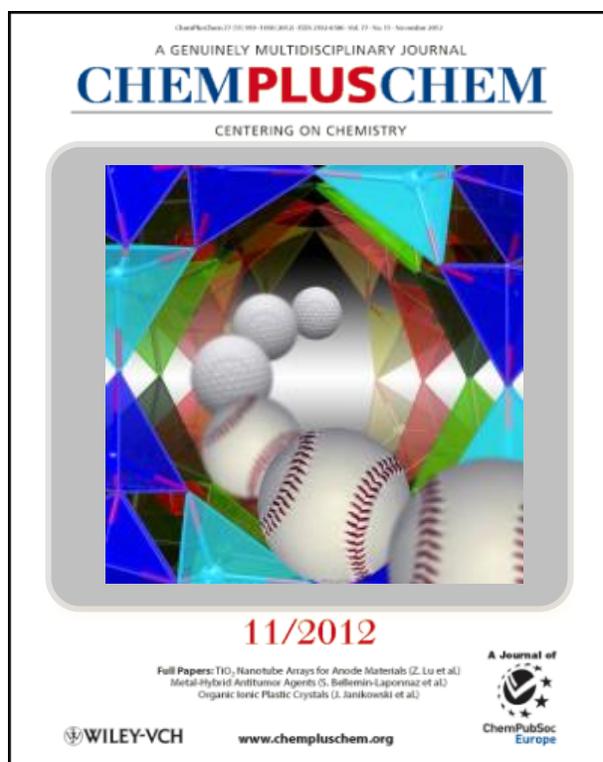


**Figure 1.** The cover picture shows the natrolite framework of a small pore zeolite made up of alternating $SiO_4$ and $AlO_4$ tetrahedral 4-rings and helical 8-rings, which can contain, via cooperative rotation of the 4-rings and subsequent modification of the 8-ring opening, monovalent alkali metals $Li^+$, $Na^+$, $K^+$, $Rb^+$ and $Cs^+$, divalent alkaline-earth ions $Ca^{2+}$, $Sr^{2+}$ and $Ba^{2+}$ as well as heavy metals like $Cd^{2+}$, $Pb^{2+}$ and $Ag^+$ as charge-balancing extra-framework cations (EFC). We have found that the vibrational frequencies of both 4- and helical 8-ring units scale with the size of the EFC and that the frequency of the H-O-H bending and O-H stretching modes of water contained within the pores are dependent on the orientations of the water molecules along the natrolite channel. Deviations from these correlations in mixed EFC natrolites could hint at new structures due to size-driven phase separations.

**References:** D. Liu, X. Chen, Y. Ma, Z. Liu, T. Vogt, Y. Lee, (2014), Spectroscopic and Computational Characterizations of Alkaline-Earth- and Heavy-Metal-Exchanged Natrolites, ChemPlusChem, **79**, pp.1096-1102.

# In-operando investigation on the reaction mechanism of sulfur electrodes for Li/S batteries by XAS

Jinghua Guo, Liang Zhang, Advanced Light Source, LBNL

COMPRES-related facility: Laser Miller at the Advanced Light Source

Sustainable and clean energy technologies are highly desirable due to the increasing global energy consumption. The rechargeable lithium/sulfur (Li/S) cell is one option and has been regarded as a cutting-edge technology. The Li/S cell has received significant attention due to the high theoretical specific capacity of 1675 mAh/g for elemental S. However, the widespread applications of the Li/S cells are limited by some issues, such as low electronic conductivity and lithium ion diffusion rate for S and sulfides, volume expansion (~76%) and polysulfide shuttle effect. To get detailed information about the S speciation in the cell and the interactions of additives and S species during the charge/discharge process, in-operando studies are highly desirable.

We have used a modified coin cell to perform such experiment, which can provide accurate information on the nature of the electrochemical processes. A 2 mm × 1 mm rectangular hole was punched with the Laser Miller at the Advanced Light Source on the stainless steel coin cell shell. The size of the hole is critical for the in-operando electrochemical cells: the X-ray absorption signal would be extremely weak if the hole is too small, and the cell will leak if the hole is too large. On the other hand, the hole with appropriate size can also eliminate the different cell structure-induced changes of the S speciation during the electrochemical process. With the help of Laser Miller, we can accurately control the size of the hole. The hole is then sealed with kapton film using epoxy, as shown in Figure 1. The modified cell can work well for tender and Hard X-ray spectroscopy.



Figure 1. Normal coin cell shell (left) and modified coin cell shell with Laser Miller (right).

# Pressure tuning the lattice and optical properties of Ag$_2$S
## Zhao Zhao, Wendy L. Mao, Stanford University

### (COMPRES-related facilities: ALS 12.2.2)

Transition metal chalcogenides have attracted increasing attention for their unique structural and electronic properties. High pressure is a powerful tool for tuning the lattice and electronic structure of transition metal chalcogenides away from their pristine states. In this work, we systematically studied the *in situ* structural and optical behavior of Ag$_2$S under pressure by synchrotron X-ray diffraction (ALS 12.2.2) and infrared spectroscopy measurements in a diamond anvil cell. Upon compression, Ag$_2$S undergoes a series of structural transitions while the crystallographic inequivalence of the two Ag sites is maintained. Electronically, pressure effectively tunes the ambient semiconducting Ag$_2$S into a metal at ~22 GPa. Drude model analysis shows that the optical conductivity evolves significantly, reaching the highest value of 100 $\Omega^{-1}$ cm$^{-1}$ at ~40 GPa. Our results highlight the structural and electronic tunability of silver chalcogenides and suggest the potential of Ag$_2$S as a platform for developing optical and opto-electronic applications.



**Figure 1.** (a) Experimental set up for high pressure X-ray and IR measurements. (b) Crystal structures for the four phases of Ag$_2$S under pressure, where two distinctive Ag sites are observed. (c) Representative high pressure XRD patterns with $\lambda = 0.3775$ Å. Numbers on the right are pressures in units of GPa. New diffraction peaks in phase II are shown by stars and phase III by diamonds.
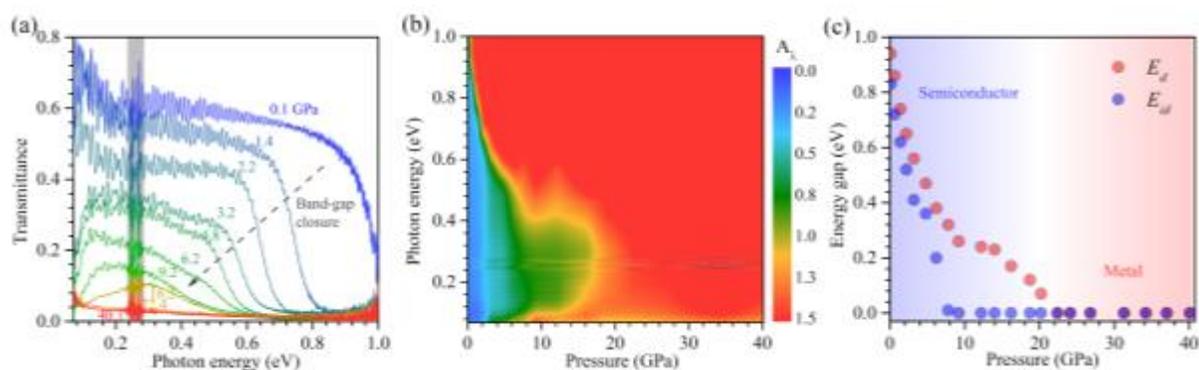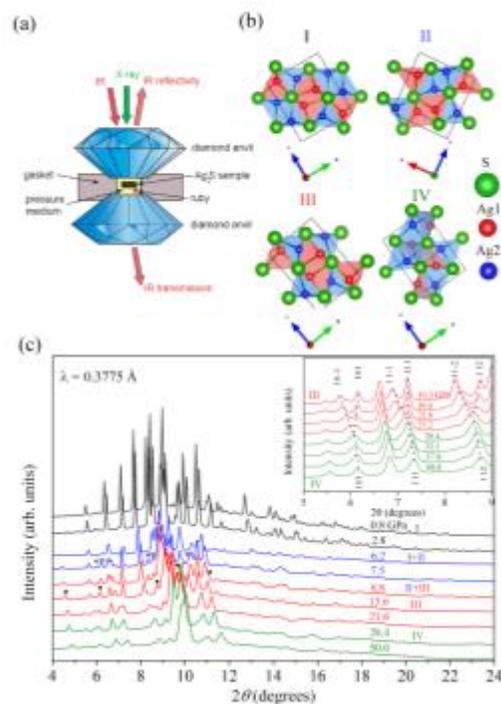


**Figure 2.** (a) Representative IR reflectance spectra at various pressures. The 0.23−0.28 eV region is obscured by absorption of the diamonds in the DAC. (b) Pressure-photon energy-optical conductivity ($\sigma$) mapping. (c) Evolution of DC conductivity ($\sigma_0$) with pressure.

References: Z. Zhao, H. Wei, W. L. Mao (2016), *Appl. Phys. Lett.* 108, 261902 (2016);

# Probing magnetic transitions in $(Mg,Fe)GeO_3$-perovskite with Mössbauer Spectroscopy

**June K. Wicks, Sally J. Tracy, Camelia V. Stan, Thomas S. Duffy** *Princeton University*
**Wenli Bi, Ercan E. Alp** *Argonne National Laboratory*

The role of Fe in bridgmanite in the deep earth can be complicated, as Fe can occupy two different crystallographic sites (A or B) and can adopt different valence states (2+,3+) and electronic configurations (high or low spin). Previous experimental and theoretical work on this material has reported a pressure-induced low- to high-QS (quadrupole splitting) transition at ~30 GPa, explained by a small lateral displacement of the $Fe^{2+}$ ion (e.g. Jackson et al., 2005, Hsu et al., 2010). A recent theoretical study predicts that in the Ge analogue, although the presence of Ge reduces the Pv->pPv transition by ~50 GPa, the low- to high-QS transition should be ~20 GPa higher in the germanate due to the larger unit cell (Shukla et al., 2015).

At the COMPRES-supported Mössbauer point source at Sector 3 of the Advanced Photon source, Argonne National Laboratory, we collected Mössbauer spectra for $(Mg_{0.8}Fe_{0.2})GeO_3$ perovskite at 39, 44, and 51 GPa (Figure, below). The sample was synthesized at 40 GPa with laser heating at Sector 13-ID-D, and the perovskite structure confirmed with X-ray diffraction. Preliminary analysis indicates predominately $Fe^{2+}$ with some $Fe^{3+}$ contribution at low pressure. With increasing pressure, we find the appearance of a third high-QS site, consistent with similar observations in the silicate.

Mössbauer Spectra of $(Mg_{0.8}Fe_{0.2})GeO_3$ perovskite collected at Sector 3, APS. These measurements were collected as anchor points for a follow-up synchrotron Mössbauer spectroscopy study. Black arrows indicate the appearance of a high-QS site at 44 GPa.
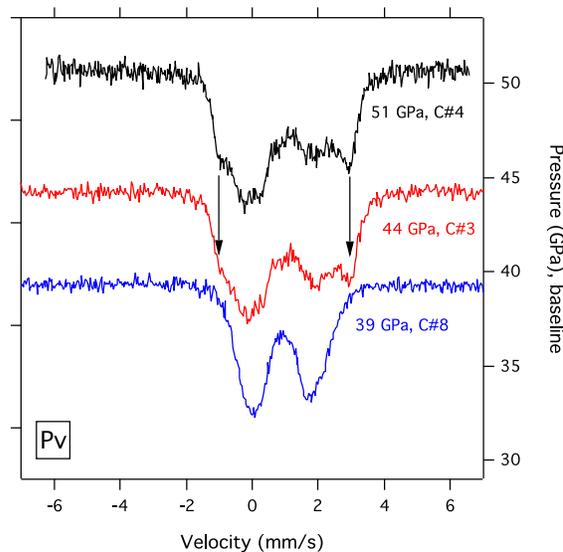
Jackson, J. M., Sturhahn, W., Shen, G., Zhao, J., Hu, M. Y., Errandonea, D., Bass, J. D., and Y. Fei (2005) A synchrotron Mössbauer spectroscopy study of (Mg,Fe)SiO3 perovskite up to 120 GPa. *Am. Min.,* 90, 199-205.

Hsu, H., Umemoto, K., Blaha, P., and R. M. Wentzcovitch (2010) Spin states and hyperfine interactions of iron in (Mg,Fe)SiO3 perovskite under pressure. *Earth Planet. Sci. Lett.*, 294, 19-26.

Shukla, G., Topsakal, M., and R. M. Wentzcovitch (2015) Spin crossovers in iron-bearing MgSiO₃ and MgGeO₃: Their influence on the post-perovskite transition. *Phys. Earth Planet. Int.*, 249, 11-17.

# Origins of ultralow velocity zones through slab-derived metallic melt

Jiachao Liu[a], Jie Li[a], Rostislav Hrubiak[b], and Jesse S. Smith[b]

[a]University of Michigan; [b]HPCAT, Geophysical Laboratory, Carnegie Institution of Washington.

(COMPRES-related facility: COMPRES gas-loading system at GSECARS)

Recent studies suggest that metallic iron and carbon are produced in subducted slabs when they sink beyond a depth of 250 km. In this experimental study the eutectic melting curve of the iron−carbon system was found to cross the geotherm near Earth's core-mantle boundary, suggesting that dense metallic melt may form in the lowermost mantle. If concentrated into isolated patches, such melt could produce the seismically observed density and velocity features of the ultralow velocity zones (ULVZs), which are localized patches sitting above the core-mantle boundary. Depending on the wetting behaviors of such metallic melt among the lowermost mantle minerals, the resultant ULVZs may be short-lived domains that are replenished or regenerated through subduction, or long-lasting regions containing both metallic and silicate melts. Slab-derived metallic melt may produce another type of ULVZ that escapes core sequestration by reacting with the mantle to form iron-rich post- bridgmanite or ferropericlase.
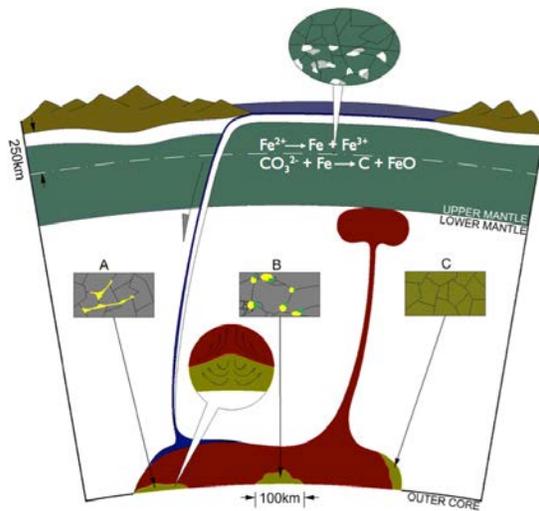


**Figure** 1: Cartoon illustration of three types of ULVZs involving slab-derived iron-carbon (Fe-C) melt (heights are exaggerated). The upper oval-shaped balloon shows that, at a depth beyond 250 km in the mantle, metallic iron (white) is produced by the disproportionation of ferrous iron in pyroxene and garnet, whereas the dominant carbon species are elemental carbon or iron carbides (gray). Three rectangular boxes represent (box A) ULVZs containing 5-11 vol. % Fe-C melt (yellow) that wets the solid silicate matrix (gray), (box B) ULVZs containing 9-16 vol.% nonwetting Fe−C melt (yellow) coexisting with a small degree of silicate melt (green) in solid silicate matrix (gray), and (box C) ULVZs containing solid phases (yellow-shaded gray) that have become iron-rich through reaction with Fe-C melt. The lower round balloon indicates that dynamic stirring through viscous coupling with the upwelling mantle may prevent or slow down the draining of dense Fe-C melt to the core.

Reference: Liu JC, Li J, Hrubiak R, & Smith JS (2016) Origins of ultralow velocity zones through slab-derived metallic melt. *Proc Natl Acad Sci USA* 113(20):5547-5551.

# Studies of Partial Melting of Peridotite at Mantle Pressures,

# Temperatures, and Frequencies

Li and Weidner have been exploring the mechanical implications of partial melting using a natural peridotite as the starting material and conducting experiments at the pressure, temperature and frequency as seismic waves in the low velocity zone.  Their work, cited in a recent paper by Anderson and King (Driving the Earth machine, 5 December 2014 • VOL 346 ISSUE 6214)

> In a remarkable series of experiments, Li and Weidner have shown that a solid with pockets of melt oriented by the shearing can produce the kind of low–wave speed, low-viscosity anisotropic material that is consistent with the observed properties of the asthenosphere. Interaction of seismic waves with this material perturbs the material and further reduces the seismic wave speed.

In their paper, Li and Weidner measure Young's modulus at seismic frequency of a partially molten peridotite as a function of the amount of melt at mantle conditions.  They model the effect of partial melting by considering the thermodynamic interaction of the solid and liquid as perturbed by an oscillating stress field.  The observations and model are expressed in the following diagrams.
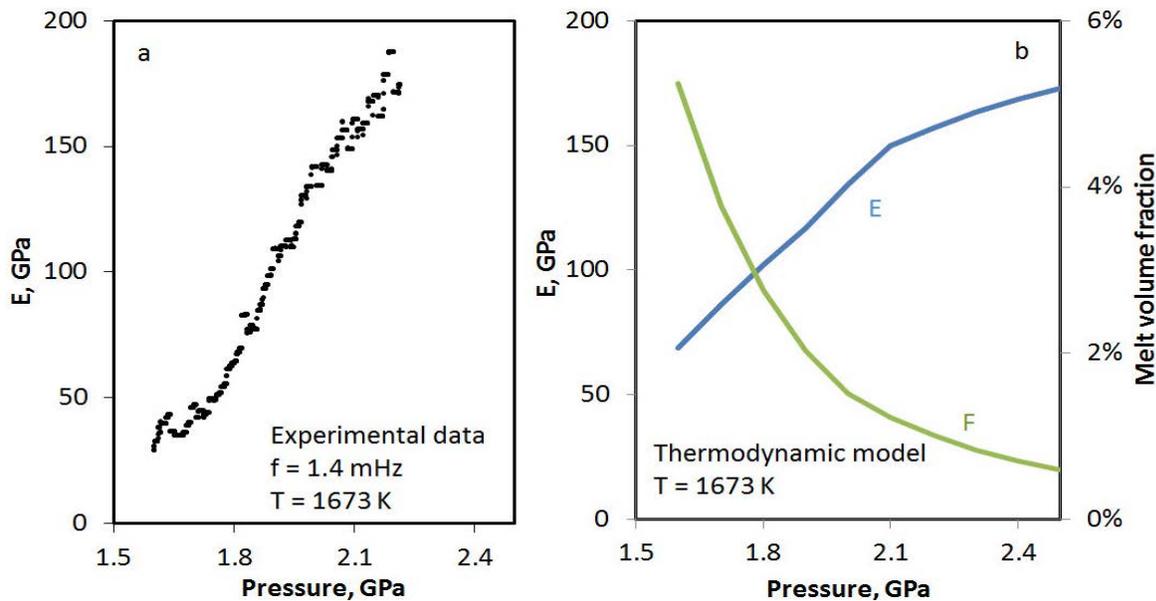


The right illustration gives the theoretical model of both the Young's modulus (E) and the fraction of melt (F).  The remarkable result is that the Young's modulus changes by a factor of three in both the data and the model for a change in the four per cent of melt.  This effect of melting on the elastic properties has not been considered before.

**Reference:** Li, L., and D. J. Weidner, Effect of Dynamic Melting on Acoustic Velocities in a Partially Molten Peridotite, Physics of the Earth and Planetary Interior, 222, 1-7, 2013

# Kinetics of Partial Melting

Partial melting in the Earth's mantle involves a combination of processes such as ionic diffusion and solid - liquid transition. These processes yield an array of characteristic times for the melting kinetics. Both the magnitude and time constant of melt-induced volume strain affect seismic velocity, attenuation, and buoyancy. In situ monitoring of samples during melting are enabled by multi-anvil high-pressure devices coupled with synchrotron x-ray radiation. In this study, the volume strain induced in a sample from melting is measured as a function of time using x-ray images. We find a doubling of the effective thermal expansion for only 2% melt both from our data and from thermodynamic models of peridotite. The characteristic time of melting is determined to be less than one second. These findings imply that seismic velocities will be sensitive to the strain related to the phase interaction induced by the stress of the seismic wave. The effect is to lower the seismic velocity.
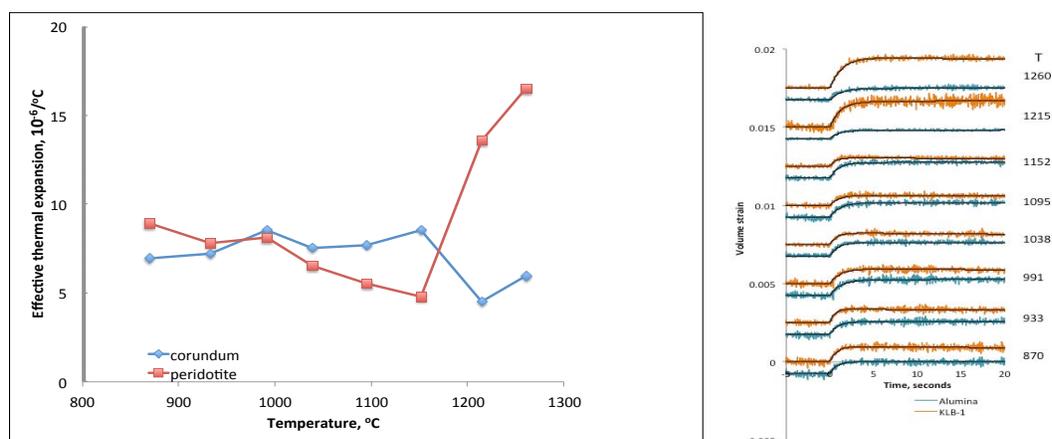


The thermal expansion of the peridotite increased by about a factor of three at the temperature corresponding to the onset of melting. On the right the time dependence of volume is illustrated for several temperatures for both the sample (salmon color) and reference corundum (blue). The rise time of the volume for an instantaneous increase of the furnace temperature reflects the time required for heat to diffuse into the sample. The rise time does not change when melting occurs, indicating that melting is instantaneous compared to the one second rise time. Thus, melting is fast enough to be induced on the 10 – 1000 second time of the seismic stress field.

**Reference:** Donald J. Weidner and Li Li, Kinetics of melting in peridotite from volume strain measurements, Phys. Earth Planet. Sci., doi:10.1016/j.pepi.2015.06.006

# Seeking Links between Structure and Physical Properties of Geo-Liquids

Yoshio Kono, Guoyin Shen (HPCAT, Carnegie Institute of Washington), Tony Yu and Yanbin Wang (GSECARS, The University of Chicago)

(COMPRES supported Paris-Edinburgh system at 16-BM-B of HPCAT, APS)

A defining characteristic of silicate melts is the degree of polymerization (tetrahedral connectivity), which dictates viscosity and affects compressibility. While viscosity of depolymerized silicate melts increases with pressure consistent with free volume theory, isothermal viscosity of polymerized melts decreases with pressure up to ~3 – 5 GPa, above which it turns over to normal (positive) pressure dependence. By combining high-pressure x-ray diffraction studies in the Paris-Edinburgh press with molecular dynamics simulations (Fig. 1), we show that the viscosity turnover in polymerized liquids corresponds to the tetrahedral packing limit, below which the structure is compressed through tightening of the inter-tetrahedral bond angle, resulting in high compressibility, continual breakup of tetrahedral connectivity, and viscosity decrease with increasing pressure. Above the turnover pressure, silicon and aluminum coordination increases to allow further packing, with increasing viscosity and density. These structural responses prescribe the distribution of melt viscosity and density with depth and play an important role in magma transport in terrestrial planetary interiors.

Knowledge of the occurrence and mobility of carbonate-rich melts in the Earth's mantle is also important for understanding the deep carbon cycle and related geochemical and geophysical processes. However, our understanding of the mobility of carbonate-rich melts remains poor. We conducted viscosity measurements on carbonate melts up to 6.2 GPa using a newly developed technique of ultrafast synchrotron X-ray imaging in the Paris-Edinburgh press. These carbonate melts, which are dominated by the $CO_3$ trigonal planar units, display ultralow viscosities in the range of 0.006-0.010 Pa s, which are ~2 to 3 orders of magnitude lower than those of basaltic melts in the upper mantle. As a result, the mobility of carbonate melts (defined as the ratio of melt-solid density contrast to melt viscosity) is ~2 to 3 orders of magnitude higher than that of basaltic melts. Such high mobility has significant influence on several magmatic processes, such as fast melt migration and effective melt extraction beneath mid-ocean ridges.

References: [1] Wang, Y., T. Sakamaki, L. Skinner, Z. Jing, T. Yu, Y. Kono, C. Park, G. Shen, M. L. Rivers, S. R. Sutton (2014) Atomistic insight into the viscosity and density behavior of silicate melts, *Nature Communications*, **5**, 3241. [2] Kono, Y., C. Kenney-Benson, D. Hummer, H. Ohfuji, C. Park, G. Shen, Y. Wang, A. Kavner, C.E. Manning (2014) Ultralow viscosity of carbonate melts at high pressures, *Nature Comms.*, **5**:5091.
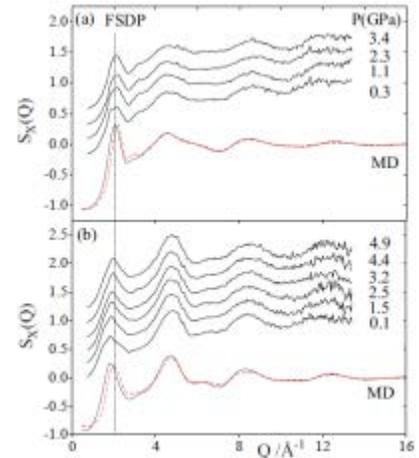
**Fig. 1**. (a) Structure factors for diopside melt. (b) Structure factor for jadeite melt. In each figure, molecular dynamics (MD) simulations at ambient pressure (black solid curve) and 5 GPa (red dashed curve) are shown below the experimental curves for comparison.
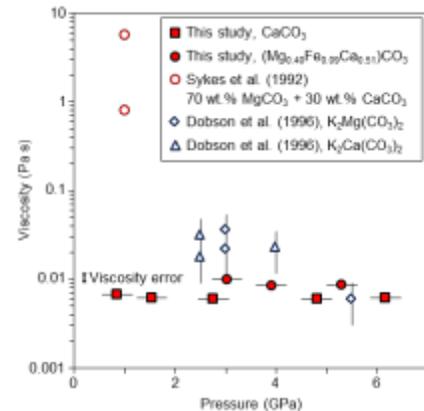


**Fig. 2**. Viscosities of calcite and dolomite melts up to 6.2 GPa along the melting curves compared with those of Ca-Mg carbonate melts and potassium carbonate melts reported previously. Error of our viscosity measurement is smaller than the size of symbol. Our viscosities of calcite and dolomite melts are 2-3 orders of magnitude lower than those of previous quench experiments.

# High pressure and temperature equation of state of cobalt oxide: Implications for redox relations in Earth's mantle

Matthew M. Armentrout, Emma S. G. Rainey, and Abby Kavner, UCLA

The high pressure and temperature equation of state of rocksalt-structured cobalt oxide was measured up to 65 GPa and 2600 K using synchrotron X-ray diffraction in conjunction with the laser heated diamond anvil cell at HPCAT, sector 16, APS and at ALS 12.2.2. We use this newly determined equation of state in conjunction with existing measurements of the thermoelastic parameters of cobalt metal to calculate the Gibbs free energy difference between the cobalt oxide and cobalt metal phases as a function of pressure and temperature. A comparison of the energetics of the Co/CoO system with the Ni/NiO system predicts that below 58 GPa CoO+Ni is stable relative to NiO+Co, while above 58 GPa the reverse is true. This tipping point in energy can be mapped as a crossing point in the electrochemical potential of the two metal ions, suggesting that the cobalt becomes more siderophile than nickel with increasing pressure. This result is in qualitative agreement with existing measurements of nickel and cobalt partition coefficients between mantle and core materials.



**Figure 1.** Representative caked diffraction patterns. Diffraction peaks for cobalt oxide (C), NaCl B1 (B1), and NaCl B2 (B2) are labeled. **(upper)** Pattern obtained at 27 GPa at room temperature after laser heating. The cobalt oxide peaks show significant strain anisotropy. **(lower)** Pattern obtained at 30 GPa and ~2400 K. Strain anisotropy is not observed during heating.



**Figure 2.** Measured cobalt oxide unit cell volume as a function of pressure and (binned) temperature. Data using the NaCl B1 pressure calibrant (circles), NaCl B2 pressure calibrant (squares) and ambient pressure thermal expansion data from Touzelin 1978 (diamonds) are plotted. Uncertainties are within the size of the symbols. Isotherms constructed from the best-fit thermoelastic properties and at the lower bound of each temperature bin are drawn.

**Figure 3.** The oxygen fugacity (left axis), Gibbs free energy in kJ/mol (interior right axis), and standard reduction potential in volts (exterior right axis) of the Co/CoO, Ni/NiO, and Fe/FeO metal/oxide systems. The equilibria are calculated as a function of pressure along an adiabat with a foot temperature of ~1600 K (Katsura et al. 2010).

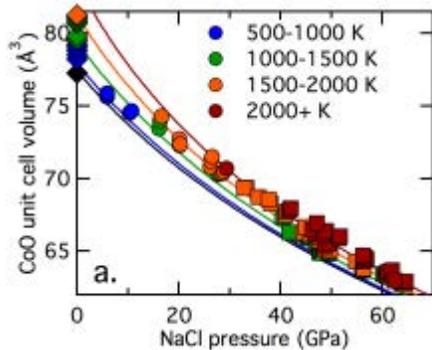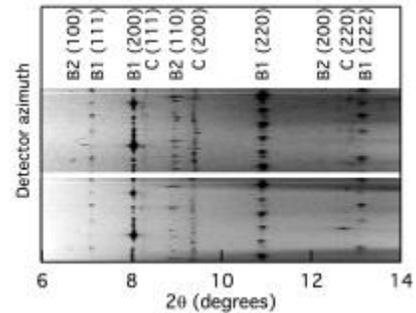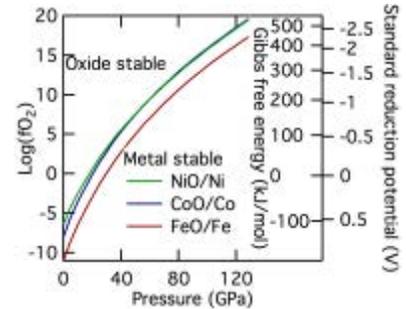References: M. M. Armentrout, E.S.G. Rainey and A. Kavner, (2013), High pressure and temperature equation of state of cobalt oxide: Implications for redox relations in Earth's mantle, *Am. Mineral.,* **98**, pp. 993-999.

# Oxidation-Reduction Reactions Occurring at the
# Slab-Mantle Interface in Subduction Zones

M. Guild[1], C. Till[1], E.E. Alp[2], W. Bi[2]

[1] *School of Earth and Space Exploration at Arizona State University, Tempe, AZ*
[2] *Advanced Photon Source, Argonne National Laboratory, Argonne, IL*

(COMPRES-related facilities:  Conventional Mössbauer Spectroscopy)

At subduction zones, oxidized material (i.e. oceanic crust and sediment) is introduced into relatively reduced material (i.e. the mantle) but we do not understand the specific oxidation-reduction reactions that occur at this interface.  Arc magmas are among the most oxidized igneous rocks on Earth, a signature which may be the result of the oxidation state of their mantle source produced by subduction zone fluids and melts (e.g., Gill, 1981; Carmichael, 1991; Kelley and Cottrell, 2009) or from secondary processing after leaving their mantle source, such as metasomatism, assimilation, fractional crystallization, melt-rock reaction, or degassing processes (e.g., Dauphas et al., 2009; Mallmann and O'Neill, 2009; Lee et al., 2005, 2010).

The Higashi-Akaishi peridotite body within the Sanbagawa metamorphic belt in SW Japan is interpreted to be an exhumed portion of mantle wedge.  Mantle wedge samples, as well as hydrous mantle wedge melts, are preserved in the Higashi-Akaishi body providing an opportunity to study oxidation state of natural mantle wedge samples.  Observations of the oxidation state of samples from the Higashi-Akaishi will test these two conflicting hypotheses and provide direct evidence of whether or not subduction processes oxidize the mantle.

Garnet pyroxenite samples were collected from the Higashi-Akaishi peridotite, are thought to represent trapped mantle wedge melts. Mineral separates of garnet, clinopyroxene, and orthopyroxene were sent to Argonne National Laboratory, where E.E. Alp and W. Bi performed conventional Mössbauer experiments in December 2015 to measure $Fe^{3+}/Fe^T$ as a preliminary test for potential future investigation.  Garnet showed a strong signal for $Fe^{2+}$ (close 100%). The spectra for 20 mg of orthopyroxene (12 wt% $FeO_t$) and 2 g of clinopyroxene (4 wt% $FeO_t$) were less definitive, but are interpreted to be dominantly $Fe^{2+}$.  Orthopyroxene may show some small percentage $Fe^{3+}$ however; an exact percentage of $Fe^{3+}$ and $Fe^{2+}$ have yet to be quantitatively determined.  Future planned analyses will measure $Fe^{3+}/Fe^T$ for higher purity and larger quantity mineral separates for the garnet pyroxenite as well as determine $Fe^{3+}/Fe^T$ for the other main units from the Higashi-Akaishi peridotite.

*Reference: Guild, M., Till, C., Alp, E.E., Bi, W., "What oxidation-reduction reactions are occurring at the slab-mantle interface?" FESD Dynamics of Earth System Oxygenation All-Hands Workshop, February 2016*
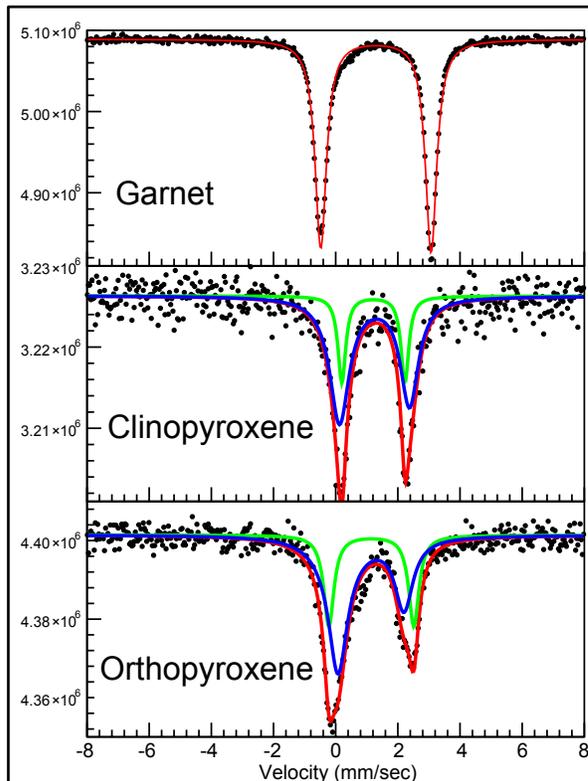


**Figure 1:  Conventional Mössbauer spectra of Fe-bearing minerals from the garnet pyroxenite of the Higashi-Akaishi peridotite body.**

# Redox-induced density contrast and implications for mantle structure and primitive oxygen

Tingting Gu[1], Mingming Li[2], Catherine McCammon[3] and Kanani K. M. Lee[1]
[1]Department of Geology & Geophysics, Yale University, New Haven, CT, 06511, USA
[2]School of Earth and Space Exploration, Arizona State University, Tempe, AZ, 85287, USA
[3]Bayerisches Geoinstitut, Universität Bayreuth, Bayreuth, 95440, Germany

(COMPRES-related facilities: COMPRES gas-loading system at GSECARS)

The high-pressure equations of state of the thermodynamically stable lower mantle phases in enstatite chondritic model mantle samples were collected using synchrotron x-ray diffraction in conjunction with the laser heated diamond anvil cell at GSECARS and HPCAT, sectors 13 and 16, APS (Figure 1). The two glass samples, one *oxidized* and one *reduced*, were nearly identical in their starting compositions, however differed in their $Fe^{3+}/Fe$ ratios. This slight difference in ferric iron causes the exsolution of alumina $Al_2O_3$ from the starting silicate sample, thereby decreasing the amount of Al in the dominant bridgmanite (Bm) phase, nominally $(Mg, Fe, Al, Si)O_3$. Overall, despite beginning with the same molar mass, the reduced sample is denser than the oxidized sample by 1-1.5%. Our geodynamic simulations suggest that such a density difference can cause a rapid ascent and accumulation of oxidized material in the upper mantle, with descent of the denser reduced material to the core-mantle boundary (Figure 2). The model leads to heterogeneous redox conditions in Earth's interior, which has profound implications for interpreting large low-shear velocity provinces and the rise of oxygen in Earth's atmosphere.
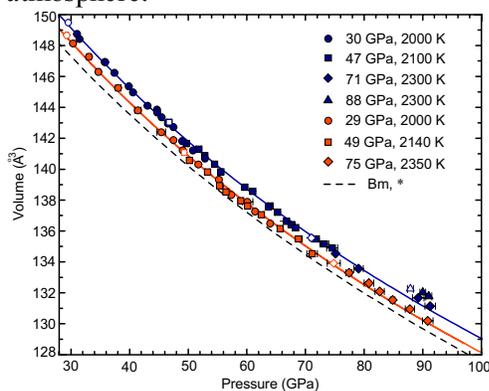


**Figure 1. Pressure versus volume of bridgmanite at room temperature, with corresponding B-M EOS curves.** J95_RED (dark blue) and J95_OX (light orange) samples are shown with PNe/Ar for all the data. Open symbols indicate pressures where the Bm was synthesized at, followed by solid symbols. Black dashed curve shown for pure end member $MgSiO_3$ Bm.



**Figure 2. Process of segregation between reduced and oxidized material caused by intrinsic density differences. a-d,** composition field in chronological order. Red and blue parts represent reduced and oxidized compositions with ~1.5-2% density difference, while the black part represents the upper mantle with constant density with the same value as the initial one of the more oxidized material. The color bar represents an intrinsic density difference of 0-2% corresponding to buoyancy number B between 0 and 0.8.
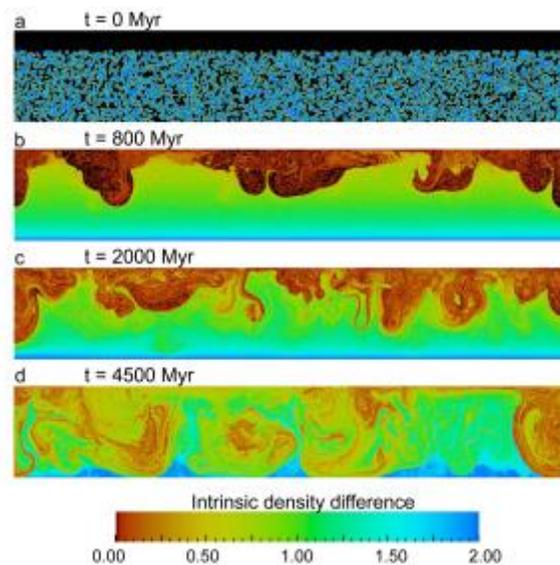
Reference: T. Gu, M. Li, C. McCammon and K. K. M. Lee, "Redox-induced density contrast and implications for mantle structure and primitive oxygen," *Nature Geoscience, in press* (2016).

# Lattice Dynamic Behavior of Orthoferrosilite (FeSiO3) toward Phase Transition under Compression

Jennifer Kung (NCKU, Taiwan) and Baosheng Li (Mineral Physics Institute, Stony Brook University, U.S.A)

(COMPRES-related facilities: National Synchrotron Light Source beamline X17B2)

We performed elasticity and Raman scattering measurements of ortho-FeSiO3 up to ~7.5 GPa. The velocities of the P and S waves were measured in conjunction with in situ X-radiation techniques. Above 5 GPa, the velocity of the S wave, but not the P wave, exhibited strong softening while the averaged crystal structure, as indicated by X-ray diffraction, maintained an orthorhombic symmetry. Within the same pressure range, the Raman shifts showed systematic increasing as a function of pressure. Based on the results of both Mg and Fe end-member orthopyroxenes, the observed velocity anomalies marked the onset of a phase transition to the high-pressure phase. The experimental results in this study provide insight into lattice dynamic behavior in terms of the composition effect at the onset of the phase transition in the orthopyroxene group under compression.
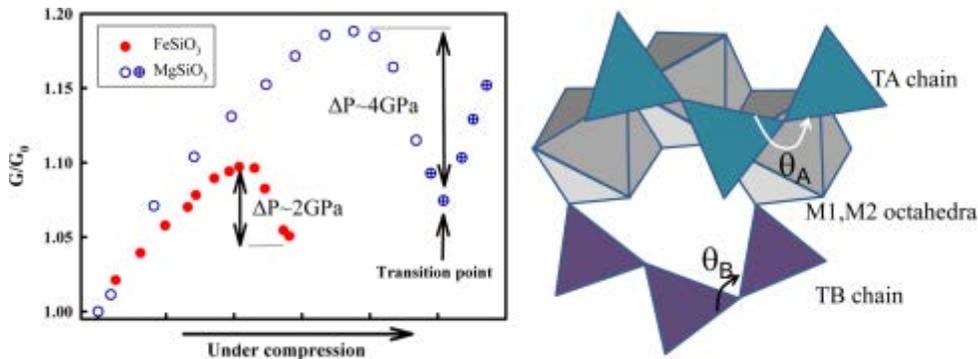


**Fig. 1.** Left:Comparison of the normalized shear modulus between of MgSiO3 and FeSiO3 orthopyroxenes. Right: Illustration of a part of the crystal structure of orthopyroxene, showing two different kink angles of the tetrahedral chains, θA (O3A−O3A−O3A) and θB (O3B−O3B−O3B).

**Reference**

Kung, J., and B. Li (2014), Lattice Dynamic Behavior of Orthoferrosilite (FeSiO$_3$) toward Phase Transition under Compression, J. Phys. Chem. C, 118 (23), 12410−12419, 2014.

# Excess volume and exsolution in pyrope-grossular garnets

There are very large systematic differences in quenched excess volumes in the pyrope-grossular garnets prepared in piston/cylinder (PC) or multianvil (MA) devices. The systematics of our quenched excess volumes from MA (dry) are much more positive and better behaved than in literature PC syntheses done with hydrothermal assistance. Large positive excess volumes were then measured on ALS beamline 12.2.2 at T to 600 °C and P to 10 GPa. The variation of thermal expansion and compressibility with composition is complex but systematic. Microstrains as a function of composition are also complex but anticorrelate with the same systematics.
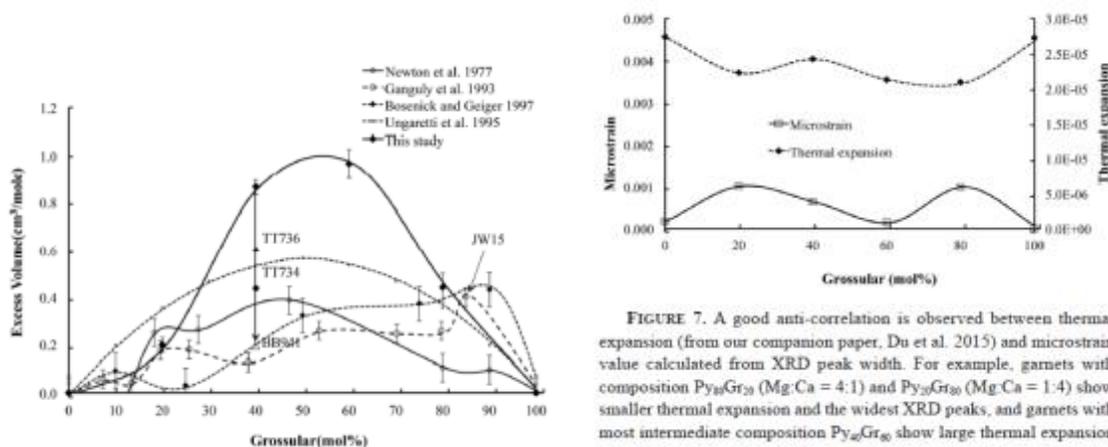


FIGURE 7. A good anti-correlation is observed between thermal expansion (from our companion paper, Du et al. 2015) and microstrain value calculated from XRD peak width. For example, garnets with composition $Py_{80}Gr_{20}$ (Mg:Ca = 4:1) and $Py_{20}Gr_{80}$ (Mg:Ca = 1:4) show smaller thermal expansion and the widest XRD peaks, and garnets with most intermediate composition $Py_{40}Gr_{60}$ show large thermal expansion but small microstrain value.

The persistence of the large positive excess volumes at P-T suggested that immiscibility should be observable in this system in the laboratory. **Both convergent and divergent garnet pairs at Gr 14 and Gr 36 have been established at 1200 °C/8 GPa, confirming this proposition and constraining garnet mixing properties better than from H, S, and V measurements.** This formed the basis of Wei Du's PhD thesis (2011) at Columbia University.

Publications from this project:

W Du, SM Clark, and D Walker (2015) Thermo-compression of pyrope-grossular garnet solid solutions: Non-linear compositional dependence. *American Mineralogist, Volume 100, pages 215–222.* doi.org/10.2138/am-2015-4752

W Du, SM Clark, and D Walker (2016) Excess mixing volume, microstrain, and stability of pyrope-grossular garnets. *American Mineralogist, Volume 101, pages 193–204.* doi.org/10.2138/am-2016-5128

# A new high-pressure phase transition in natural Fe-bearing orthoenstatite

Jin S. Zhang[1], Przemyslaw Dera[2] and Jay D. Bass[1]

[1] Department of Geology, University of Illinois, Urbana, Illinois 61801, U.S.A.
[2] Center for Advanced Radiation Sources, University of Chicago, Argonne National Laboratory, Argonne, Illinois 60439, U.S.A.

(COMPRES-related facilities: COMPRES gas-loading system at GSECARS)

Single-crystal X-ray structure refinements have been carried out on natural Fe-bearing orthoenstatite (OEN) at pressures up to 14.53 GPa. We report a new high-pressure phase transition from OEN to a monoclinic phase (HPCEN2) with space group $P2_1/c$, with a density change of ~1.9(3)%. The HPCEN2 phase is crystallographically different from low-pressure clinoenstatite (LPCEN), which also has $P2_1/c$ symmetry. Upon release of pressure HPCEN2 reverts to OEN, and the transition pressure is bracketed between 9.96 and 14.26 GPa at room temperature. We find no evidence for a $C2/c$ phase at high pressure. The lattice constants for the new phase at 14.26 GPa are $a$=17.87(2) Å, $b$=8.526(9) Å, $c$=4.9485(10) Å, $\beta$=92.88(4) ° ($\rho$=3.658(9) g/cm$^3$). Refinement of the new structure indicates rotation of tetrahedral chain as the key characteristic of this transition. This experiment points to the possibility of OEN and HPCEN2 as the stable phases in Earth's upper mantle.

OEN (Pbca) 12.66 GPa     HPCEN2 (P2₁/c) 14.26 GPa
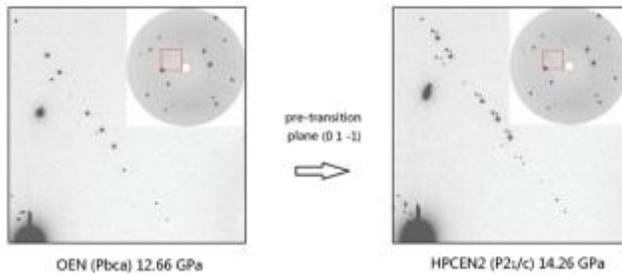
**Figure 1.** Comparison of single-crystal diffraction patterns before and after the OEN-HPCEN2 transition.

**Figure 2.** Polyhedral illustration of the structural change from OEN (Pbca) to HPCEN2 ($P2_1/c$). The O3-O3-O3 angle of the Pbca structure $\theta_A$=160.71(16)° (layer 1) changed to and $\theta_{A1}$= 148.44(79)° and $\theta_{A2}$= 216.61(77)°; in layer 2, $\theta_B$=135.44(15)° changed to $\theta_{B1}$=131.94(72)° and $\theta_{B2}$=133.13(49)°
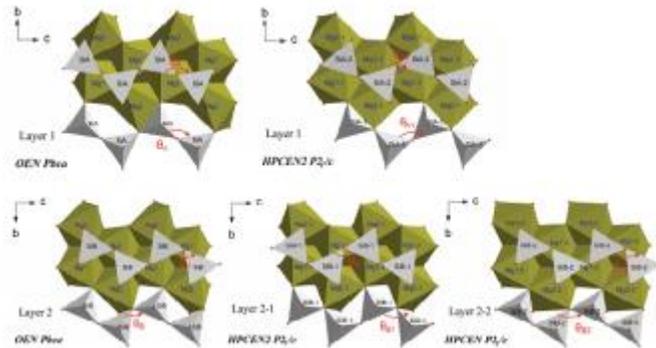
Reference: Zhang, J. S., P. Dera, and J. D. Bass (2012), A new high-pressure phase transition in natural Fe-bearing orthoenstatite, *Am. Mineral.* **97**, 1070–1074. doi:10.2138/am.2012.4072

# Effects of composition on the pressure-induced Pbca-P2₁/c phase transition of natural orthoenstatite

Jin S. Zhang[1,*], Bruno Reynard[2], Gilles Montagnac[2], Ru Cheng Wang[3] and Jay D. Bass[1]

[1] Department of Geology, University of Illinois, Urbana, Illinois 61801, U.S.A.

[2] Laboratoire de Géologie de Lyon, CNRS, Ecole Normale Supérieure de Lyon, France

[3] State Key Laboratory for Mineral Deposits Research, Department of Earth Sciences, Nanjing University, Nanjing 210093, China

Raman spectroscopy has been employed to investigate possible compositional effects on the high-pressure phase transition of Mg-rich orthoenstatite to a newly-discovered P2₁/c phase. Three natural orthoenstatite samples were used in this study: near end-member Mg orthoenstatite (Zabargad Island, Egypt), Al-free Fe-bearing orthoenstatite (Morogoro, Tanzania), and Al-rich Fe,Ca-bearing orthoenstatite (Kilbourne Hole, New Mexico). Experiments were carried out at room temperature. For all samples, the high-pressure phase transition is characterized by a splitting of the 660-680 cm$^{-1}$ doublet in the Raman spectrum into a triplet, with a corresponding change of peak intensities. These spectral changes are caused by the lowered symmetry of the high-pressure phase, as indicated by structural refinement from single-crystal X-ray diffraction results. The high-pressure phase of all samples appears to have space group P2₁/c. No evidence for a C2/c phase was observed. Our results indicate that upon compression, 10mol% Fe decreases the onset pressure of formation of the high-pressure P2₁/c phase by about 1 GPa. Results for the Kilbourne Hole OEN show that a combined enrichment of Al and Ca contents increases the onset pressure of formation of HPCEN2 (upon compression) by over 3 GPa relative to Tanzania OEN. Upon decompression, all samples revert to single-crystals of the orthoenstatite starting phase.
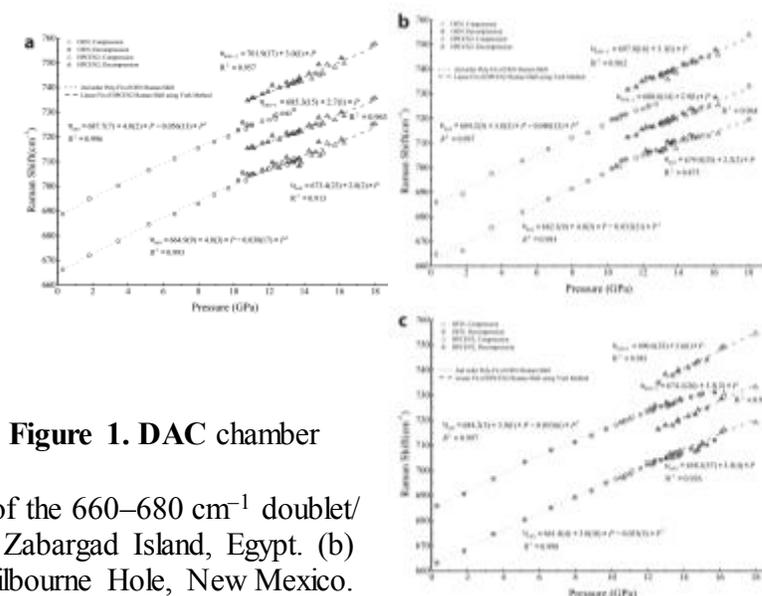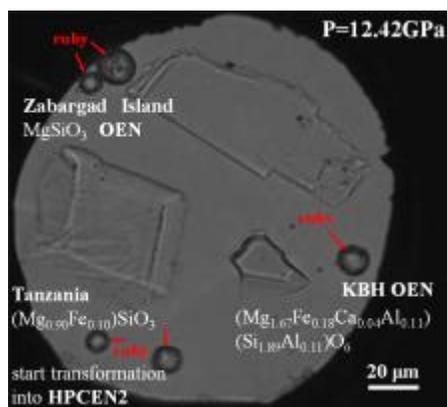
**Figure 1. DAC** chamber



**Figure 2.** Raman frequency shifts of the 660–680 cm$^{-1}$ doublet/triplet as a function of pressure. (a) Zabargad Island, Egypt. (b) Morogoro Region, Tanzania. (c) Kilbourne Hole, New Mexico.

Reference: Zhang, J. S., Reynard, B., Montagnac, G., Wang, R. and J. D. Bass (2013), Pressure-induced Pbca-P2₁/c phase transition of natural orthoenstatite: Compositional effect and its geophysical implications, *Am. Mineral.* **98**, 986-992. doi:10.2138/am.2013.4345

# Pressure-induced Pbca-P2$_1$/c phase transition of natural orthoenstatite: the effect of high temperature and its geophysical implications

Jin S. Zhang[1,*], Bruno Reynard[2], Gilles Montagnac[2], and Jay D. Bass[1]

[1] Department of Geology, University of Illinois, Urbana, Illinois 61801, U.S.A.
[2] Laboratoire de Géologie de Lyon UMR CNRS 5276 Ecole Normale Supérieure de Lyon, France

In-situ high-pressure (P) high-temperature (T) Raman spectroscopy has been used to investigate the effect of temperature on the high-pressure phase transition of Mg-rich orthoenstatite (OEN) to a newly-discovered P2$_1$/c phase (HPCEN2) up to 673K and 18.2(10) GPa. Two natural orthoenstatite samples were used in this study: near end-member Mg orthoenstatite (Zabargad Island, Egypt), and Al+Fe-bearing orthoenstatite (San Carlos, Arizona). For San Carlos OEN (SC-OEN), the experiment was performed at room temperature, 373K, 573K and 673K; For Zabargad Island OEN (Zabg OEN), experiments were performed at 573K and 673K. The three phases OEN, HPCEN2, and another high-pressure phase with space group C2/c (denoted by HPCEN) are readily distinguished by a characteristic doublet, triplet, or singlet, respectively, in the 660-680 cm$^{-1}$ range. Similarly, splitting of a peak near 1100 cm$^{-1}$ is indicative of an OEN→HPCEN2 transition. For both samples, no phase other than OEN and HPCEN2 was observed within the investigated P-T range. The recovered products after slow cooling for over 24 hours from 673K and 16.6(9) GPa were OEN. The Clapeyron slope (dP/dT) of this transition is bracketed between +0.020 to -0.0026 GPa/K for Zabg-OEN, and +0.0023 to -0.0049 GPa/K for SC-OEN. Our results suggest a possible stability field for HPCEN2 at the bottom of the upper mantle.

**Figure 1.** Raman spectra of OEN and HPCEN2 for Zabargad samples at high P and several temperatures. Blue arrows indicate the disappearance or strong intensity decay of the 403 cm$^{-1}$ peak in the HPCEN2 phase; red arrows indicate the appearance of a slightly higher frequency mode (468cm$^{-1}$ peak at 12GPa) associated with the OEN→HPCEN2 transition. Note that at P=11.0 GPa and 298K, the back transformation of to OEN has started, but is incomplete; both OEN and HPCEN2 are present at these conditions.

**Figure 2.** Clapeyron slope dP/dT for the Pbca → P2$_1$/c transition. The room-temperature compression data points are from Zhang et al. (2012; 2013).

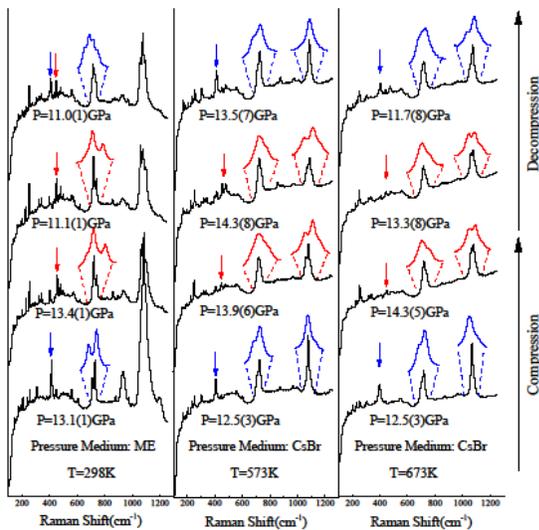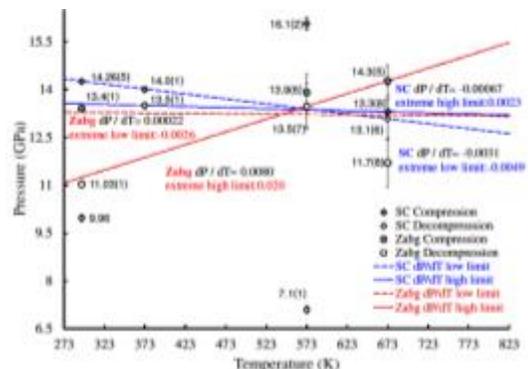Reference: Zhang, J. S., Reynard, B., Montagnac, G, and J. D.Bass (2014), Pressure-induced Pbca-P2$_1$/c phase transition of natural orthoenstatite: high temperature effect and its geophysical implications, *Phys.Earth Planet. Int.* **228**, 150-159. doi: 10.1016/j.pepi.2013.09.008

# The role of carbon in extrasolar planetary geodynamics and habitability

C.T. Unterborn, JE Kabbes, JS Pigott, DM Reaman, WR Panero, *The Astrophysical Journal* 793 (2): 124, 2014.

The proportions of oxygen, carbon, and major rock-forming elements (e.g., Mg, Fe, Si) determine a planet's dominant mineralogy. Variation in a planet's mineralogy subsequently affects planetary mantle dynamics as well as any deep water or carbon cycle. Through thermodynamic models and high-pressure diamond anvil cell experiments, we demonstrate that the oxidation potential of C is above that of Fe at all pressures and temperatures, indicative of 0.1-2 Earth-mass planets. This means that for a planet with (Mg+2Si+Fe+2C)/O > 1, excess C in the mantle will be in the form of diamond. We find that an increase in C, and thus diamond, concentration slows convection relative to a silicate-dominated planet, due to diamond's ~3 order of magnitude increase in both viscosity and thermal conductivity. We assert then that in the C-(Mg+2Si+Fe)-O system, there is a compositional range in which a planet can be habitable. Planets outside of this range will be dynamically sluggish or stagnant, thus having limited carbon or water cycles leading to surface conditions inhospitable to life as we know it.
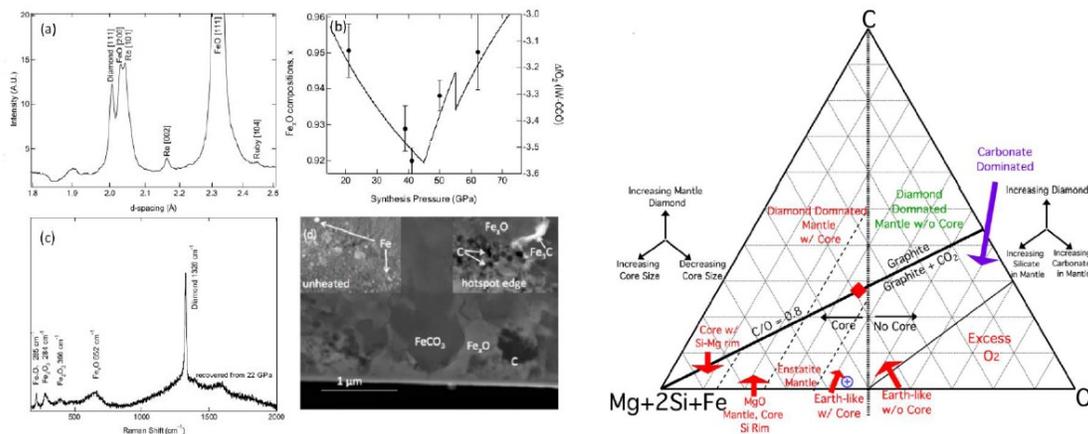


**Left**: Reactions between FeO, $FeCO_3$, and Fe at 21–63 GPa and 2150(150) K show the oxidation of iron and reduction of carbon. (a) X-ray diffraction at 43 GPa shows the presence of diamond and wüstite with no evident siderite. (b) The unit cell volume of the recovered sample. (c) Raman spectroscopy of a sample recovered from 22 GPa. (d) TEM image of a foil extracted by focused-ion beam milling from a sample recovered from 63 GPa and 2200 K. **Right**: Ternary diagram for the C–(Mg+2Si+Fe)–O system defining compositional regimes of interior planet compositions and structure.

## Constitutive Law and Flow Mechanism in Diamond Deformation

For centuries it has been known that diamond is brittle and can easily cleave when crafting on a certain crystallographic plane. However, as the hardest material known to mankind, diamond is experimentally difficult to deform, particularly at room temperature. The classic strain-stress relation, which is fundamentally important to the plasticity of diamond, has yet to be established under both room and elevated temperatures. We studied deformation behavior of polycrystalline diamond at room temperature, 1000°C, and 1200°C, near confined pressures of 3.5 GPa. The uniaxial high *P-T* deformation experiments were carried out in a deformation- DIA apparatus (D-DIA) interfaced with synchrotron x-ray diffraction and radiography at COMPRES-supported MAC facility (X17B2-NSLS/6BMB-APS). At any given deformation state, the macroscopic differential stress is derived from elastic distortion in a crystalline lattice and the total axial strain is measured by x-ray imaging of the bulk sample. We also derived the microscopic strain based on diffraction profile analysis. The deformation at room temperature is essentially brittle, cataclastic, and mostly accommodated by fracturing on {111} plane with no plastic yielding at uniaxial strains up to 15%. At elevated temperatures diamond crystals exhibit significant ductile flow with corresponding yield strength of 7.9 and 6.3 GPa, indicating that diamond starts to weaken when temperature is over 1000°C. At high temperatures the plastic deformation and ductile flow is meditated by the <110>{111} dislocation glide and the {111} micro-twinning.
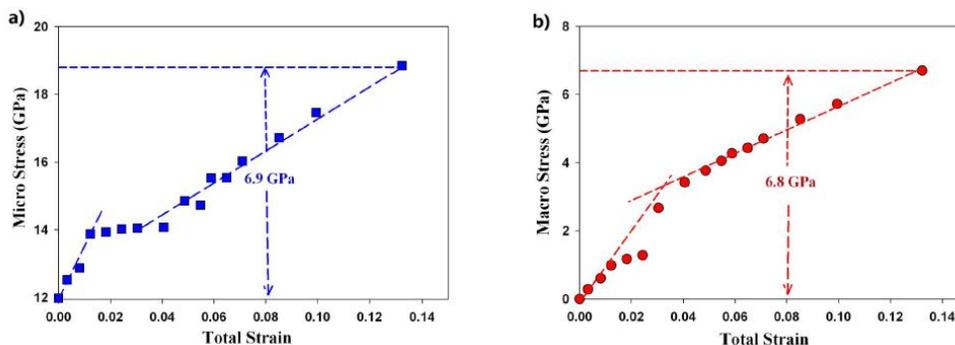


**Figure 1** (a) Microscopic and (b) macroscopic stress as a function of total strain for polycrystalline diamond deformed at room temperature and a confining pressure of 3.5 GPa.
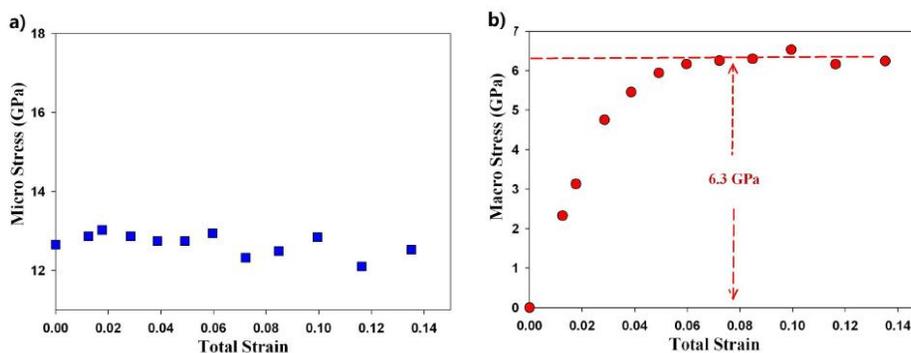


**Figure 2** (a) Microscopic strain-stress curve and (b) macroscopic strain-stress curve for polycrystalline diamond deformed at 1200°C and ~ 4.0 GPa. Because the deformation experiment was conducted at a higher temperature of 1200°C a higher pressure was applied to prevent potential graphitization of diamond.

**Slab stagnation in the shallow lower mantle linked to an increase in mantle viscosity.**
Hauke Marquardt and Lowell Miyagi, U. Bayreuth and U. Utah

(COMPRES-related facilities: ALS 12.2.2, ALS 12.2.2. Laser mill)

Seismic images appear to show that some subducting slabs of oceanic lithosphere stagnate and broaden in the mid-lower mantle. However, bridgmanite and ferropericlase, the main phases of the lower mantle do not show any structural transitions at this depth. Thus, one would one would not expect the presence of a mid-mantle boundary layer that would impede slab subduction. We performed angle-dispersive high-pressure radial x-ray diffraction (rXRD) on $(Mg_{0.8}Fe_{0.2})O$ and $(Mg_{0.9}Fe_{0.1})O$ powder at Beamline 12.2.2 of the Advanced Light Source, Lawrence Berkeley National Laboratory. Deformation of ferropericlase was accomplished in a panoramic diamond-anvil cell to a maximum pressure of 100 GPa using x-ray transparent cubic boron nitride (cBN) and beryllium gaskets. We observe an initial increase of all lattice strains, followed by saturation by 20 GPa. Starting from ~20-30 GPa we observe a pronounced increase of lattice strains corresponding to (111), (220) and (311) lattice planes. This secondary increase in lattice strains continues to ~65 GPa at which point the rate lattice strains again level off. Using elastic constants from Marquardt et al. (2009), we calculate that the flow strength of ferropericlase increases by a factor of three at pressures from 20 to 65 GPa (Figure 2, Marquardt and Miyagi 2015). Modeling based on this data shows that mantle viscosity near subducting slabs could increase by 2.3 orders of magnitude, which could lead to the stagnation of slabs in the mid lower mantle.

**Figure 2** of (Marquardt and Miyagi 2015): Strength of $(Mg0.8Fe0.2)O$ ferropericlase vs pressure. Red circles are measurements in Be-gasket while blue diamonds are measurements in cBN gaskets. Solid black lines, linear fits to data in the pressure ranges <20 GPa, 20–65 GPa and >65 GPa. Dashed black line, linear extrapolation of data at pressures <20 GPa. Black squares, $(Mg0.83Fe0.17)O$ (Lin et al., 2009; white triangles, $(Mg0.4Fe0.6)O$ (Tommaseo et al., 2006). White circles, blue dashed line, $(Mg0.8Fe0.2)O$ (Miyagi et al., 2013). Black circles, $(Mg0.9Fe0.1)SiO_3$ bridgmanite (Merkel et al., 2003).
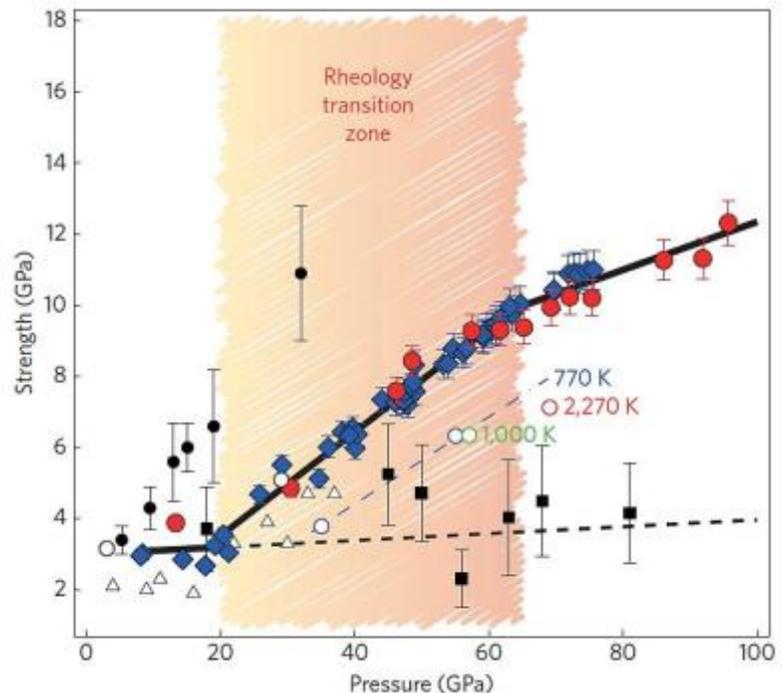


Reference: H. Marquardt, L. Miyagi (2015), Slab stagnation in the shallow lower mantle linked to an increase in mantle viscosity. Nature Geosci 8, 311–314.

# Texture development and slip systems in bridgmanite and bridgmanite + ferropericlase aggregates.

Lowell Miyagi and Hans-Rudolf Wenk, U. Utah, UCB

(COMPRES-related facilities: ALS 12.2.2)

Bridgmanite (Mg,Fe)SiO3 and ferropericlase (Mg,Fe)O are the most abundant phases in the lower mantle and localized regions of the D" layer just above the core mantle boundary. Seismic anisotropy is observed near subduction zones at the top of the lower mantle and in the D" region. One source of anisotropy is dislocation glide and associated texture (crystallographic preferred orientation) development. Thus, in order to interpret seismic anisotropy, it is important to understand texture development and slip system activities in bridgmanite and bridgmanite + ferropericlase aggregates. We studied on in-situ texture development in bridgmanite and bridgmanite + ferropericlase aggregates deformed in the diamond anvil cell up to 61 GPa. When bridgmanite is synthesized from enstatite it exhibits a strong (4.2 m.r.d.) 001 transformation texture due to a structural relationship with the precursor enstatite phase. When bridgmanite + ferropericlase are synthesized from olivine or ringwoodite, bridgmanite exhibits a relatively weak 100 transformation texture (1.2 and 1.6 m.r.d. respectively). This is likely due to minimization of elastic strain energy as a result of Young's modulus anisotropy. In bridgmanite 001 deformation textures are observed at pressures < 55 GPa. The 001 texture is likely due to slip on (001) planes in the [100], [010], and <110> directions. Stress relaxation by laser annealing to 1500-1600 K does not result in a change in this texture type. However at pressures > 55 GPa a change in texture to a 100 maximum is observed, consistent with slip on the (100) plane. Ferropericlase, when deformed with bridgmanite, does not develop a coherent texture. This is likely due to strain heterogeneity within the softer ferropericlase grains. Thus it is plausible that ferropericlase is not a significant source of anisotropy in the lower mantle.
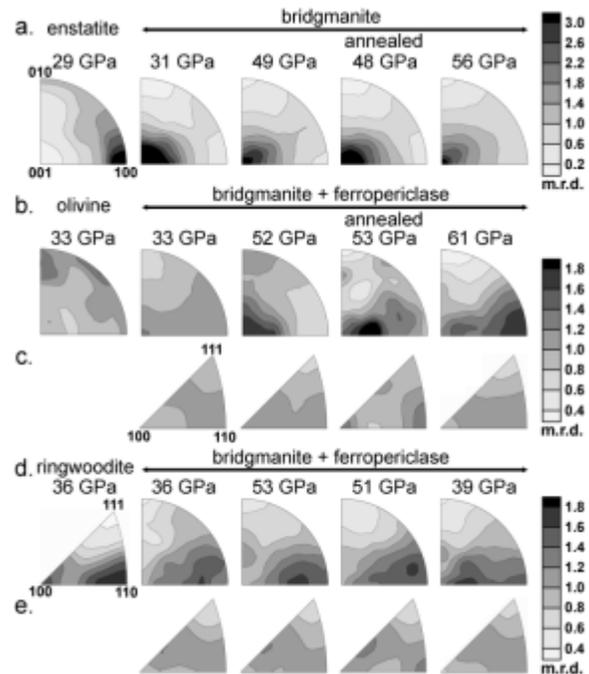


**Figure 3** of Miyagi and Wenk (2016): Inverse pole figures of starting materials and bridgmanite and ferropericlase for selected data points. Run1 is shown in part a, Run 2 is shown in part b (bridgmanite) and part c (ferropericlase). Run 3 is shown in part d (bridgmanite) and part e (ferropericlase). IPFs show the probability of finding the pole (normal) to a lattice plane in the compression direction.

Reference: L. Miyagi, and H.-R. Wenk (2016), Texture development and slip systems in bridgmanite and bridgmanite + ferropericlase aggregates, *Phys Chem Minerals*, 1–17.

# Plastic Anisotropy and Slip Systems in Ringwoodite Deformed to High Shear Strain in the Rotational Drickamer Apparatus

Lowell Miyagi, George Amulele, Kazuhiko Otsuka, Zhixue Du, Robert Farla, and Shun-Ichiro Karato, U. Utah, Yale University

(COMPRES-related facilities: NSLS X17B2)

High shear strain deformation experiments up to equivalent strains of 180% were performed on ringwoodite in the Rotational Drickamer Apparatus at pressures of 23 GPa and temperatures of 1800 K. At very large shear strains deviation in the strengths of the (311) and (400) lattice planes is observed, indicating plastic anisotropy. Lattice strain theory was applied to calculate effective viscosities for available slip systems from the observed plastic anisotropy. We find that the effective viscosities (unitless) are proportional to 0.43, 0.46, and 1.54 for the $\{111\}<1\bar{1}0>$, $\{1\bar{1}0\}<110>$ and $\{001\}<1\bar{1}0>$ slip systems respectively. This indicates that $\{111\}<1\bar{1}0>$ slip is slightly softer than $\{1\bar{1}0\}<110>$ at these conditions. However since the $\{111\}<1\bar{1}0>$ slip system has significantly more symmetric variants than the slip systems involving other lattice planes, it is expected to dominate deformation. This is confirmed by polycrystal plasticity modeling using the viscoplastic self-consistent code (VPSC) which indicates that simulations with dominant $\{111\}<1\bar{1}0>$ slip provides the best match to experimental textures.



**Figure 5** of Miyagi et al. (2014): Equivalent stress plotted versus equivalent strain for San_230 (solid symbols) and San_231 (open symbols). Equivalent stress calculated from the (311) ringwoodite peak is shown with square symbols and (400) is represented by diamond shaped symbols. The black arrow indicates when strain rate was stepped in San_230.



**Figure 6** of Miyagi et al. (2014): Equal area upper hemisphere pole figures for (100), (110), and (111) pole showing textures obtained for San_230. Texture strength is measured in m.r.d. Texture after annealing and prior to deformation is shown in (a). Figure (b) shows texture development at 23% equivalent strain, prior to strain rate stepping. Figure (c) show texture after deformation to 180% equivalent strain. Sense of shear for (b) and (c) is shown with black arrows.

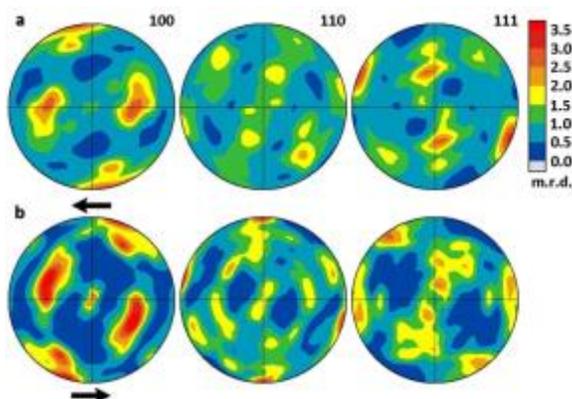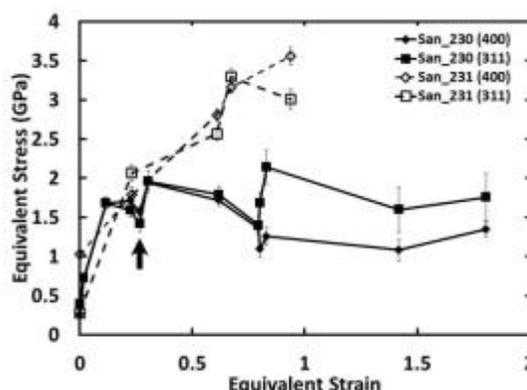Reference: L. Miyagi, G. Amulele, K. Otsuka, Z. Du, R. Farla, and S.-I. Karato (2014), Plastic anisotropy and slip systems in ringwoodite deformed to high shear strain in the Rotational Drickamer Apparatus, *Physics of the Earth and Planetary Interiors*, *228*, 244–253.

# Studies by the Yale program at NSLS (Karato)

We use RDA (rotational Drickamer apparatus) combined with the synchrotron x-ray facility at X17B2 at NSLS to study the plastic flow behavior of materials under high-pressure and temperature conditions. We have conducted quantitative deformation experiments on two important minerals in Earth's transition zone (410 to 660 km depth). The flow laws (stress-strain rate relationship) of these minerals were investigated using the *in-situ* X-ray diffraction and x-ray radiography. These studies have provided constraints on the resistance of these minerals for plastic flow under a broad range of conditions.

In addition, we have pushed the pressure limit of quantitative studies on plastic flow in order to understand the plastic properties of minerals in the lower mantle (660-2890 km). This is the largest portion of the rocky part of this planet. By analyzing the diffracted x-ray from various portions of the sample, we realized that a substantial pressure gradient is present in the sample assembly of RDA. Consequently, we reduced the sample size to conduct deformation experiments at pressures of ~27 GPa and temperature of ~2100 K (both P and T were determined by the equations of state of two materials). Under these conditions, dominant minerals are $(Mg,Fe)SiO_3$ bridgmanite and $(Mg,Fe)O$. We found that bridgmanite has substantially higher resistance to deformation than $(Mg,Fe)O$.
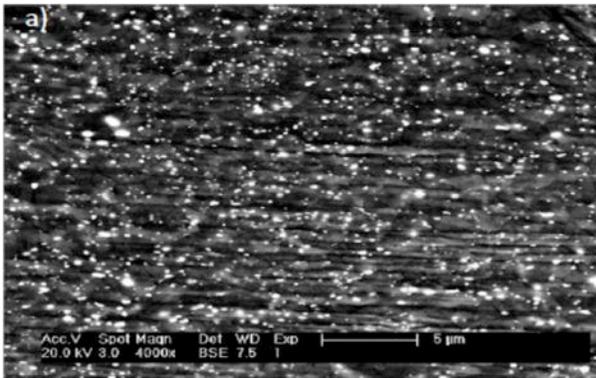


SEM micrograph of a deformed bridgmanite + (Mg,Fe)O aggregate. Dark regions are bridgmanite and light grey regions are (Mg,Fe)O. Bright spots are metallic Fe.

Conditions of deformation are P=27 GPa, T=2130 K, strain-rate $\sim 10^{-5}$ s$^{-1}$.

# Grain-boundary Plasticity in Olivine (P. Raterron, C. Bollinger*, N. Hilairet, S. Merkel)

The rheology of the Earth upper mantle is controlled by the plasticity of olivine-rich rocks. Olivine single crystal plasticity is understood and quantified to mantle pressures and temperatures (e.g., Bai et al., 1991, JGR, 96, 2441-2463; Raterron et al., 2012, PEPI, 200-201, 105-112). The plasticity of aggregates involves complex mechanisms, and the fundamental question of the amount of strain accommodated at grain boundaries remains unanswered.

Using reported experimental data on San Carlos olivine deformation at mantle conditions - mostly obtained in the D-DIA that equipped the NSLS X17B2 beamline (e.g., Durham et al., 2009, PEPI, 172, 67-73; Bollinger et al., 2014, PEPI, 228, 211-219) - we compared the plasticity of olivine aggregates to that of single crystals and demonstrated that strain at grain boundaries can be orders of magnitude larger than intracrystalline strain. We further showed that the proportion of grain-boundary strain decreases with increasing temperature and stress. Applied along mantle geotherms (Figure), our results shows that grain boundary plasticity is dominant in the shallow mantle. In the deep upper mantle, grain boundary plasticity vanishes and strain is accommodated within the grains.
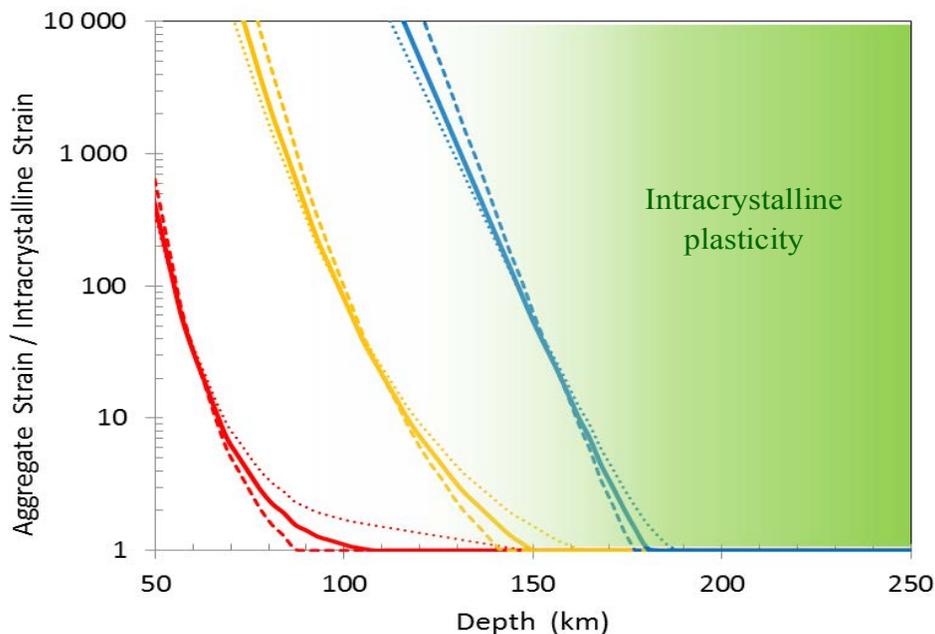


**Figure: Aggregate strain / Intracrystalline strain in olivine versus depth, along a 20-Ma (red) and an 80-Ma (yellow) ocean geotherm, and a continental geotherm (blue). The lines correspond to different oxygen fugacities (dotted IW, plain FQM-2, dashed FQM).**

# High-Energy X-ray Focusing and High-pressure Pair Distribution Function Research

Xinguo Hong[1], Thomas S. Duffy[2], Lars Ehm[1,3], Zhong Zhong[3], Sanjit Ghose[3], and Donald J. Weidner[1]

[1]*Mineral Physics Institute, Stony Brook University, Stony Brook, NY 11794, USA*
[2]*Department of Geosciences, Princeton University, Princeton, NJ 08544, USA*
[3]*National Synchrotron Light Source II, Brookhaven National Laboratory, Upton, NY 11973, USA*

The atomic pair distribution function (PDF) method using short-wavelength, high energy X-ray or neutron diffraction is a powerful tool for studying crystalline, disordered, and nanocrytalline materials. However, as the refractive index of most materials is close to unity in the X-ray range, focusing high-energy X-rays is challenging, leading to sparse studies of high-pressure pair distribution function (HP-PDF) reported so far. We have developed a micro-focusing optics for high-energy x-rays by combining a sagittally bent Laue crystal monchromator with Kirkpatrick-Baez (K–B) X-ray focusing mirrors. The optical system is able to provide a clean, high-flux X-ray beam suitable for pair distribution function (PDF) measurements at high pressure using a diamond anvil cell (DAC). The coupling of sagittally bent Laue crystals with K–B mirrors provides a useful means to focus high-energy synchrotron X-rays from a bending magnet or wiggler source. A focused beam of moderate size (10–15 μm) has been achieved at energies of 66 and 81 keV. PDF data for nanocrystalline platinum (n-Pt) were collected at 12.5 GPa with a single 5 s X-ray exposure, showing that the in-situ compression, decompression, and relaxation behavior of samples in the DAC can be investigated with this technique. PDFs of nano Pt (n-Pt) and nano Au (n-Au) under quasi-hydrostatic loading to as high as 71 GPa indicate the existence of substantial reduction of grain or domain size for Pt and Au nanoparticles at pressures below 10 GPa. As shown by the HP-PDF examples of Pt and Au nanoparticles and $GeO_2$ glass, the obtained micro-focusing high-energy X-rays should be applicable to a wide range of science including fundamental materials physics, geology, high-pressure research, and energy-materials research.
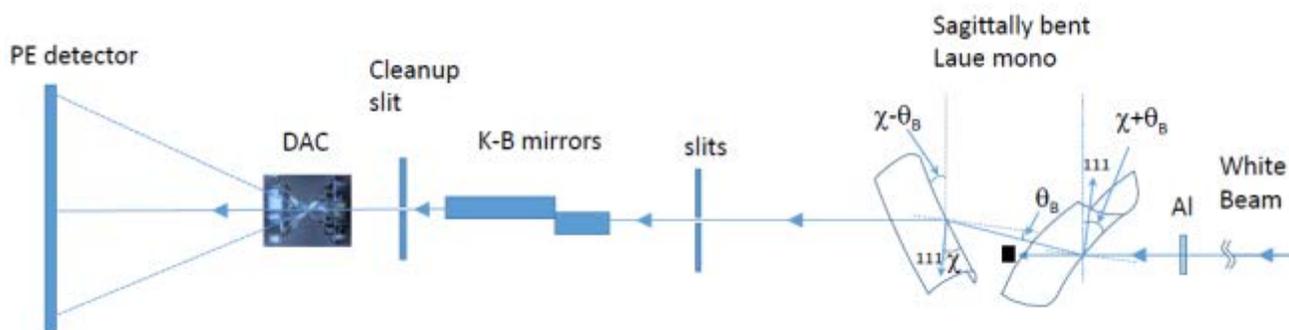
Schematic layout of high-energy X-ray focusing optics combining a sagittally bent Laue monochromator with K–B mirrors. The components from right to left (direction of X-ray propagation) are: aluminum (Al) filter, sagittally bent Laue crystals in anti-clastic bending geometry, slits, K–B mirrors, clean-up slits, DAC stage, and Perkin-Elmer (PE) detector.

## References

Hong, X., L. Ehm, Z. Zhong, S. Ghose, T. S. Duffy and D. J. Weidner, High-energy X-ray focusing and applications to pair distribution function investigation of Pt and Au nanoparticles at high pressures, *Scientific Reports* 6: 21434, 2016.

# Measurement setup for the simultaneous determination of diffusivity and Seebeck coefficient in a multi-anvil apparatus

Matthew K. Jacobsen, Wei Liu and Baosheng Li (Mineral Physics Institute, Stony Brook University, U.S.A)

(COMPRES-related facilities: Multi-anvil Cell Assembly Facility)

In this paper, a high pressure setup is presented for performing simultaneous measurements of Seebeck coefficient and thermal diffusivity in multi-anvil apparatus for the purpose of enhancing the study of transport phenomena. Procedures for the derivation of Seebeck coefficient and thermal diffusivity/conductivity, as well as their associated sources of errors, are presented in detail, using results obtained on the filled skutterudite, $Ce_{0.8}Fe_3CoSb_{12}$, up to 12 GPa at ambient temperature. The polycrystalline specimen was synthesized at high pressure and high temperature in a 1000-ton multi-anvil apparatus. Together with recent resistivity and sound velocity measurements in the same apparatus, these developments not only provide the necessary data for a self-consistent and complete characterization of the figure of merit of thermoelectric materials under pressure, but also serve as an important tool for furthering our knowledge of the dynamics and interplay between these transport phenomena.
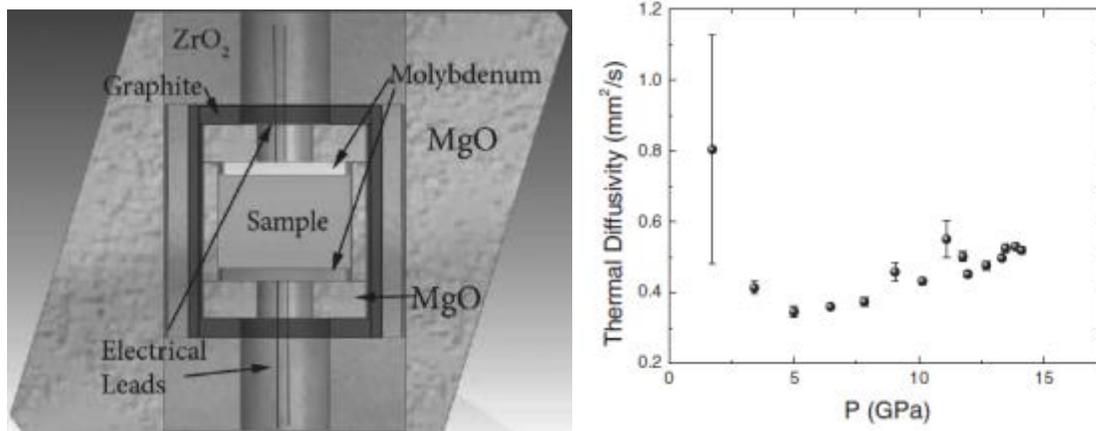


**Fig. 1** Multi-anvil thermal diffusivity/Seebeck coefficient cell assembly (left) and the thermal diffusivity vs. pressure for $Ce_{0.8}Fe_3CoSb_{12}$.

### Reference

Jacobsen, M., W. Liu, and B. Li, Measurement Setup for the Simultaneous Determination of Diffusivity and Seebeck coefficient in a Multi-Anvil Apparatus, Rev. Sci. Instrum. 83, 093903 (2012).

# Absolute X-Ray Energy Calibration Using a Diffraction-based Iterative Method

Xinguo Hong[1], Zhiqiang Chen[1] and Thomas S. Duffy[2]

[1]*Mineral Physics Institute, Stony Brook University, Stony Brook, New York 11794, USA*
[2]*Department of Geosciences, Princeton University, Princeton, New Jersey 08544, USA*

Accurate X-ray energy calibration is indispensable for X-ray energy-sensitive scattering and diffraction experiments, but there is still a lack of effective methods to precisely calibrate X-ray energy over a wide range. In this paper, the authors proposed a new method of precise and fast absolute X-ray energy calibration over a wide energy range using an iterative X-ray diffraction based method. It is found that by using an iterative algorithm the X-ray energy is only tied to the relative offset of sample-to-detector distance, which can be readily varied with high precision on the order of $10^{-5}$–$10^{-6}$ spatial resolution using gauge blocks. Even starting with arbitrary initial values of 0.1Å, 0.3Å, and 0.4 Å, the iteration process converges to a value within 3.5 eV for 31.122 keV X-rays after three iterations. Different diffraction standards of $CeO_2$, Au and Si show an energy deviation of 14eV. As an application, the proposed method has been applied to determine the pair distribution function (PDF) measurement using calibrated high-energy X-rays at 82.273 keV. Unlike the traditional X-ray absorption-based calibration method, the proposed approach doesn't rely on any edges of specific elements, and is applicable to the high energy X-ray region where no appropriate absorption edge is readily available.
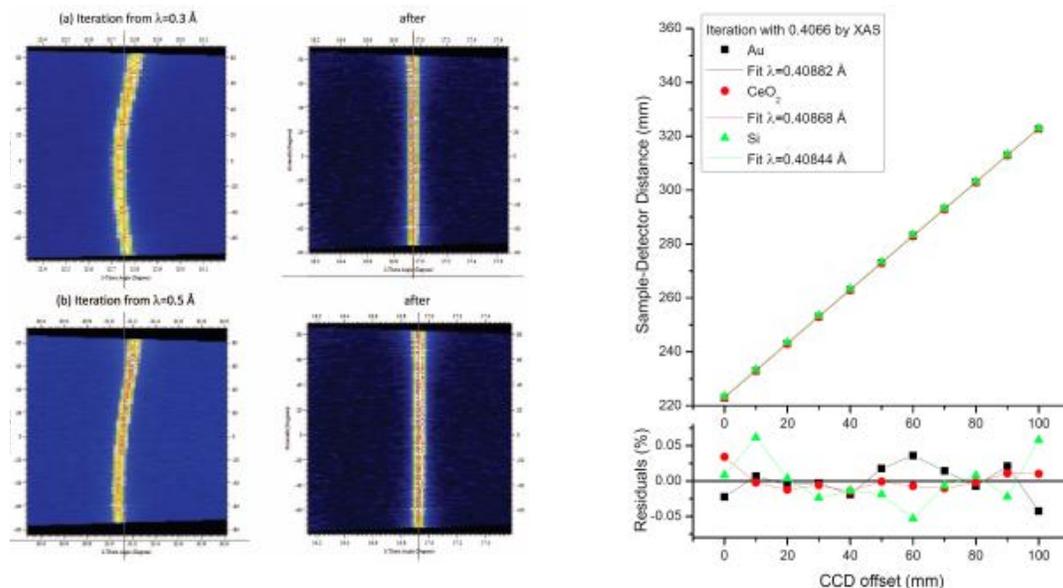
**Left:** Effect of iteration process on FIT2D function magnified for the line at $2\theta = 17°$ with initial x-ray wavelength 0.3 Å and 0.5 Å, respectively. **Right:** Energy calibration with different diffraction standards, Au, CeO2, and Si, using the initial value of 0.4066 Å defined by x-ray absorption. After iteration for three times, the standard deviation among these standards becomes $1.9 \times 10^{-4}$. (Upper panel) linear correlation of apparent sample-to-detector distance with real CCD offset; (lower panel) Residuum of linear fitting at each iteration step in percent.

**Reference:** Hong, X., Z. Chen and T. S. Duffy, Absolute x-ray energy calibration over a wide energy range using a diffraction-based iterative method, *Review of Scientific Instruments,* **83**: 063901, 2012.

# The influence of wavelength-dependent absorption and temperature gradients on temperature determination in laser-heated diamond-anvil cells

Jie Deng[1], Zhixue Du[1,2], Kanani K. M. Lee[1]

[1]Department of Geology & Geophysics, Yale University, New Haven, CT
[2]Geophysical Laboratory, Carnegie Institution of Washington, Washington DC

(COMPRES-related facilities: offline IR at NSLS II)

*In situ* temperature measurements in laser-heated diamond-anvil cell (LHDAC) experiments are among the most fundamental measurements undertaken in high-pressure science. Despite its importance, few efforts have been made to examine the alteration of thermal radiation spectra of hot samples by wavelength-dependent absorption of the sample itself and temperature gradients within samples while laser heating and their influence on temperature determination. In this study, we take (Mg, Fe)O ferropericlase as an example to evaluate the effects of these two factors. Iron-rich ferropericlase shows strong wavelength dependent absorption in the wavelength range used to determine temperature (Figure 1), which, together with temperature gradients can account for largely deviated apparent temperatures (e.g., 1200 K deviation for a 4000 K melting temperature) in some experiments obtained by Wien fitting of thermal radiation intensities detected. In general, wavelength-dependent absorption and temperature gradients of samples are two key factors to consider in order to obtain rigorously constrained temperatures, which have been largely ignored in previous LHDAC studies.
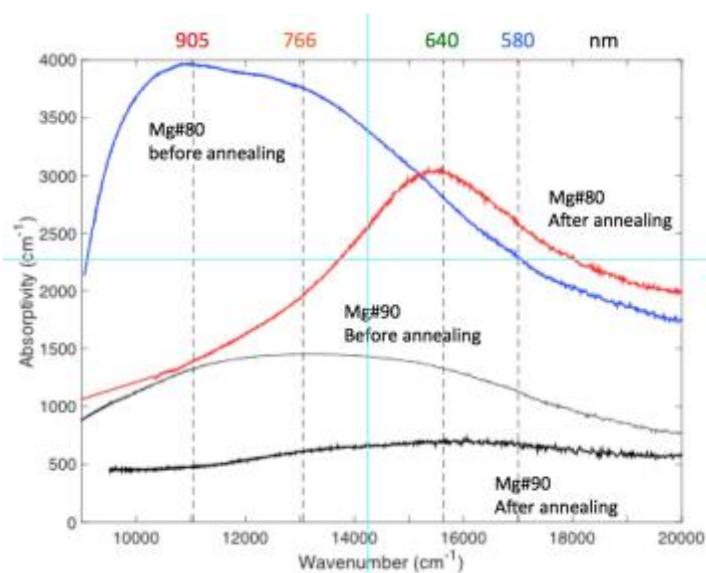


**Figure 1.** Absorption spectra for polycrystalline (Mg,Fe)O with varying composition at 40 (gray, black) and 50 GPa (blue, red), before and after annealing.

# The Compact Dynamic Beamstop: Real-time Beam Diagnostics with Minimal Angular Obstruction

Diane Bryant & Simon Morton, Berkeley Center for Structural Biology, LBNL

COMPRES-related facility: Laser Miller at the Advanced Light Source



*Figure 1- This is a close up of a recent CDBS prototype, shown next to the tip of a ball point pen for scale.*

All crystallography beamlines at all synchrotrons in the world require a beamstop. This is necessary to prevent high-intensity x-rays from damaging the sensitive x-ray detectors install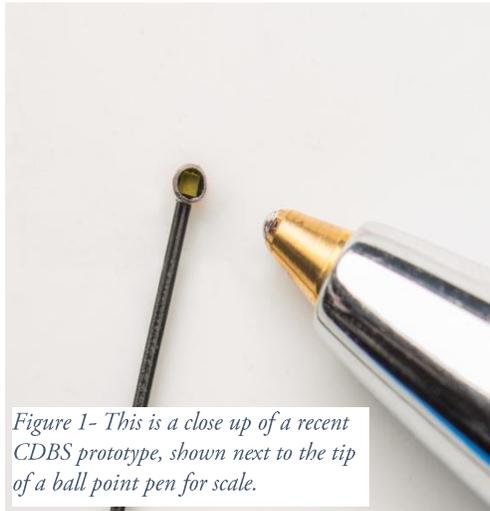ed on all beamlines. Indeed, most of the x-rays used in a typical crystallography experiment pass through the sample, and in most cases the beamstop is a simple beam-blocking device which serves no other useful purpose.

At the Berkeley Center for Structural Biology at Lawrence Berkeley National Lab (LBNL), a tiny device - the Compact Dynamic Beamstop (CDBS) - has been developed. Through a combination of micromanufacturing techniques and fluorescence detection methods, the CDBS's design makes use of those excess x-rays and transforms a simple beam-blocker into a real-time inline measurement device for beam intensity. Having access to information about the beam that interacts with users' protein samples will enable users to extract as much information as possible from each sample. This in turn has the capacity to greatly increase the rate at which both important biological information and potentially life-saving drugs can be introduced to the world. Currently there is nothing commercially available that can do what the CDBS does; prototype devices from other institutions that attempt to accomplish the same goal do not have the same desirable overlap of compact size, signal strength, and quick response time. These characteristics make it very appealing as a technology, and as such it has been licensed from LBNL by a company that will be introducing it to the marketplace in July, 2016.

The development of the CDBS was greatly facilitated by access to the COMPRES-supported laser miller at LBNL. The prototyping process would have been prolonged – and potentially impossible – without it. Throughout this process, the laser miller was used to produce a number of components in CDBS prototype devices (shown in Figure 2), making it an invaluable resource.
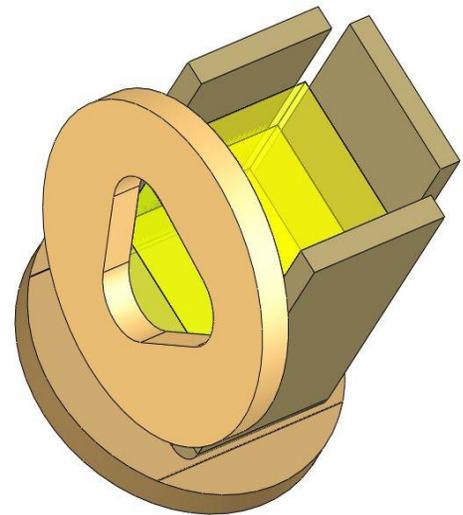


*Figure 2-This is a snapshot from a 3D model of a portion of an early CDBS prototype. All components shown were cut on the COMPRES supported laser miller.*

# Center for X-Ray Optics (CXRO) Contributions to the APEX-UED Project.

Nord Andresen, CXRO, LBNL

COMPRES-related facility: Laser Miller at the Advanced Light Source

The APEX (Advanced Photo-injector EXperiment) project at LBNL revolves around a high repetition-rate electron gun, which has paved the way towards the megahertz electron sources needed for the next generation of free electron lasers. This electron source has also been studied for direct sample probing using ultrafast electron scattering and diffraction techniques. The electron beam is very small, but does require some collimation. The following is a description of how the COMPRES-supported laser miller assisted in the fabrication of collimating masks for the APEX-UED (Ultrafast electron diffraction) project.



Figure 1-Engineering drawings of collimator mask assembly

The collimator mask assembly consists of a series of beam collimating apertures with various sizes. The aperture is positioned in front of our illuminating source (electron beam), and is used to adjust the beam size that illuminates our sample. The smaller apertures have a high aspect ratio (10um aperture has a 50:1 aspect ratio) in order to reflect or deflect the unused high energy electrons to large angles and away from the sample. Due to the extreme difficulties in drilling small holes with high aspect ratios in Tungsten, the apertures themselves are machined into 3-mm diameter by 100um thick discs, and are stacked to achieve a final aperture length of 500um (material thickness to block a 1MV e-Beam). The location tolerance of the aperture relative to the outside diameter (OD) of the disc required sub-micro precision in order for the design to function. This high precision alignment was achieved by machining the OD of the disc and aperture in a single set-up on the laser mill.



Figure 2-Finished collimator mask assembly

# Nuclear Resonant Inelastic X-ray Scattering at High Pressure and Low Temperature

Wenli Bi[ab], Jiyong Zhao[b], Jung-Fu Lin[cd], Quanjie Jia[e], Michael Y. Hu[b], Changqing Jin[f],
Richard Ferry[g], Wenge Yang[dg], Viktor Struzhkin[h] and E. Ercan Alp[b]

[a]Univeristy of of Illinois at Urbana-Champaign, Urbana, IL
[b]Advanced Photon Source, Argonne National Laboratory, Argonne, IL
[c]The University of Texas at Austin, Austin, TX,
[d] Center for High Pressure Science and Technology Advanced Research, Shanghai,China
[e]Institute of High Energy Physics, Chinese Academy of Sciences, Beijing, China
[f]Insitute of Physics, Chinese Academy of Sciences, Beijing, China
[g]HPSynC, Carnegie Institution of Washington, Argonne, IL
[h]Geophysical Laboratory, Carnegie Institution of Washington, Washington, DC
(COMPRES-related facilities: Advanced Photon Source, beamline 3-ID)

A new synchrotron radiation experimental capability of coupling nuclear resonant inelastic X-ray scattering with the cryogenically cooled high-pressure diamond anvil cell technique has been developed. The new technique permits measurements of phonon density of states at low temperature and high pressure simultaneously, and can be applied to studies of phonon contribution to pressure- and temperature-induced magnetic, superconducting and metal–insulator transitions in resonant isotope-bearing materials. $EuFe_2As_2$ is used as an example to demonstrate this new capability at beamline 3-ID of the Advanced Photon Source, Argonne National Laboratory. The Fe-specific phonon density of states and magnetism from the Fe sublattice in $Eu^{57}Fe_2As_2$ at high pressure and low temperature were derived using this new capability.

Figure 1 (top) Picture of the miniature panoramic DAC. (Left) Cylindrical piece. Two wide windows are cut to provide large solid angles for fluorescence signals reaching APD detectors. (Middle) Piston of the DAC with a diameter of 20.3 mm. (Right) Four screws used on the piston for pressure application. (bottom) Picture of the HP–LT NRIXS setup at 3-ID-B. Two APDs are mounted on the top and bottom of the vacuum shroud of the cryostat. The window w4 shown provides optical access of the ruby fluorescence signals for pressure determination as well as allowing the measurement of SMS by a forward APD.

Figure 2 (Left) NRIXS spectra of Eu57Fe2As2 under high pressures and 24 K (solid lines) and instrumental resolution function (red dashed lines) measured by SMS. The intensity of the resolution function is scaled to the elastic peak intensity in the NRIXS spectra. (Right) Derived Fe specific PDOS.
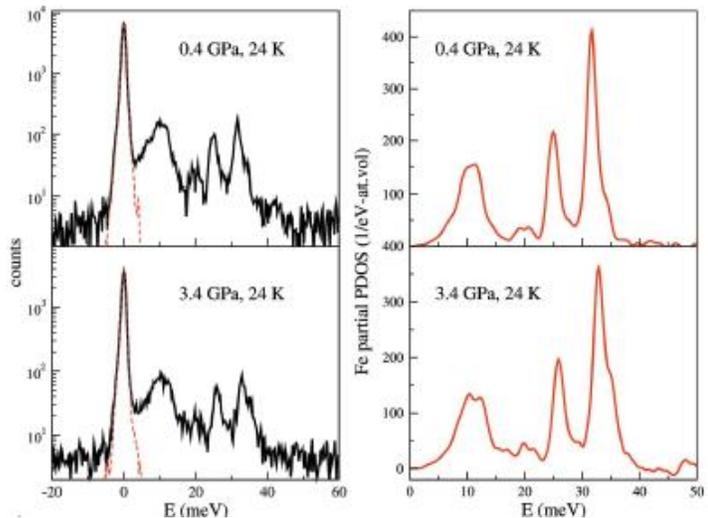
**References:** W. Bi, J. Zhao, J. Lin, Q. Jia,, M.Y. Hu, C. Jin, R. Ferry, W. Yang, V. Struzhkin, and E.E. Alp, J. Synchrotron Radiat. **22**, 760 (2015).

# Intercomparison of pressure standards (Au, Pt, Mo, MgO, NaCl and Ne) to 2.5 Mbar

*S. M. Dorfman, Department of Geosciences, Princeton University, Princeton, NJ, USA*
*V. B. Prakapenka, Center for Advanced Radiation Sources, University of Chicago, Argonne, Illinois, USA.*
*Y. Meng, High-Pressure Collaborative Access Team, Argonne National Laboratory, Carnegie Institution of Washington, Argonne, Illinois, USA*
*T. S. Duffy, Department of Geosciences, Princeton University, Princeton, NJ, USA*
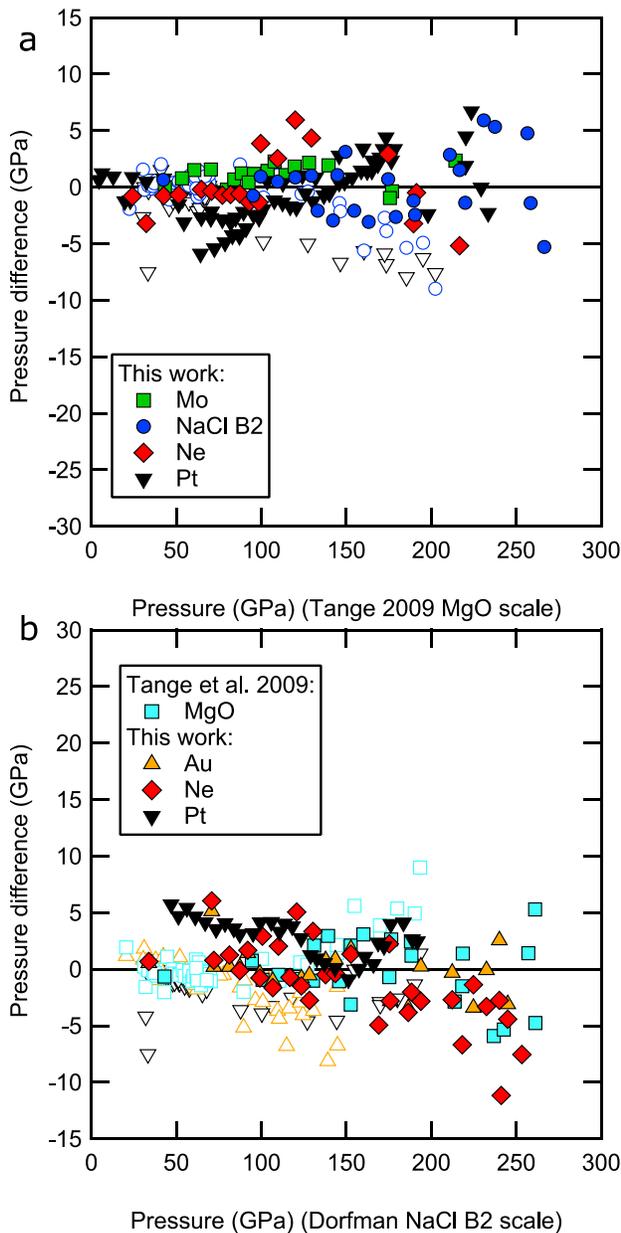
Experiments at extreme pressures in diamond anvil cells rely on internal standards to determine the stress state. Existing calibrations for these standards deviate by as much as 10-15% at Mbar pressures. These differences are due to large extrapolations and uncertainties in equation of state parameters as well as systematic effects of deviatoric stresses. To quantify and minimize uncertainties in pressure calibration, X-ray diffraction experiments were performed at APS sectors HPCAT and GSECARS on mixtures of common pressure standards co-compressed to pressures reaching 2.5 Mbar. Deviatoric stresses were minimized by loading quasi-hydrostatic Ne and He pressure-transmitting media using the COMPRES/GSECARS gas loading facility. New equations of state were fit for each material with internal agreement of ~3% at Mbar pressures. Differences in pressures observed for different standards are comparable to the differential stress supported by the pressure medium. Analysis of diffraction line widths suggests that Ne and He are equally effective at providing quasi-hydrostatic stress conditions at 2.5 Mbar.

**Figure 1: Differences in calculated pressures for equation of state fits for all materials studies relative to a) MgO b) NaCl.**

Reference: Dorfman, S.M., Prakapenka, V.B., Meng, Y., and Duffy, T.S. (2012). Journal of Geophysical Research, 117, B08210.

# Combined Resistive and Laser Heating Technique for *in-situ* Radial X-ray Diffraction in the Diamond Anvil Cell at High Pressure and Temperature

Lowell Miyagi, Waruntorn Kanitpanyacharoen, Selva Vennila Raju, Pamela Kaercher, Jason Knight, Alastair MacDowell, Hans-Rudolf Wenk, Quentin Williams, and Eloisa Zepeda Alarcon, U. Utah, UCB, ALS, and UCSC

(COMPRES-related facilities: ALS 12.2.2)

A Liermann-type diamond anvil cell with radial diffraction geometry (rDAC) was redesigned and developed for synchrotron X-ray diffraction experiments at beamline 12.2.2 of the Advanced Light Source (ALS). The rDAC, equipped with graphite heating arrays, allows simultaneous resistive and laser heating while the material is subjected to high pressure. Three different geomaterials were used as pilot samples to calibrate and optimize conditions for combined resistive and laser heating. For example, in Run#1, FeO was loaded in a boron-mica gasket and compressed to 11 GPa then gradually resistively heated to 1010 K (1073 K at the diamond side). The laser heating was further applied to FeO to raise temperature to 2273 K. In Run#2, Fe-Ni alloy was compressed to 18 GPa and resistive heated to 1785 K (1973 K at the diamond side). The combined resistive and laser heating was successfully performed again on $(Mg_{0.9}Fe_{0.1})O$ in Run#3. In this instance, the sample was loaded in a boron-kapton gasket, compressed to 29 GPa, resistive-heated up to 1010 K (1073 at the diamond side), and further simultaneously laser-heated to achieve a temperature in excess of 2273 K. Diffraction patterns obtained from the experiments were deconvoluted using the Rietveld method and quantified for lattice preferred orientation of each material under extreme conditions and during phase transformation.
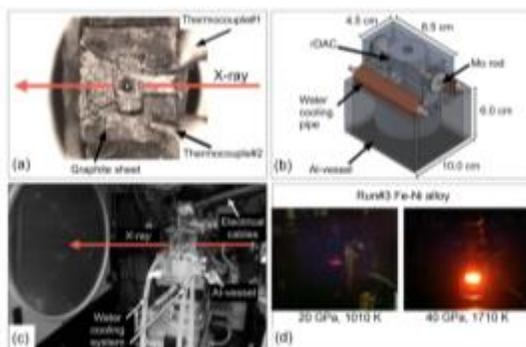


Figure 1 of Miyagi et al. (2013). Schematic of (a) a graphite heater carved for gasket dimension and X-ray beam paths, (b) the redesigned rDAC assembled in the Al-vessel, (c) the experimental setup for combined resistive and laser heating, and (d) resistive heating images on Fe–Ni alloy in Run#3 at 1007 K (left) and 1713 K (right).

Figure. 4 of Miyagi et al. (2013): The P-T path followed the rDAC experiments and selected inverse pole figures (IPFs) obtained from Run#1: FeO and Run#3: $(Mg_{0.9}Fe_{0.1})O$ at various pressure and temperatures. IPFs show the probability of finding the pole (normal) to a lattice plane in the compression direction.
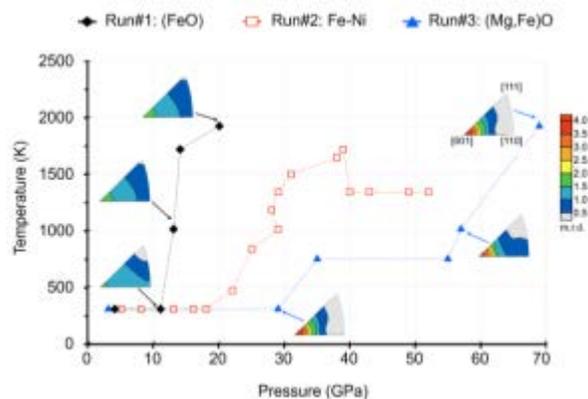
Reference: L. Miyagi, W. Kanitpanyacharoen, S. V. Raju, P. Kaercher, J. Knight, A. MacDowell, H.-R. Wenk, Q. Williams, and E. Z. Alarcon (2013), Combined resistive and laser heating technique for in situ radial X-ray diffraction in the diamond anvil cell at high pressure and temperature, *Review of Scientific Instruments*, *84*(2), 25118-25118–9.

# Resistive heater developments at BL 12.2.2

Jinyuan Yan, Alastair MacDowell, Martin Kunz, Andrew Doran, Christine Beavers, and Quentin Williams  UCSC, LBNL

(COMPRES-related facilities: ALS 12.2.2)

Physical properties as a function of pressure and temperature are of fundamental importance for geoscience and material science. High temperature in a diamond anvil cell is achieved by either resistive heating or laser heating. While laser heating works in the temperature range above ~ 1000 K, resistive heating covers the low and intermediate temperature range between room temperature and ~ 1000 K. The major problems with most current resistive heating designs are that (1) they are hard to assemble and have very low success rate (not good for a user facility) and /or (2) their maximal temperatures are far below the laser heating range.
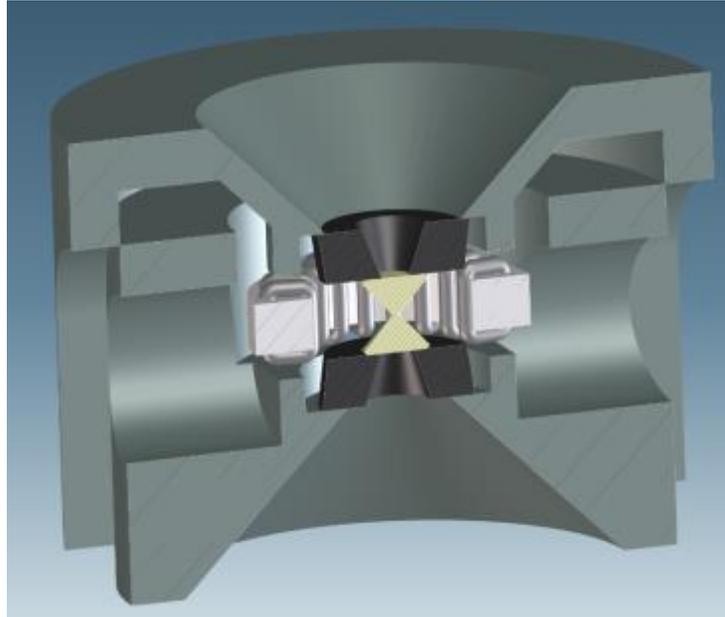


Figure 1. Schematic for the cross section of BX90 cell with a tungsten wire heater.

In this project, we developed a modular, plug-play ring resistive heater tailored to the BX90 DAC to push the regular heating temperature up to 1300K. The BX 90 lends it well for such a design since it offers relatively large space around the diamonds within the DAC body (Figure 1). The design of the heater is based on a doughnut shaped alumina ceramic core with a 0.5 mm diameter tungsten wire coiled around it. This assembly has been made in-house. Parallel we are also exploring a ring heater assembly manufactured by a local company. Reliability comparisons are under way. Commissioning experiments in inert atmosphere reached 1300 K where it stayed stable for several hours.

# Compact Low Power In-situ Infrared Tube Furnace for X-ray Powder Diffraction

Andrew Doran, L. Schlicker, C. M. Beavers, M.F. Beckheet, and A. Gurlo, LBNL – ALS, UC Santa Cruz, University of Darmstadt, University of Berlin

(COMPRES-related facilities: ALS 12.2.2)

This describes the development and implementation of a compact, low power, in-situ infrared heated, tube furnace for powder X-ray diffraction experiments. Our Silicon Carbide (SiC) based furnace design exhibits outstanding thermal performance in terms of accuracy control and temperature ramping rates while simultaneously being easy to use, robust to abuse and, due to its small size and low power, producing minimal impact on surrounding equipment. Temperatures in air in excess of 1100°C can be controlled at an accuracy of better than 1%, with temperature ramping rates up to 100°C/sec. The complete "add-in" device, minus power supply, fits in a cylindrical volume approximately 15cm long and 6cm in diameter and resides as close as 1 cm from other sensitive components of our experimental synchrotron endstation without adverse effects.

Most common designs for ambient pressure heaters suffer from a series of problems related to bulky geometry making it hard for in-situ studies or differential thermal absorption between thermo-couple and samples, thus making accurate temperature determination difficult.

Our solution to these issues is to radiatively heat by IR lamps a small tube, 2mm outside diameter by 1mm inside diameter, made of SiC and to place the sample under test inside this miniature "tube furnace" (Figure 1) . We achieve a sample and thermocouple environment inside the furnace where all objects reach thermal equilibrium for accurate temperature determinations, while at the same time heating only a few 10s of grams of material. This second point makes for both a very low power device with minimal impact on surrounding equipment and one with the possibility for very fast temperature changes.

A temperature of 1200°C can be reached while applying a total power of 150W to the lamps. At this power the lamp mounting bracket reaches approximately 85°C at its hottest point and can easily reside in close proximity to other parts of our experimental apparatus with no need for further effort to mitigate adverse effects beyond avoiding direct contact.
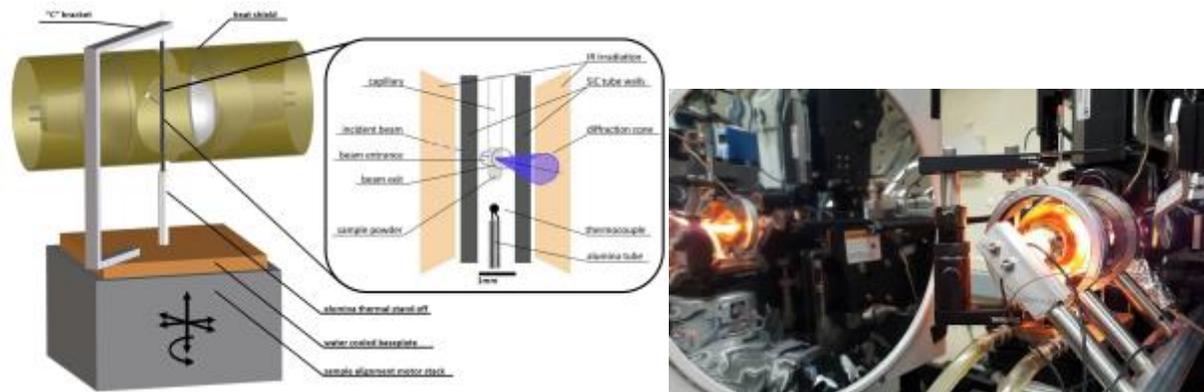


**Figure 1.** Schematics of the design of the IR tube furnace (left) and installation on beamline 12.2.2.

References: A. Doran, L. Schlicker, C.M. Beavers, M.F. Beekheet, A. Gurlo (2016), Compact Low Power In-situ Infrared Tube Furnace for X-ray Powder Diffraction, *Rev. Scie. Instrum,* submitted.

# A new double sided laser heating set-up at ALS beamline 12.2.2

Martin Kunz, Alastair MacDowell, Jinyuan Yan and Quentin Williams, ALS - LBNL

(COMPRES-related facilities: ALS 12.2.2)

COMPRES supported beamline 12.2.2 at the ALS has two focus areas, namely high-pressure single crystal diffraction (end-station 1) and in-situ laser heating of samples in a diamond anvil cell (end station 2). The original laser heating set-up suffered from vibration issues connected to long mechanical arms and an outdated pyrometry approach.
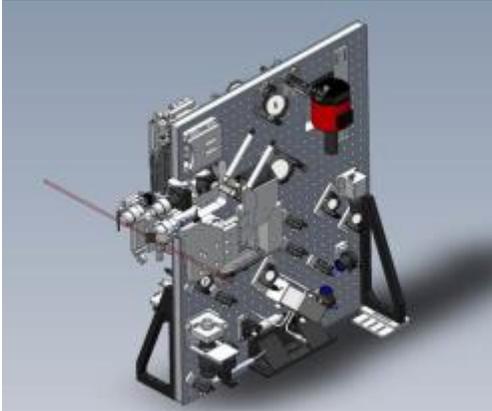


**Figure 1:** 3-d model of breadboard containing the optical set-up for the double sided laser heating. The set-up is mounted on the experimental table perpendicular to the X-ray beam; the laser beam in the default axial mode travels parallel to the X-rays

The entire set-up was redesigned, installed, commissioned and is in successful user operation. The new design reduced the mechanical arm considerably by condensing up- and downstream optics onto two sides of a vertically standing 1 m x 1 m breadboard (Figure 1). As in the old set-up, two 100 W SPI 1090 nm fiber lasers provide the laser source, including a collinear red He-Ne alignment laser. This together with a high degree of automation (focusing lens, corner mirrors, insert stages) allows for safe remote alignment for practically all alignment procedures. The design proves to be very robust and stable against non-expert operation as is common in a user facility.

The peak scaling method is used to extract temperature maps from the laser heated hot spot. On each side, the entire image is focused onto a 1-dimensional spectrometer (OceanOptics Jaz). The temperature deduced from the averaged intensity is combined with a 14 bit monochromatic (700 nm) image of the hotspot. The real peak temperature is deduced in an iterative way by comparing the observed average intensity curve with a calculated curve based on the monochromatic image and the to be optimized peak temperature (Figure 2).
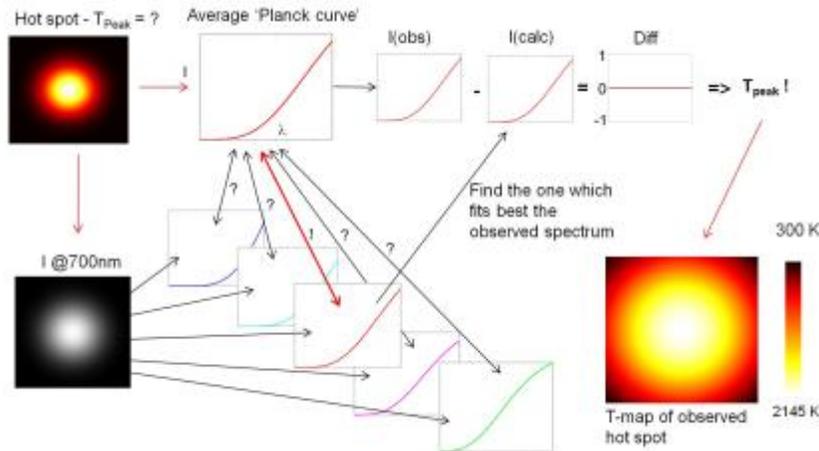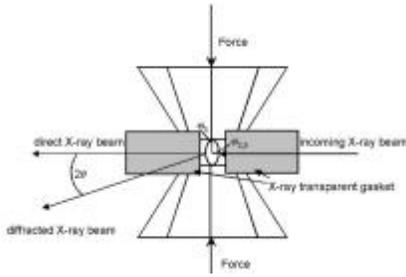


**Figure 2:** Schematic of the iterative method to deduce the correct peak temperature for an associated average temperature deduced from the entire hotspot. The observed average intensity curve is compared with a calculated curve based on the peak temperature (the optimized variable) and the monochromatic intensity map.

# A double-sided in-situ radial laser heating set-up at ALS beamline 12.2 2

Martin Kunz, Jinyuan Yan, Alastair MacDowell, Christine Beavers and Quentin Williams, ALS – LBNL, UC Santa Cruz

(COMPRES-related facilities: ALS 12.2.2)



**Figure 1:** Schematic of radial X-ray diffraction geometry

Radial diffraction in a diamond anvil cell (DAC) is employed to probe the elastic and plastic response of material to an anisotropic stress field (Figure 1). It uses the azimuthal variation of intensity and diffraction angle to deduce plastic reorientation as well as strength of material and with that helps to understand the dynamics of the Earth's mantle and solid core.

A major criticism of such experiments is that they are done at ambient temperature and thus its results are inconclusive with respect to what is happening in the deep Earth.

An in situ laser heating set up allowing for simultaneous double sided heating including peak scaling method pyrometry and radial X-ray diffraction has been installed on beamline 12.2 2. It relies on the radial DAC being rotated by 90 degrees relative to the incoming X-ray beam with the axial cell direction being horizontal and perpendicular to the X-ray beam. The set up consists on an automated periscope drop-in on the axial downstream side for the 90 degrees set up (Figure 2), and a manually installed mini laser table intercepting the straight-through upstream side for the 270 degree side (Figure 3).

Commissioning experiments on AgI and $ZrSiO_4$ showed very high image quality and stable heating at > 50 W for up to one hour.
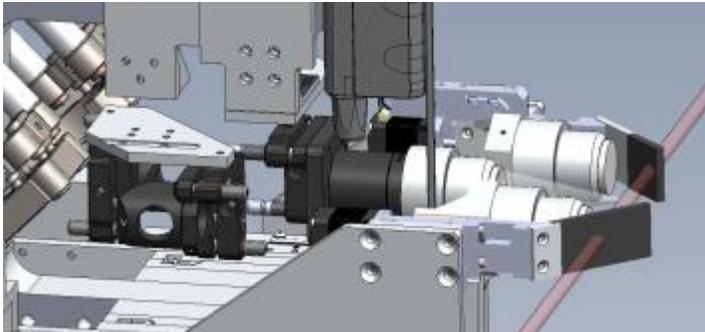


**Figure 2:** Close up 3d-drawing of periscope insert intercepting the downstream laser and image path for the 90 degree heating
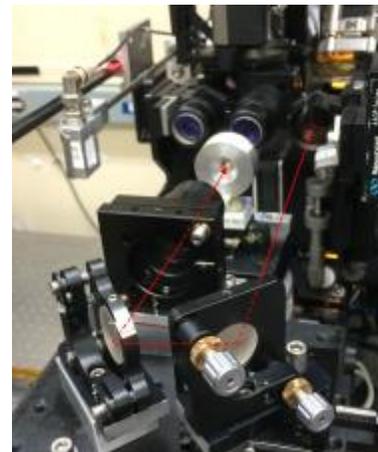


**Figure 3:** Mini table with 2 mirrors and a lens for the 270 degree heating. Red laser indicates the upstream beam intercepted by the set up

# Combined resistive and laser heating technique for in situ radial X-ray diffraction in the diamond anvil cell at high pressure experiments and temperature

To extend the range of high-temperature, high-pressure studies within the diamond anvil cell, a Liermann-type diamond anvil cell with radial diffraction geometry (rDAC) was redesigned and developed for synchrotron X-ray diffraction experiments at beamline 12.2.2 of the Advanced Light Source. The rDAC, equipped with graphite heating arrays, allows simultaneous resistive and laser heating while the material is subjected to high pressure. The goals are both to extend the temperature range of external (resistive) heating and to produce environments with lower temperature gradients in a simultaneously resistive- and laser-heated rDAC. Three different geomaterials were used as pilot samples to calibrate and optimize conditions for combined resistive and laser heating. For example, in Run#1, FeO was loaded in a boron-mica gasket and compressed to 11 GPa then gradually resistively heated to 1007 K (1073 K at the diamond side). The laser heating was further applied to FeO to raise temperature to 2273 K. In Run#2, Fe–Ni alloy was compressed to 18 GPa and resistively heated to 1785 K (1973 K at the diamond side). The combined resistive and laser heating was successfully performed again on $(Mg0.9Fe0.1)O$ in Run#3. In this instance, the sample was loaded in a boron-kapton gasket, compressed to 29 GPa, resistive-heated up to 1007 K (1073 K at the diamond side), and further simultaneously laser-heated to achieve a temperature in excess of 2273 K at the sample position. Diffraction patterns obtained from the experiments were deconvoluted using the Rietveld method and quantified for lattice preferred orientation of each material under extreme conditions and during phase transformation. These experiments demonstrated tremendous potential. Unfortunately, due to lack of funding, the resistive heating program at ALS was discontinued and we have now to conduct experiments at HASY, Hamburg.



28 GPa, 1300 K          40 GPa, 2000 K
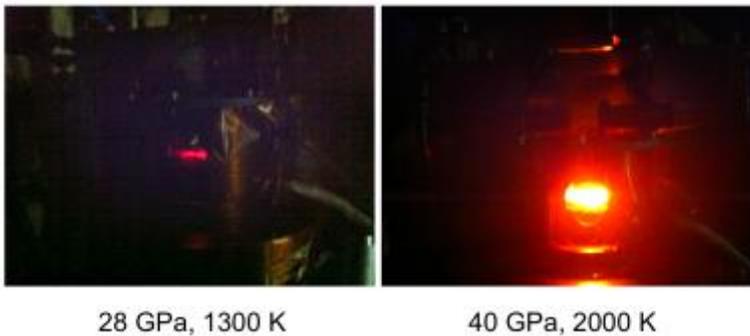
Resistive heating experiments performed at beamline 12.2.2
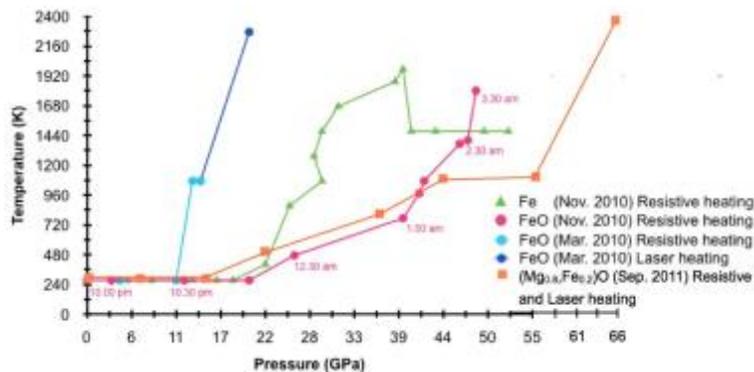


Range of combined resistive and laser heatin in radial diffraction geometry at beamline 12.2.2

Miyagi, L., Kanitpanyacharoen, W., Raju, V., Kaercher, P., Knight, J., McDowell, A., Wenk, H.R., Williams, Q., Zepeda, E. (2013). . *Rev. Sci. Instr*. 84, 025118, 1-9

**Complex multiphase materials and diamond anvil cell experiments**

Synchrotron X-ray diffraction images are increasingly used to characterize crystallographic preferred orientation distributions (texture) of fine-grained polyphase materials. Diffraction images can be analyzed quantitatively with the Rietveld method as implemented in the software package Materials Analysis Using Diffraction. Here we describe the analysis procedure for diffraction images collected with high energy X-rays for a complex, multiphase shale, and for those collected in situ in diamond anvil cells at high pressure and anisotropic stress.
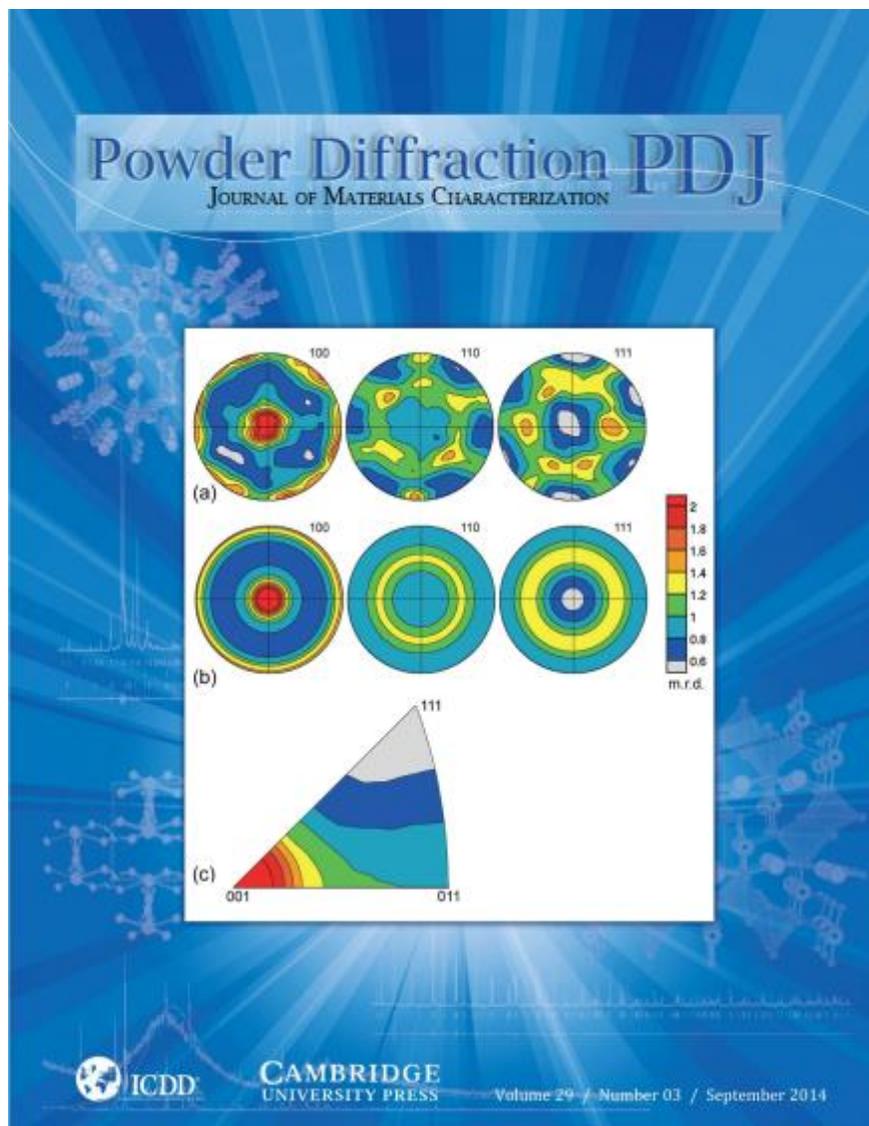


The research conducted on 12.2.2. made it to the front cover of the journal Powder Diffraction

Wenk, H.-R., Lutterotti, L., Kaercher, P., Kanitpanyacharoen, W., Miyagi, L., Vasin, R. (2014). Rietveld texture analysis from synchrotron diffraction images: II. Complex multiphase materials and diamond anvil cell experiments. *Powder Diffraction* 29, 220-232.

# Deformation T-Cup: a new controlled strain-rate high-pressure deformation apparatus

The X17B2 side-station beam-line has been host to a new style multi-anvil deformation apparatus, based on the widely used 6-8 split-cylinder geometry. This new apparatus has been used in deformation experiments at pressures in excess of 18 GPa at room temperature and 10 GPa at high temperatures.

In 6-8 (Kawai-type) devices the sample assembly is compressed by eight cubic anvils which in turn are confined by 6 outer wedges. In the new apparatus the two cubes which sit along the split-cylinder axis have been replaced by hexagonal cross section anvils (figure 1). Combining these hexagonal-anvils with secondary differential actuators incorporated into the load frame (figure 2), for the first time, enables the 6-8 multi-anvil apparatus to be used for controlled strain-rate deformation experiments to high strains. Testing of the design, both with and without synchrotron-X-rays, has demonstrated the Deformation T-Cup (DT-Cup) is capable of deforming 1–2 mm long samples to over 55% strain at high temperatures and pressures. To date the apparatus has been calibrated to, and deformed at, 18.8 GPa and deformation experiments performed in conjunction with synchrotron X-rays at confining pressures up to 10 GPa at 800 °C.

Post-commissioning, controlled strain-rate experiments, at pressures up to 10 GPa have been performed investigating the relative strength of the $SiO_2$ polymorphs. In these experiments, each of the $SiO_2$ polymorphs was deformed with olivine and the strains measured by X-radiography. The strength of the polymorph can then by normalised to that of olivine. These experiments show that the viscosity of stishovite is greater than that of coesite which is greater than that of quartz. The strength of the minerals therefore increases with the stabilisation pressure.

(Simon Hunt, Richard McCormack, Edward Bailey, Matthew Whittaker, David Dobson, Don Weidner, Li Li; Published as: Hunt et al., 2014, Rev. Sci. Inst., 85, 085103)
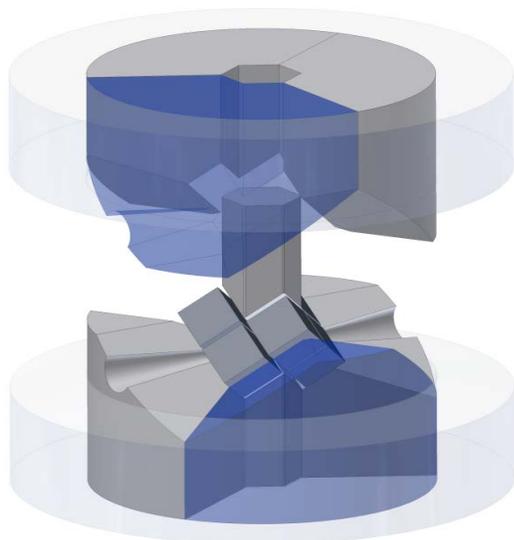


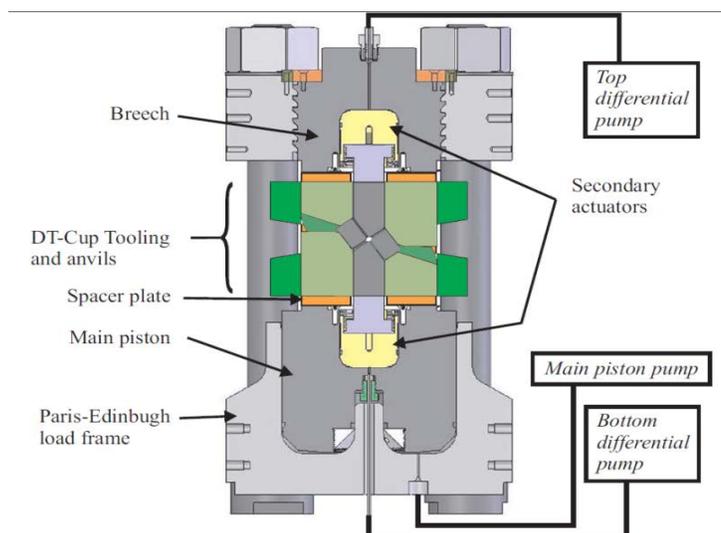Figure 1: Illustration of the DT-Cup tooling.



Figure 2: Illustration of Dt-Cup press and tooling.

# Introducing DIASCoPE: Directly Integrated Acoustic System Combined with Pressure

Experiments: System and Design - Matthew L. Whittaker, Kenneth J. Baldwin, William B. Huebsch, Haiyan Chen, Michael T. Vaughan and Donald J. Weidner

Samples and Science – Matthew L. Whitaker, Frederic Bejina, Misha Bystricky, Nicolas Terce

Understanding the properties and behaviors of materials and multi-phase aggregates under conditions of high pressure and temperature is vital to unraveling the mysteries that lie beneath the surface of the planet. Advances in *in situ* experimental techniques using synchrotron radiation at these extreme conditions have helped to provide answers to fundamental questions that were previously unattainable. Synchrotron-based ultrasonic interferometry measurements have proven to be especially important in determining acoustic velocities and thermoelastic properties of materials at high pressures and temperatures. However, due to relatively slow data collection times, it has been difficult to measure the effects of processes as they occur, and instead the measurement is made on the end product of these processes. DIASCoPE is an important step toward addressing this problem.

Over the last three years, we have designed and developed an on-board ultrasonic acoustic velocity measurement system that cuts data collection time down by over an order of magnitude. We can now measure P- and S-wave travel times in samples at extreme conditions in less than one second. Moreover, the system has been fully integrated with the multi-anvil apparatus and the EPICS control system at beamline X17B2 of the National Synchrotron Light Source, allowing for greater ease of control *and* full automation of experimental data collection. The DIASCoPE has completed the testing and commissioning phase, and the first data collected using this powerful new system is presented here.
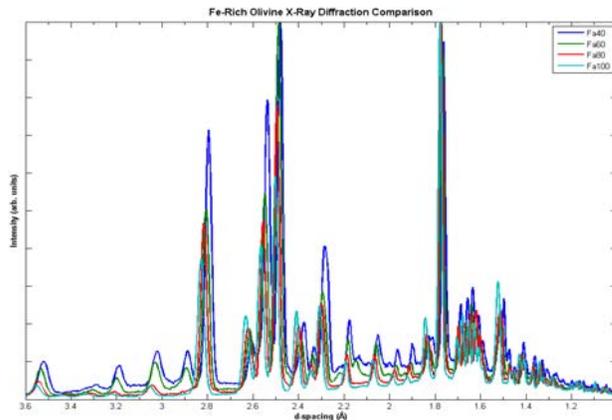


As a collaboration between Stony Brook and Toulouse, we have begun investigating the effects of iron content on the thermoelastic properties and acoustic velocities of iron-rich olivine. While there have been several studies on the Mg-rich side of this solid solution series, there is virtually none on the Fe-rich side, which is something we hope to rectify in this study. Below are three figures showing a very preliminary comparison of the first four samples studied in this investigation: Fa100, Fa80, Fa60, and Fa40.
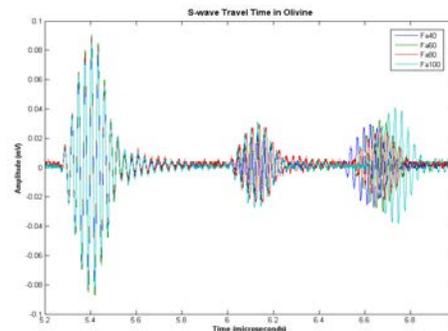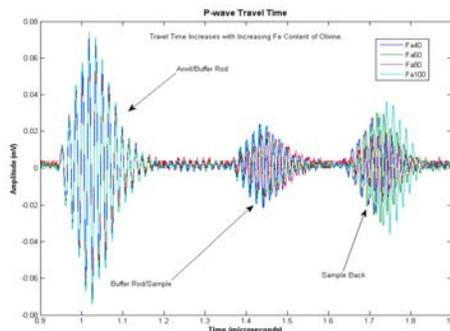
As these figures clearly show, there is a progressive change in d-spacing, P-, and S-wave velocities with Fe content of the olivine.

# The Strength of Ruby from X-ray Diffraction Under Nonhydrostatic Compression to 68 GPa

Haini Dong[1, 2, 3], Susannah M. Dorfman[2], Jianghua Wang[1], Duanwei He[1], and Thomas S. Duffy[2]

[1]*Institute of Atomic and Molecular Physics, Sichuan University, Chengdu 610065, China*
[2]*Department of Geosciences, Princeton University, Princeton, NJ, 08544 USA*
[3]*Institute of Geophysics, Chinese Academy of Sciences, Guiyang 550002, China*

The strength and mechanical properties of hard ceramics are required for their applications under extreme static and dynamic mechanical stresses and high pressures. Aluminum oxide, $Al_2O_3$, has many useful mechanical properties such as high hardness, wear resistance, and fracture toughness, combined with chemical inertness and thermal stability. Ruby ($\alpha$-$Al_2O_3$: $Cr^{3+}$) has been a widely used pressure standard for static high-pressure experiments since the 1970s. Given the importance of ruby in high-pressure science, complete characterization of this fundamental material is needed. In this study, ruby was compressed to 68 GPa under non-hydrostatic conditions in a diamond anvil cell (DAC). Angle-dispersive X-ray diffraction experiments in a radial geometry were conducted at beamline X17C of the National Synchrotron Light Source. The stress state of ruby at high pressure and room temperature was analyzed based on the measured lattice strain. The differential stress of ruby increases with pressure from 3.4% of the shear modulus at 18.5 GPa to 6.5% at 68.1 GPa. The polycrystalline ruby sample can support a maximum differential stress of 16 GPa at 68.1 GPa under non-hydrostatic compression (left-hand figure). The results of this study provide a better understanding of the mechanical properties of this important material for high-pressure science. Through a synthesis of our new ruby data together with high-pressure yield strength measurements on a range of strong solids (right-hand figure), we show a correlation between static yield strength and Vickers hardness that provides a useful guideline to relate the hardness at ambient conditions with high-pressure yielding behavior. Thus, the high-pressure yield strength can be used as a proxy for material hardness.
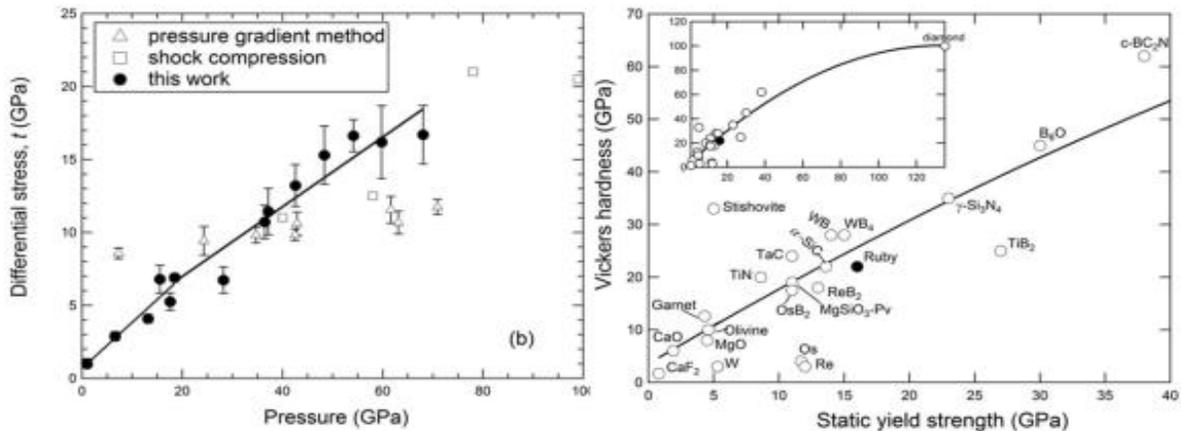
Left: Differential stress in ruby as a function of pressure. Solid circles: this work; solid lines: linear fits to the present data. Right: Vickers hardness vs. high-pressure yield strength for selected ceramic materials and metals. The solid lines are polynomial fits to the data. The inset shows the yield strength-Vickers hardness relationship including diamond.

## Reference

Dong, H., S. M. Dorfman, J. Wang, D He, and T. S. Duffy, The strength of ruby from high-pressure X-ray diffraction to 68 GPa, *Physics and Chemistry of Minerals*, 41, 527-535, 2014.

# Compression of a multiphase mantle assemblage: Effects of undesirable stress and stress annealing on the iron spin state crossover in ferropericlase

Konstantin Glazyrin[1,2], Nobuyoshi Miyajima[3], Jesse S. Smith[4], and Kanani K.M. Lee[1]

[1]Department of Geology and Geophysics, Yale University, New Haven, Connecticut, USA
[2]FS-PE Group, DESY, Hamburg, Germany
[3]Bayerisches Geoinstitut, Universität Bayreuth, Bayreuth, Germany
[4]High Pressure Collaborative Access Team, Argonne National Laboratory, Argonne, Illinois, USA

(COMPRES-related facilities: COMPRES gas-loading system at GSECARS)

Using synchrotron-based x-ray diffraction (Figure 1), we explore characteristic signatures for nonhydrostatic stresses and their effect on the spin state crossover of ferrous iron in (Mg, Fe)O ferropericlase (Fp) (Figure 2) upon compression in a two-phase mixture which includes an Al- and Fe-bearing bridgmanite (Bm). We observe an influence of nonhydrostatic stresses on the spin state crossover starting pressure and width. The undesirable stresses discussed here include uniaxial deviatoric stress evolving in the diamond anvil cell and effects of intergrain interaction. While the former leads to a pressure overestimation, the latter one lowers the pressure of the onset for the high-spin to low-spin electronic transition in $Fe^{2+}$ in ferropericlase (Mg, Fe)O with respect to hydrostatic conditions.
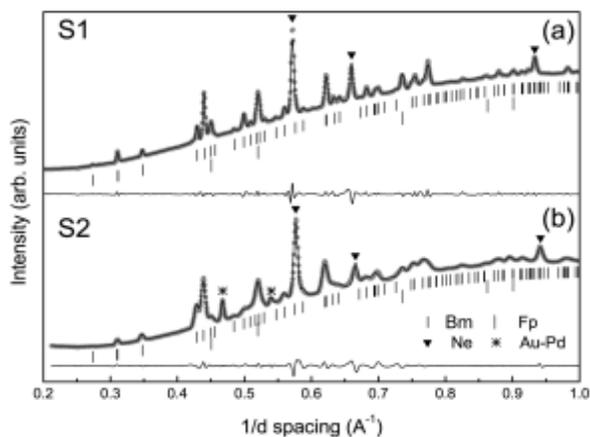
**Figure 1.** X-ray diffraction patterns collected at room temperature after laser annealing for (a) S1 and (b) S2 samples. Different symbols shown represent (black ticks) Bm, (grey ticks) Fp, (black triangle) Ne, and (star) Au-Pd. Black line passing through the light grey data points corresponds to LeBail fit of the data. Note considerable broadening in case of S2 and considerable amount of Ne phase detected in each case. Patterns (a) and (b) were collected 79 GPa and 88 GPa (Ne pressure scale) respectively. Residuals of the fit are shown with a thin line.
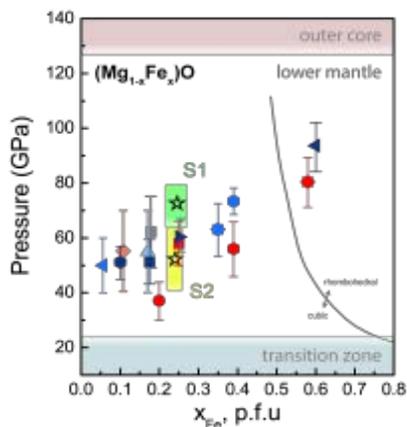


**Figure 2.** Phase diagram of ferropericlase ($Mg_{1-x}Fe_xO$) with room temperature literature data on spin state crossover. From left to right: light blue left triangle x=0.06 [*Crowhurst et al.*, 2008]; dark blue hexagon x=0.1 [*Marquardt et al.*, 2009]; light red diamond x=0.11 [*Irifune et al.*, 2010]; light blue triangle x=0.17 [*Antonangeli et al.*, 2011]; dark blue square x=0.17 [*Lin et al.*, 2005]; gray square x=0.17 [*Badro et al.*, 2003]; red circle x=0.2 [*Fei et al.*, 2007a]; red square x=0.25 [*Mao et al.*, 2011]; dark blue right triangle x=0.25 [*Lin et al.*, 2005]; light blue star x=0.35 [*Chen et al.*, 2012]; red hexagon x=0.39 [*Fei et al.*, 2007a]; light blue hexagon x=0.39 [*Zhuravlev et al.*, 2009]; dark blue left triangle x=0.4 [*Lin et al.*, 2005]; red star x=0.58 [*Fei et al.*, 2007a]. Red symbols indicate sample annealing, while blue and gray symbols indicate no temperature treatment. Triangles indicate single crystal loadings. Error bars correspond to the apparent width of transition. The green and yellow regions indicate spin state crossover regions as determined for $Fp_{S1}$ (hydrostatic conditions) and $Fp_{S2}$ (strictly non-hydrostatic conditions), respectively.

# The 8-Shooter: A Rotatable X-Ray Pinhole Assembly for Beamline 8.3.1

George Meigs &James Holton, Physical Bioscience Division, LBNL

COMPRES-related facility: Laser Miller at the Advanced Light Source

The laser miller was absolutely necessary in fabrication of our rotatable X-ray pinhole assembly A.K.A, "The 8-Shooter" This is an essential component of Beamline 8.3.1; one which is in continual use. The electro-mechanical bits of the 8-Shooter are a 1/4" S.S Tube, rotated by means of Pico Motor Driver fitted with a 40000 counts/turn encoder, powered by a Galil DMC-4040 Motion Controller.
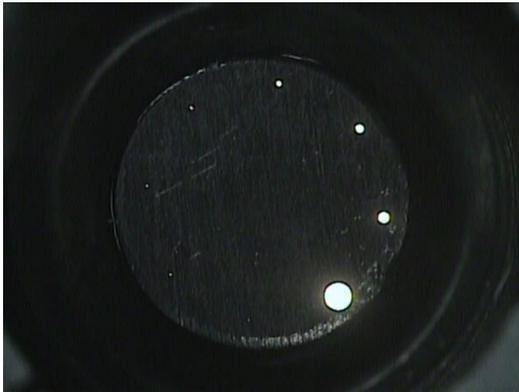


Figure 1-Image of the recessed tantalum pinhole disc.

A 3000um dia. X 100um thick Tantalum disk is glued to the inside of the 1/4" tube, 1.0 millimeter down. Through this Ta disk, on a radius of 1000um, are drilled 8 aperture defining pinholes of diameters 10, 15, 20, 30, 50, 75, 100, and 300 um. On the surface of the 1/4" S.S. tube is glued another Ta disk of 5000um dia. X 100um thick. Through this disk, on the same radius, are drilled 8 holes which function as X-Ray scatter guards, of diameters 20, 30, 40, 50, 75, 100, 130, 330um.

It is essential to have the Pinholes and their associated Scatter Guard Holes coaxial. After practicing a number of test drillings, we were able to first glue both of the Ta disks into place, then drill a Scatter Guard Hole, move the focus of the Laser Cutter down 1000um, then drill the Aperture Defining Pinhole through the Scatter Guard hole, thereby assuring the holes have a common center. This was done by fastening the Pico Motor assembly to X-Y stage of the Mill, positioning the center of rotation of the 1/4" tube 1.000 mm from the Laser Cutter's beam. After each Scatter Guard and Pinhole was drilled, the Tube/Disk assembly was rotated by 40000/8 = 5000 encoder counts, and the next pair were drilled. Of course, the 3000um and 5000um Ta disks had themselves had been previously cut by Laser Mill.



Figure 2- An early version of the 8-Shooter, before scatter-guard drilling was fully integrated.

This device went through a number iterations and refinements to arrive at its current essential form, which enabled data collections for 94 badged users last year.
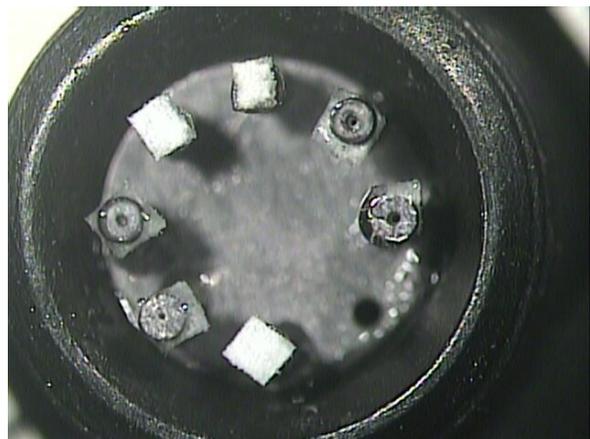
# Acoustic travel time gauges for in-situ determination of pressure and temperature in multi-anvil apparatus

Xuebing Wang, Ting Chen, Xintong Qi, Yongtao Zou, Jennnifer Kung, Tony Yu, Yanbin Wang, Robert Liebermann and Baosheng Li, Stony Brook University and University of Chicago
[COMPRES Cell Assembly Project]

In this study, we developed a new method for in-situ pressure determination in multi-anvil, high-pressure apparatus using an acoustic travel time approach within the framework of acoustoelasticity. The ultrasonic travel times of polycrystalline $Al_2O_3$ were calibrated against NaCl pressure scale up to 15 GPa and 900 _C in a Kawai-type double-stage multi-anvil apparatus in conjunction with synchrotron X-radiation, thereby providing a convenient and reliable gauge for pressure determination at ambient and high temperatures. The pressures derived from this new travel time method are in excellent agreement with those from the fixed-point methods. Application of this new pressure gauge in an offline experiment revealed a remarkable agreement of the densities of coesite with those from the previous single crystal compression studies under hydrostatic conditions, thus providing strong validation for the current travel time pressure scale. The travel time approach not only can be used for continuous in-situ pressure determination at room temperature, high temperatures, during compression and decompression, but also bears a unique capability that none of the previous scales can deliver; i.e., simultaneous pressure and temperature determination with a high accuracy ($\pm$0.16 GPa in pressure and $\pm$17 °C in temperature). Therefore, the new in-situ $Al_2O_3$ pressure gauge is expected to enable new and expanded opportunities for offline laboratory studies of solid and liquid materials under high pressure and high temperature in multi-anvil apparatus.
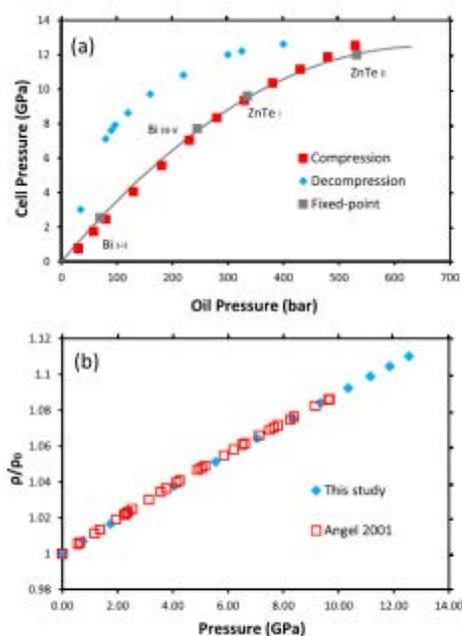
FIG. 5. (a) Comparison of pressure determined using buffer rod as in-situ pressure marker with previous calibration from fixed-point method and (b) densities of coesite from the current study with pressure determined using the travel time pressure scale and comparison with single crystal data of Angel et al. (2001) obtained under hydrostatic conditions.

.
Reference: Wang, X., T. Chen, X. Qi, Y. Zou, J. Kung, T. Yu, Y. Wang, R. C. Liebermann and B. Li, Acoustic travel time gauges for in-situ determination of pressure and temperature in multi-anvil apparatus, J. Appl., 118, 065901, 9pp, 2015.

# Fast temperature spectrometer for samples under extreme conditions

D. Zhang[1,2], J. M. Jackson[1], J. Zhao[2], W. Sturhahn[1], E. E. Alp[2], T. S. Toellner[2] and M. Y. Hu[2]
1. California Institute of Technology, 1200 E California Blvd, Pasadena, CA 91125
2. Advanced Photon Source, Argonne National Laboratory, 9700 S. Cass Ave, Argonne, IL 60439
(COMPRES-related facilities: APS XSD 3-ID-B)

A multi-wavelength Fast Temperature Readout (FasTeR) spectrometer was developed to capture a sample's transient temperature fluctuations, and reduce uncertainties in melting temperature determination. Without sacrificing accuracy, FasTeR features a fast readout rate (about 100 Hz), high sensitivity, large dynamic range, and a well-constrained focus. The temperatures determined by FasTeR outside of the vicinity of melting are in good agreement with results from the charge-coupled device spectrometer. Near melting, FasTeR is capable of capturing transient temperature fluctuations, at least on the order of 300 K/s. A software tool, SIMFaster, is described and has been developed to simulate FasTeR and assess design configurations. FasTeR is especially suitable for temperature determinations that utilize ultra-fast techniques under extreme conditions. Working in parallel with the laser-heated diamond-anvil cell, synchrotron Mössbauer spectroscopy, and X-ray diffraction, the FasTeR spectrometer has been applied to measure the melting temperature of $^{57}Fe_{0.9}Ni_{0.1}$, the major component of Earth's core, at high pressure.
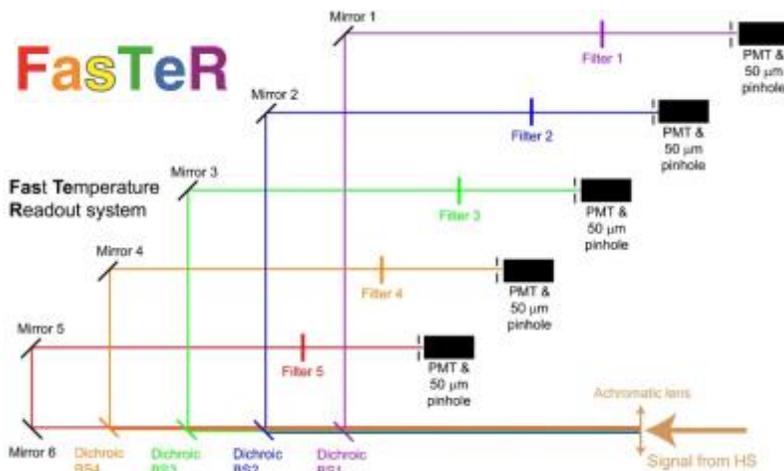
Fig 1: Optical layout of the FasTeR system. PMT: photon multiplier tube. HS: hotspot on the sample.

Fig 2: Determining the melting temperature of $Fe_{0.9}Ni_{0.1}$ at $P_{300K}$ = 29±2 GPa. Black solid dots: temperatures determined from the FasTeR system. Grey empty circles: temperatures determined from the CCD spectrometer. Black curve: best-fit theoretical curve using the FasTeR data. Grey dashed curve: best-fit theoretical curve using the CCD data. For the FasTeR data, ~300 measurements are represented in each temperature value plotted.
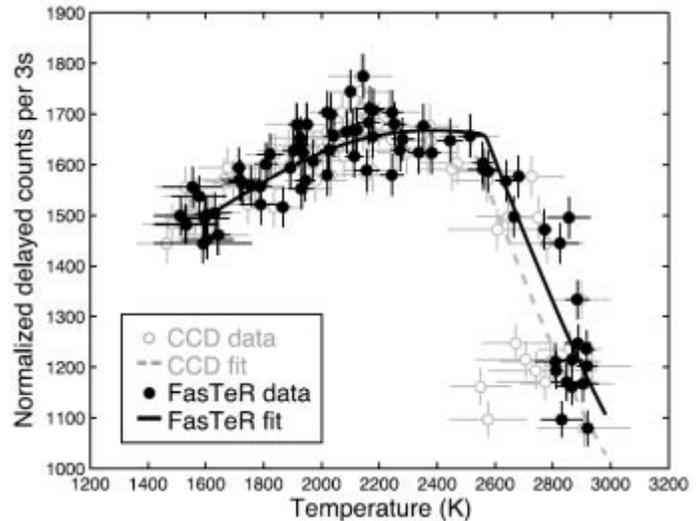
**Reference:** Zhang, D., J. M. Jackson, J. Zhao, W. Sturhahn, E. E. Alp, T. S. Toellner and M. Y. Hu (2015), Fast temperature spectrometer for samples under extreme conditions, *Rev. Sci. Instrum.,* 86, 013105.

# Electroless Deposition of Silver Nanoparticles on Graphene Oxide Surface and Its Applications for the Detection of Hydrogen Peroxide

Jun Zhu, KeunSoo Kim, Zhenxian Liu, Huan Feng,Shifeng Hou (Montclair State University)

(COMPRES-related facilities: National Synchrotron Light Source Beamline U2A)

A new process to decorate graphene oxide (GO) with silver nanoparticles was developed through electroless deposition technique, which was performed by treating GO with Sn2+ first and then with Ag+. Silver nanoparticles-GO (AgNPs-GO) nanocomposites were prepared by this technique. The process was monitored using UV-vis spectroscopy, Raman spectroscopy and transmission electron microscopy (TEM). The electrochemical behaviour of AgNPs-GO modified glassy carbon electrode was investigated by cyclic voltammetry. The potential application of this technique for hydrogen peroxide detection was tested with a range from 10 mM to 20 mM with a detection limit of 0.5 mM.
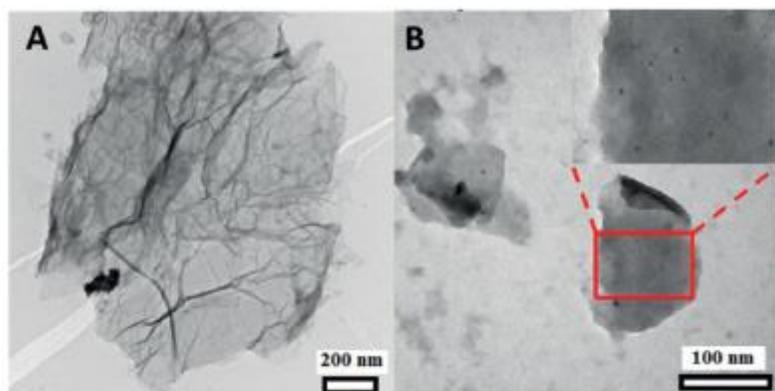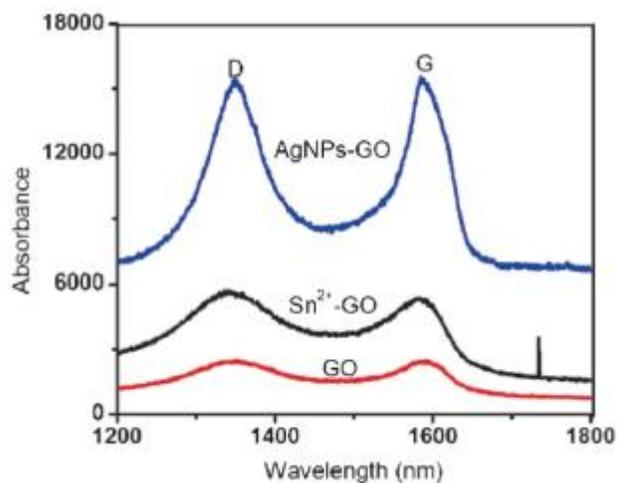


Fig. 1. TEM images of $Sn^{2+}$-GO (A) and AgNPs-GO (B).

Fig. 2. The Raman spectra of GO, Sn2+-GO, and AgNPs-GO.

**Reference:** Zhu J.,Kim K.-S, Liu Z., Feng H. Hou S. (2014) Electroless Deposition of Silver Nanoparticles on Graphene Oxide Surface and Its Applications for the Detection of Hydrogen Peroxide. Electroanalysis, **26**(11), 2513-2519.